ALLOCHTHONOUS PERMIAN ROCKS IN THE SOCORRO REGION, CENTRAL NEW MEXICO: A STRUCTURAL ANALYSIS OF EMPLACEMENT AND DEFORMATION

by

RONALD MICHAEL LINDEN

Submitted in Partial Fulfillment of the
Requirements for the Degree of Doctor of Philosophy
in Geoscience (Geology)

New Mexico Institute of Mining and Technology
Socorro, New Mexico

September, 1990

ACKNOWLEDGEMENTS

Very special thanks are due my advisor, Dr. Antonius J. Budding, for his guidance throughout all aspects of this project. In addition to being responsible for the initial conception of the project, many of the experimental and analytical techniques I have employed in this study were acquired through classes he taught and research he directed. His broad scientific background was a valuable resource in virtually every phase of this endeavor and it has been a pleasure working with him.

I would also like to thank the other members of my dissertation committee; Drs. David Johnson and Allan Sanford of the New Mexico Tech Geoscience Department, Dr. Marshall Reiter of the New Mexico Bureau of Mines and Mineral Resources, and Dr. J.A. Smoake, Professor of Biology and Dean of Gradute Students. Their critical review of this manuscript and helpful suggestions have added to its overall quality and completeness, and I wish to express my appreciation.

Partial support for this study was provided by a research grant from the New Mexico State Mining and Mineral Resources Research Institute to Dr. Budding and by the New Mexico Tech Geoscience Department in the form of teaching assistantships. Additional funding for this project was provided by the New Mexico Geological Society Grants-in-Aid Program, the Richard A. Matuzeski Graduate Research Fund, and the Antonius and Anita Budding Graduate Research Fund. The monetary assistance furnished by these sources was applied to several aspects of the study, and is gratefully acknowledged.

I wish to dedicate this work to all the members of my family for their unwavering support throughout this undertaking. In particular, my wife, Linda, and my parents, Michael and Antonia, without whose love, understanding, patience, and ca$h, completion of this project would not have been possible. Recognition is also due to my four-legged field assistants, Lucy and "the Weenie", who helped make the long days of field work more enjoyable and productive. Numerous conversations with Chris Beck, Bob Colpitts, and Dr. Clay Smith also proved helpful in this investigation – I thank them for their "ears" and "ideas".

TABLE OF CONTENTS

LIST OF FIGURES

ABSTRACT

Allochtonous Permian rocks of the Yeso, Glorieta, and San Andres Formations are present at a number of locations along the east side of the Socorro constriction in the central Rio Grande rift. These rocks overlie autochthonous Triassic and Cretaceous sediments (lower Chinle through lower Tres Hermanos) along low-angle faults, and also display décollement structures at several stratigraphic levels within the Permian section itself. Insight into problems concerned with the direction(s) of emplacement, and the mechanics and timing of deformation is obtained by detailed structural mapping and strain analysis of various kinematic indicators and structural features.

Marked differences in the mechanical properties associated with various members of the stratigraphic section have been instrumental in the deformation. The Permian section is essentially a series of thick, competent units (limestones and sandstones), which overlie an interval of relatively incompetent lithologies (evaporites and weak sandstones). Structural features indicate that a sheet comprised of these superincumbent, competent rocks has become detached from the incompetent lower section, and has been thrust over the Mesozoic sediments. Analysis of the deformation shows that a vertical strain profile through a typical allochthon can be characterized as extensional in the upper portions and compressional in the lower regions. This distinctive pattern suggests that the translation of the allochthonous rocks is best described by gravitational detachment along horizons of pronounced competency contrast.

Additional support for this conclusion is obtained from rock-mechanical experiments performed on the lithologies critical in the deformation. The resultant data on the rheological properties of the rocks have been used to construct Mohr analyses which explain the main structural characteristics observed in the deformation. Results indicate that the source of these allochthons were uplifts located in the region east to southeast of the study area. Based on structural, stratigraphic, and intrusional relationships, the deformation is believed to have taken place during the Paleocene Epoch.

INTRODUCTION

The purpose of this study is to investigate structural features found in the Socorro region of the Rio Grande rift. Within the field area (Figure 1) a number of allochthonous rock masses, décollement structures, and overturned folds have been documented by several investigators (Rosen, 1983; Colpitts, 1986). This deformation is largely restricted to the Yeso, Glorieta, and San Andres Formations of Permian age. Prior to the inception of this project little was known regarding the direction(s) of allochthon transport, or the mechanics and timing of deformation. It is the intention of this investigation to address and determine answers to these questions.

Field studies were conducted to gather structural data from the areas affected by this deformation. Stress-strain indicators such as folding, faulting, zones of brecciation, fossil deformation, stylolites, slickensides, joints, clastic dikes, and fracture fillings, were used to construct a model which can explain the observed field relationships. Each of these features presents a partial record of the kinematics of some stage of the deformation. Several general mechanisms of emplacement were evaluated based on the kinematic indicators and the outcrop geometries observed in the field. Implicit in this approach is that each of these proposed mechanisms of allochthon emplacement has associated with it specific types of strain indicators that can help differentiate between these alternatives.

Geologic maps showing the structural and stratigraphic features upon which the interpretation is based have been prepared and are included as additional plates. Plates 1 and 2 show the structure and geology (map view) of the two main allochthon trends, the Mesa del Yeso–Gibbs Place trend and the Sierra de la Cruz–Rancho Grande Well trend. Also included on each of these plates is a description of the lithologic sequence and an explanation of the structural symbols used in the construction of the maps. Cross-sectional interpretations are presented on Plate 3. In order to more effectively illustrate the complexity of this deformation, both maps and cross-sections have been constructed on a scale of $1 : 6,000$, or 1 inch = 500 feet (no vertical exaggeration on cross-sections).

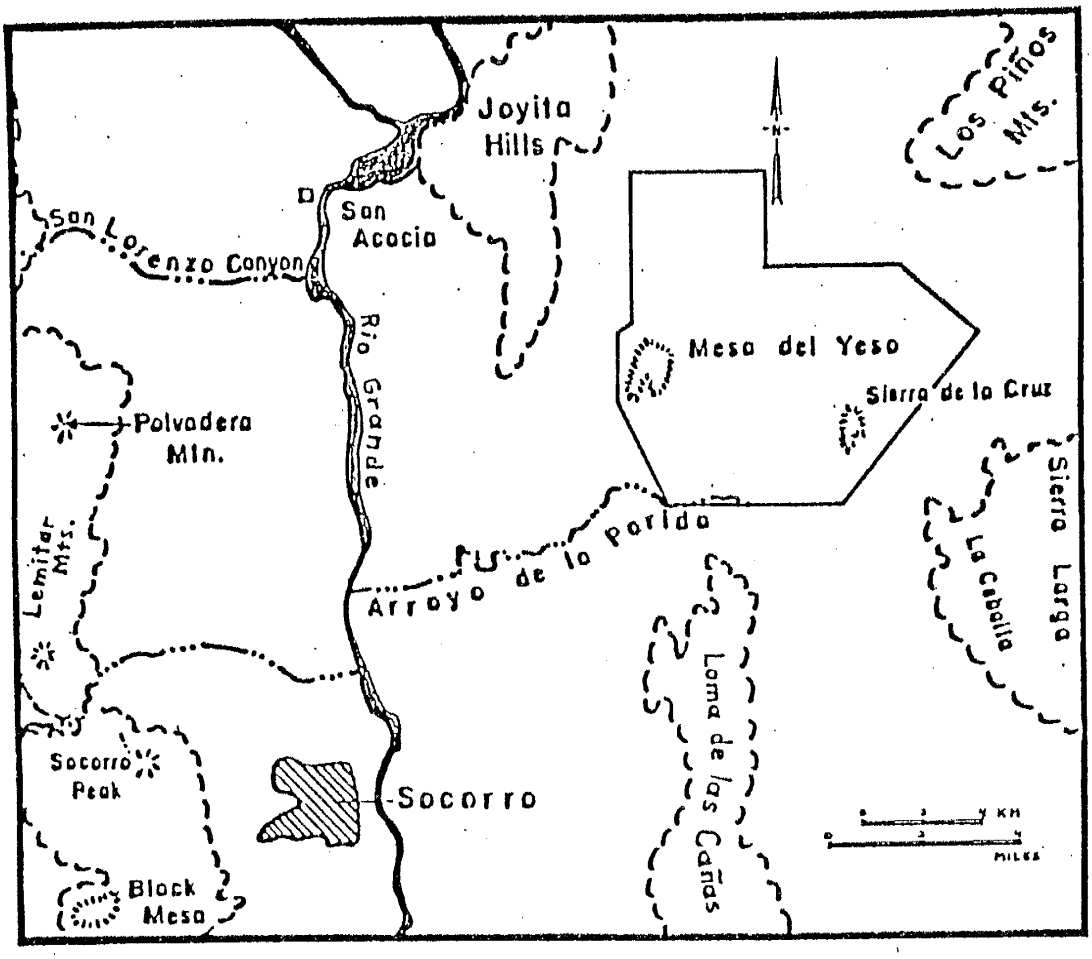

Figure 1. Generalized map of the Socorro region showing the location of the field area (within outline).

STRATIGRAPHY

Stratigraphic studies of the region east of the Rio Grande in central New Mexico have been conducted by various investigators (Hunter and Ingersoll, 1981; Hook, 1983; Siemers, 1983). Crystalline basement of Proterozoic age, composed primarily of metamorphosed supracrustal rocks and intrusive igneous rocks which range in composition from felsic to mafic (Condie and Budding, 1979), is overlain by Pennsylvanian, Permian, Triassic, and Cretaceous sediments. These rocks were subsequently buried by variable thicknesses of Tertiary volcaniclastic and volcanic rocks, and irregular deposits of Tertiary and Quaternary sandstones and gravels. Although not equally developed at all locations, Figure 2 presents the general stratigraphic sequence of the rocks characteristic of this region.

Included in the figure are brief descriptions of the dominant lithologies of the various formations and members. Also indicated is the portion of the stratigraphic column which is affected by the low-angle detachments. It is important to note that the section of the sedimentary section in which the detachments are present largely consists of alternating layers of thick, competent rocks (limestones and sandstones) separated by beds of incompetent material (evaporites and weak sandstones). This arrangement and combination will prove to be the crucial ingredient in the structural development of the allochthonous terranes. The present account shall investigate several structural scenarios utilizing data recorded in the field combined with experimentally determined rock-mechanical measurements. Knowledge of specific physical properties possessed by these lithologies, such as compressional strength, fracture angle, and viscosity, is necessary to critically evaluate these scenarios. Other investigators (Needham and Bates, 1946; Colpitts, 1986) have concentrated more on describing the characteristics of the sediments in the area and the reader is referred to these sources for more detailed information of this sort.

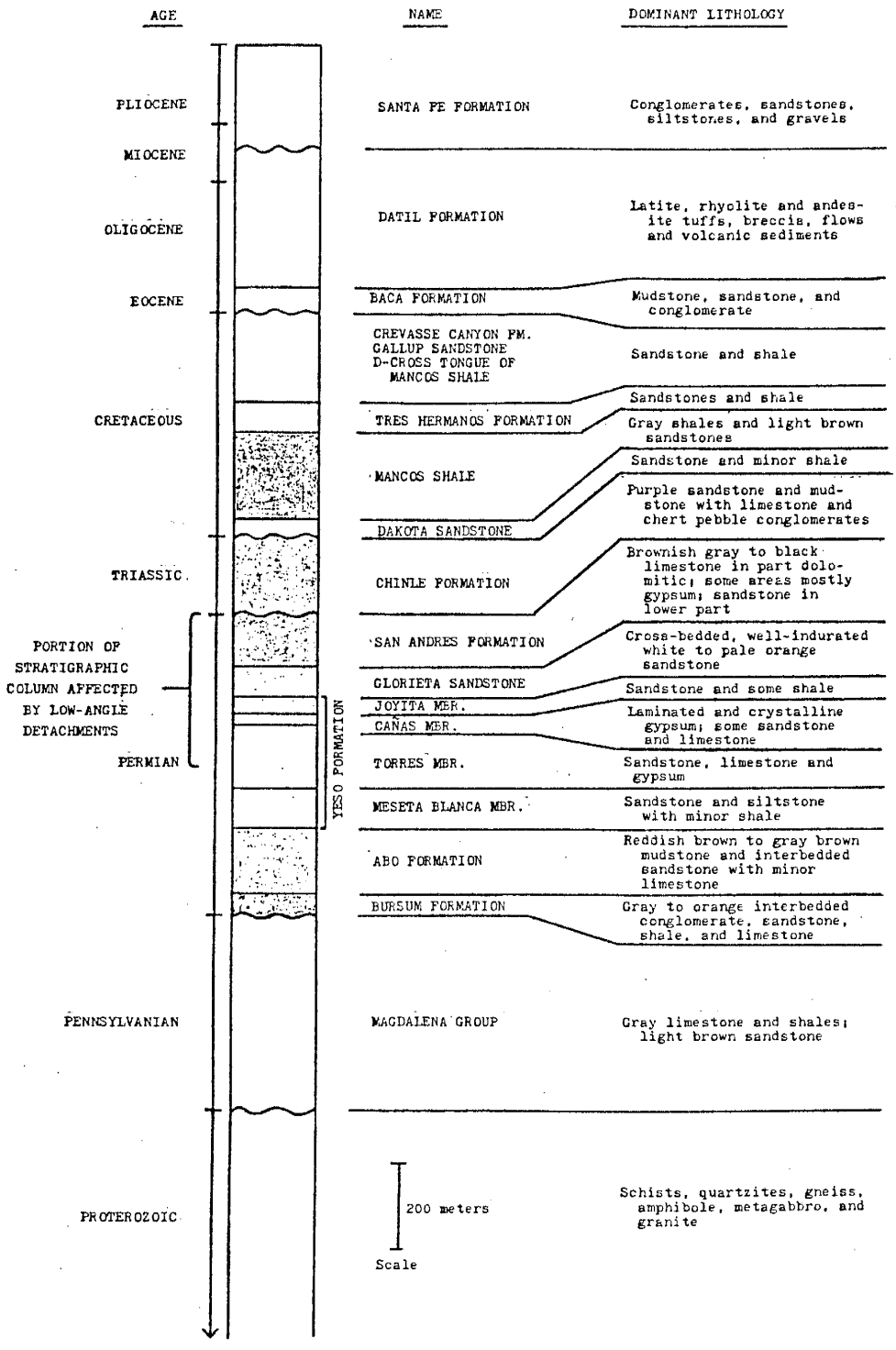

Figure 2. Generalized stratigraphic column of the rocks exposed along the east side of the Socorro constriction, central Rio Grande rift.

CHAPTER I – MAIN STRUCTURAL FEATURES

Several periods of tectonism have intensely folded and faulted the rocks along the east side of the Socorro constriction. These include deformation during Early Triassic time, some folding and formation of uplifts in the Laramide, the development of the flat-lying décollement surfaces and allochthon emplacement (which will be shown to have probably occurred during the Paleocene Epoch), and the later Neogene faulting of these rocks. A more comprehensive summary of these and other structural features found in the region has been compiled by Smith (1983). Our primary concern is the distribution of the allochthonous Permian rocks and the structures associated with their emplacement, so we shall limit our discussion to descriptions of these features.

Low-angle Faults

Of foremost interest in this study are the low-angle faults that are typical of this area. Where undisturbed by later high-angle faulting, these surfaces have dips which range up to 15 degrees, are locally irregular or undulose, and occur at several stratigraphic levels. Typically coincident with bedding planes, they have been observed in the middle to upper Torres, Cañas, and Joyita Members of the Yeso Formation, the lower part of the Glorieta Sandstone, and the lower to middle San Andres Formation. Movement along the detachment surface has often eliminated large parts of the stratigraphic section. A good understanding of the stratigraphy is essential because of the tendency of these faults to parallel bedding.

The development of décollement fault segments reflects the profound control on the structural development that is imposed by the anisotropy and heterogeneity of the lithologic sequence. Gypsum is the mechanically preferred horizon on which the décollement slip is accomodated because of its role as a weak decoupling layer and its propensity for flow, a property which helps initiate instabilities and promote folding. This reduction in coupling also results in an axis of maximum compression which is much less inclined to the horizontal than in the case of overburden stresses associated with homogeneous sequences (see Figure 27, p. 55). It is, therefore, quite common for differential drag along a gypsum layer to cause folds to rotate in response to sharp

contrasts in applied basal traction. It will be demonstrated that these décollements are initiated in and largely confined to stratigraphic levels that are inherently weak because of low rock strength, high fluid pressures, or both.

The low-angle faults are in general not a single geometrical surface, but consist of a layer (whose thickness is small compared with that of the overriding rock mass) in which the deformation and displacement is concentrated. Within the fault zone proper, virtually all the mechanical work performed on the fault is consumed in deformational and frictional processes. By definition (Turcotte and Schubert, 1982), the mechanical work expended on an active fault per square centimeter of its surface is equal to the product of the shear stress on a fault plane and the relative displacement of the fault blocks. This shear stress is the component parallel to the line of relative displacement. Observations of the fault zone indicate a frictional sliding mechanism evidenced by discontinuous zones of brecciation along the main structure and its transgressive segments (see Figure 11, p. 21). As the thrust sheets move over the underlying rocks, small areas may become permanently stuck and result in the propagation of a new fault branch. Evidence from field (Ramsay, 1967) and laboratory work (Paterson, 1978) shows that, on all scales, *active shear zones are zones of weakness and localized shear softening.*

Folds and Folding

Frictional forces acting across the fault may exert sufficient drag to cause folds to form. These drag folds are generally noncylindrical and asymmetric. Numerous overturned or recumbent, horizontal to gently plunging anticlines and synclines are found in the middle and upper Torres Member of the Yeso Formation (Figures 3 and 4). The sense of overturning, or vergence of these folds (Bell, 1981), varies between westerly and northwesterly for the most part, with a small number showing eastward vergence. Average orientation of the fold axes is N35E, with plunges of up to 20 degrees southwest or northeast (Figure 5). They are most commonly developed in the Torres and where the Cañas/Joyita section is absent. Because the fault-related frictional forces rapidly decay as one moves away from the immediate region of the

Figure 3. Typical example of overturned folds composed of interbedded limestones, sandstones, and gypsum, in the upper Torres. View is to the southwest; beds in foreground are steeply dipping away from observer (note dogtail for scale).

Figure 4. Multiple zones of décollement and associated small-scale folds have developed in the Torres. Here two such folds (one synform, one antiform) are in contact across a detachment surface.

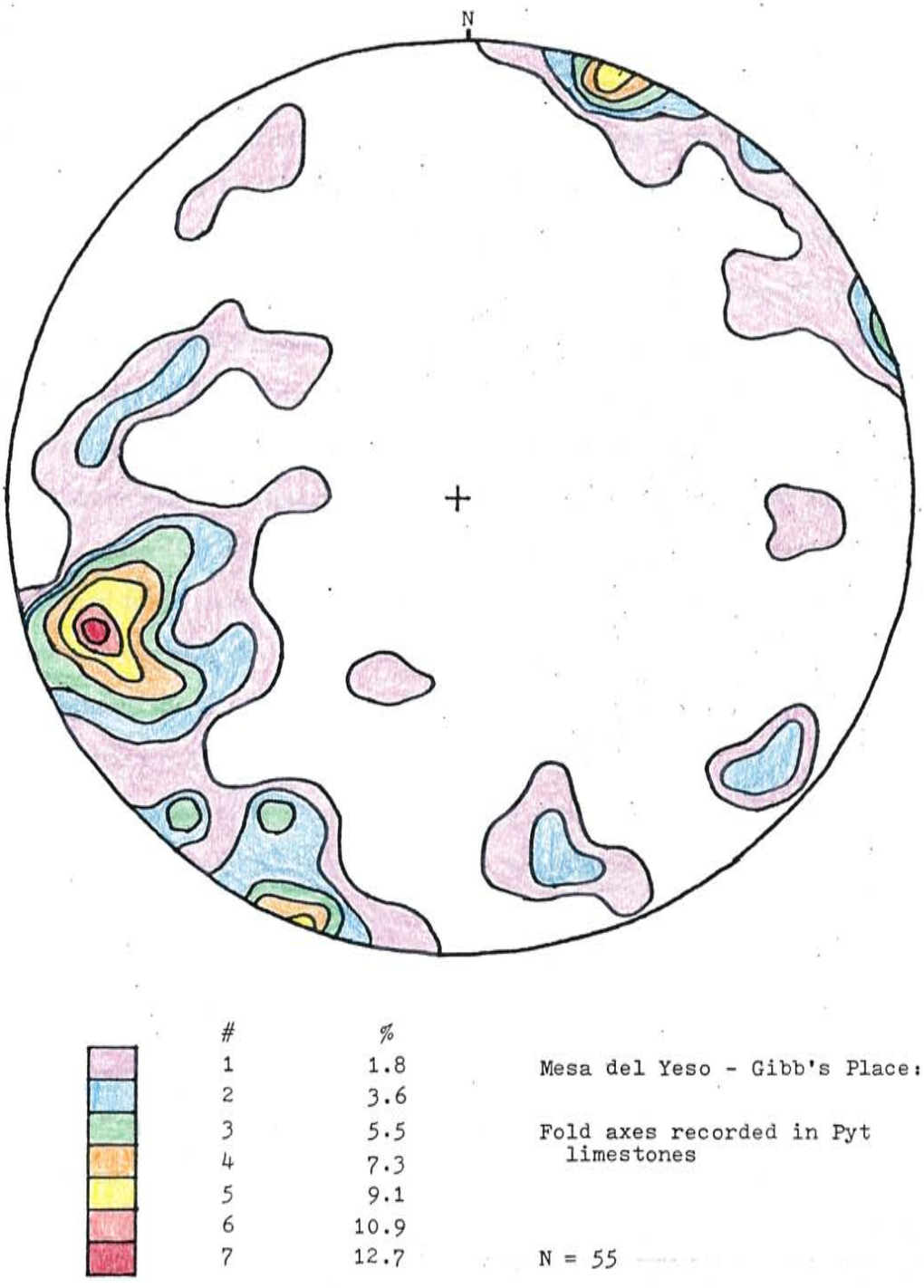

Figure 5. Contoured stereonet plot (Schmidt net; lower hemisphere projection) of fold axis orientations recorded in Torres limestones (Mesa del Yeso–Gibbs Place).

fault, these folds are closely localized near the fault surface (St. Venant's Principle of rapid dissipation of local stresses; Mase, 1970). This folding is clearly restricted to, and related to, the shear zone, and not caused by any later unrelated deformation. The orientation and the sense of overturning displayed by these features records deformation produced by the overriding allochthons. Deformation of stratified rocks demands that individual beds slip past one another and bend; friction between layers and the interstitial resistances of different beds to folding are much less than the cohesive forces of a solid mass. In active folding, where the layers have varied rheological properties, deformation will often be locally heterogeneous and complex. Fold styles observed in the study area vary continuously from open and nearly concentric, to closed, overturned and isoclinal. The open folds commonly have axial planes at fairly high angles (90° to 70°) to the plane of the shear zone, whereas the tighter, more flattened folds show axial planes with much lower angles of inclination. These characteristics suggest that the folds may have nucleated continuously or episodically throughout the deformation, and became progressively tightened, flattened and rotated towards the plane of the shear zone.

At present, most of the understanding of mechanical principles regarding the formation of both small and large scale folds is confined to the very first instabilities arising in systems with very simple rheology. The theory of multilayer folding as advanced by Biot (1961, 1965) and Johnson (1984) primarily deals with the onset of buckling and is generally applicable only to the initial stages of folding, i.e. when strains are comparatively small, being restricted to less than 10% of the original, undeformed dimensions. None of the computations made using these methods can be extended to describe fold shape as the folds increase in amplitude (Ramsay and Huber, 1987). Such works are, therefore, of limited use in illuminating the structural evolution of the fold complex found in the field area, and will not be considered further.

High-angle Faults

Throughout the study area high-angle faults are found in both the allochthons

and the underlying rocks. Several characteristics allow us to make some tectonic distinctions between those faults that are confined to the allochthonous sheet, and those that cut the underlying lithologies – it is this later group that will be investigated first. The majority of these are normal faults that exhibit dip-slip motion as evidenced by frictional phenomena (slickensides, gouges), but reverse faulting is also noted, particularly in association with the Montosa Fault (see Plate 2). Fault trends cluster in four general orientations; two main groupings at N30E ± 10° and N40W ± 20°, and two subordinate clusters at approximately E-W and N-S orientations.

The most numerous faults in the field area are those that trend northeast. They are also the most laterally persistent and exhibit the greatest amount of displacement, with some exceeding half a kilometer. Structural truncation of members of the other high-angle fault groups indicate that the NE striking faults were the first to form. Dip angles range from about 60° to near vertical with most faults being down-dropped to the southeast. Faulting within the Montosa System is more complex due to its compressional nature as a positive flower structure (Harding, 1985). This structure, which is composed of several strands and forms an anastomosing pattern which cuts the sediments into numerous separate blocks, trends approximately N30E. The fault zone juxtaposes Pennsylvanian Madera Limestone and Permian rocks (Bursum and Abo formations) on the east side with the Meseta Blanca and Torres Members of the Yeso Formation (Permian) on the west. Some distance further to the northeast (10-15 km), Stark and Dapples (1946) report that this sense of displacement is reversed. The rocks within the fault zone show evidence of folding and variable dips are noted due to tilting of individual blocks. Several locations (see Plate 2) indicate where the Montosa Fault has cut the Permian allochthons, suggesting that the fault system either developed contemporaneously with or postdated the development of the allochthons. It will be shown that the former option is preferred.

The northwest trending faults (N60W to N20W) are the next most populous set found in the study area. These features are predominantly dip-slip normal faults showing only small to moderate amounts of movement, commonly on the order of

several meters to several tens of meters. They are locally observed to curve into and merge with the northeasterly trending faults. Dips measured in the field range from about 45° to essentially vertical, and faults can be down-droppped to either the northeast or southwest. Those faults which show N-S or E-W strikes are much less numerous than the two previously described sets. Dipping at high angles for the most part (75–90°), they show widely varying amounts of displacement; some as little as several meters, while others place upper Abo in contact with Torres ($\approx$ 150 meters). Development of such displacements on these faults is probably associated with Tertiary normal faulting which accompanied rifting.

Faults which cut the allochthons are usually of small vertical displacement (less than 10 meters) and tend to have dips between 70° and vertical. A north to northeast directional preference is observed, although northwest trends are also present. Dip-slip motion down-to-the-east is the most common sense of displacement noted; no strike-slip movement is evident in any of these faults. As a rule, these features do not penetrate into the underlying strata, but remain confined to the allochthonous sheet. Mechanical reasons why this is so and an overview of tectonic faulting in general are discussed at length in the sections dealing with physical properties and mechanical modeling.

Types of Allochthonous Relationships Observed

As shown in Figure 6, the allochthons present in the field area come in a variety of chronostratigraphic relationships. The column on the left side of the figure represents the undisturbed stratigraphy and accurately portrays the relative thickness of the units. To the right of the column, the three main types of allochthon geometries are illustrated. Type A represents the case where the relative ages of the lithologies across the detachment surface are correct, younger over older, but where several sedimentary units normally present (Pyj, Pyc) have been tectonically eliminated. The situation shown in type B is one in which older rocks overlie younger rocks; members of the Permian section (Pg, Psa) are superincumbent upon Mesozoic sediments, usually the Triassic Chinle Formation. The third arrangement is actually a composite of types A

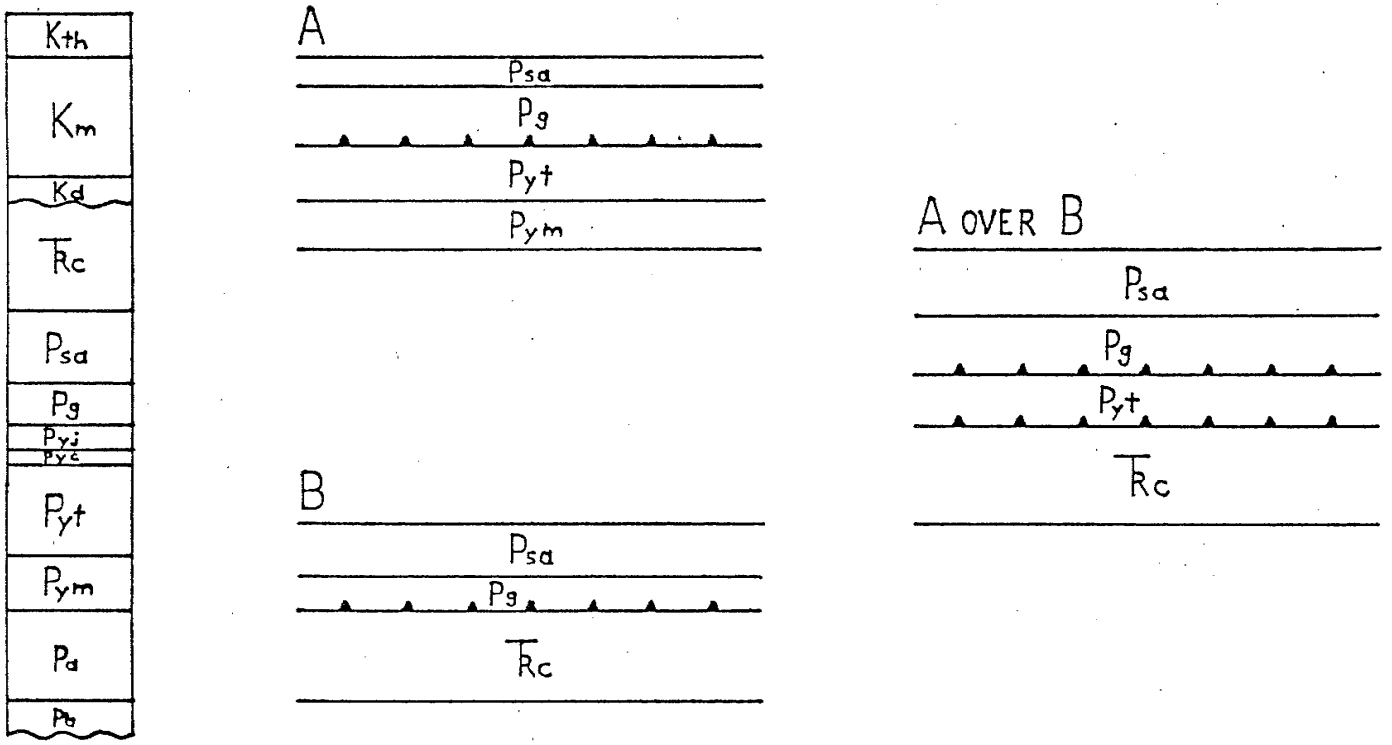

Figure 6. Types of allochthonous relationships characteristic of the deformation found within field area.

and B. In these situations, Permian rocks overlie lithologies of Mesozoic age (type B) while they themselves have suffered stratal thinning or elimination (type A) – hence, we get A over B. This geometry is actually the most common one observed in the mapped area (see Plate 1).

CHAPTER II – STRESS-STRAIN INDICATORS

Each of the strain indicators observed in the field defines a unique direction of relative extension or compression, or a unique line of slip or axis of rotation. When considered collectively, these data provide a direct and succinct record of the kinematic history of the rock, and serve as a sound basis for dynamic analysis of deformation. A short description of the kinematic significance of the various indicators will be given, to be followed by its particular relevance to the deformational picture we seek to assemble.

Stylolites

These pressure solution phenomena record the orientation of the greatest principal stress. Because one or the other surface of a bedding plane or fracture is locally more soluble, the surface of dissolution develops a highly irregular, toothed shape; these irregular dissolution surfaces are called stylolites, an example of which is shown in Figure 7. Rock is dissolved along these surfaces, so they are commonly lined with a layer of insoluble residue, as observed in thin-section. Stylolites are most abundant in the limestones of the San Andres Formation, but are also found in the limestones of the Torres Member (Yeso Formation). Most of the stylolites observed in the field area are parallel to bedding, suggesting that lithostatic pressure due to gravitational loading was the greatest principal stress. Orientations perpendicular to bedding were exclusively found in areas where the Torres has undergone tight folding (Figure 8), indicating a change in the orientation of the most compressive stress as compared with the San Andres.

It has been reported by Dunnington (1967) that stylolites may form in limestones buried by as little as 90 meters of overburden (vertical stress $\approx$ 2.25 MPa). Between

Figure 7. Example of stylolite formation parallel to bedding as commonly observed in the Torres and San Andres limestones.

Figure 8. Areas of tight folding in the Torres limestones have produced stylolite formation perpendicular to bedding.

750 and 1000 meters of superincumbent material may have overlain the Permian rocks at the time of deformation, resulting in a vertically oriented stress of $\approx$ 18.75 – 25.00 MPa. Such stress conditions are clearly in excess of requirements for stylolite formation.

Extensional Jointing

Joints are the most ubiquitous structures to have developed in the rocks, and are found in both competent and incompetent lithologies. They are cracks or fractures along which there has been little or no displacement parallel to the fracture surface. Extensional joints are usually planar and the joint planes are often perpendicular to bedding and generally uniform in direction for considerable distances. They usually occur in systems composed of several joint sets oriented in different directions, the individual members of which are more-or-less parallel and regularly spaced. The morphology of these joint surfaces provides insight into the mechanisms responsible for their formation. Joints formed in tension will display a hackly, abruptly uneven appearance incompatible with frictional sliding. Structural characteristics of shear failure such as scratches, grooves, gouge, or brecciation will not be observed unless movement parallel to the joint surface has taken place. Extensional joints are formed as the result of the dilatational response of brittle materials in which σ_1, the most compressive stress, is parallel to the joint. A more exhaustive discussion of the mechanical constraints and structural evolution of regional jointing is given in Linden (1987).

It is generally thought that joint formation is due to the effect of tensile stresses generated during uplift and denudation. This uplift and denudation affect the pre-existing stress in three ways: (1) by horizontal extension due to uplift, (2) vertical expansion and horizontal contraction through the release of gravitational load, and (3) contraction produced by cooling. These processes have a net effect of producing horizontal tension in most cases. The buildup of tensile stress will proceed until it equals the tensile strength of the material, and jointing will occur. Studies show that the joint frequency is dependent upon the bed thickness, the physical properties

of both the rock bed and its surroundings, and the degree of tectonic deformation. Theoretical and experimental studies (Price, 1966; Hobbs, 1967; and Linden, 1987) have demonstrated that under the conditions of stress that occur in the uppermost several kilometers of the crust (Haimson, 1977), neither the tensile strength nor the compressional strength of most crustal rocks are exceeded. Since it is not possible to form either extensional or shear fractures, *the conclusion is reached that regional joints cannot be the products of severe horizontal compression during a vigorous period of mountain building.* Instead, fractures develop in a subsequent period of decreasing horizontal compressive stress associated with the orogenic movement of rocks to progressively shallower levels in the crust. Due to the attitude and characteristics displayed by the joint systems noted in the field area, this general scenario is believed to be applicable to the present study.

Fracture Fillings

Extension fractures which develop due to extensional strain and rupture usually initiate in a direction parallel to the most compressive stress, σ_1, and perpendicular to the least compressive stress, σ_3, acting at the time of failure (Jaeger and Cook, 1979). With further increments of strain, they generally continue to open, either perpendicularly or obliquely to the fracture surface depending upon the orientation of the local strain ellipse. These fissures are filled with fluid in most tectonically active situations, and this fluid phase usually contains minerals in solution. Because the fracture is a site of low pressure, the fissure becomes filled with crystalline material as it is progressively opened, in acordance with Riecke's principle. The orientation of these crystals will faithfully indicate the direction in which the opening has progressed (Ramsay and Huber, 1983).

Several locations in the Torres and San Andres exhibit "chocolate tablet" structures which indicate the systematic, sequential manner in which the fragmented material separated. Frequency maximums recorded from fractures oriented perpendicular to bedding in the San Andres limestones correspond to extensional directions of approximately N65W and N40E. These examples of plane strain specify that σ_1 be

vertical and that extensional strain is largely confined to the plane of bedding.

Fibrous vein systems are usually most abundant in the more competent units of a stratified succession of rock, and indeed, there are numerous extension veins to be found in the San Andres and Glorieta Formations. But the sediments that contain the most highly developed vein systems are the relatively incompetent, weakly-cemented Torres sandstones that are often found directly beneath the overriding allochthons. Ramsay and Huber (1983) point out that incompetent materials will only develop systems of extension veins where these materials have suffered exceptionally high local strains and strain rates. Circumstances involving such differential slip can be found on the limbs of the flexural slip/drag folds generated by the translation of the superincumbent sheet.

Syntaxial veins, the major characteristics of which are illustrated in Figure 9A, are most common in the San Andres Formation. These features are compositionally identical or very close to that of the surrounding rock; in the present case, calcite veins in San Andres limestones. The fibers occur in two distinct groups which are attached to either wall and show crystallographic continuity to the corresponding wall rock crystals. The contact which separates these two fiber groups is a more-or-less centrally located suture called the median line. Such structures can often be seen on the hand-specimen and outcrop scale. Individual fibers can exhibit forms which are perpendicular to the vein walls and become progressively more curved toward the median line. Across this suture the fibers will show a mirror-image curvature. As a result of certain crystals being more favorably oriented for growth than others, there are changes in fiber width toward the central suture. This change in the width of individual fibers is best interpreted in terms of progressive growth sense from wall to center – hence, the name syntaxial.

An analysis to determine the direction of calcite crystal growth within fractures was performed on oriented thin-sections of San Andres Limestone using the universal stage. Results are illustrated in Figure 10, which is a contoured plot of the c-axis orientation of the crystals. The strong concentration of points perpendicular to the

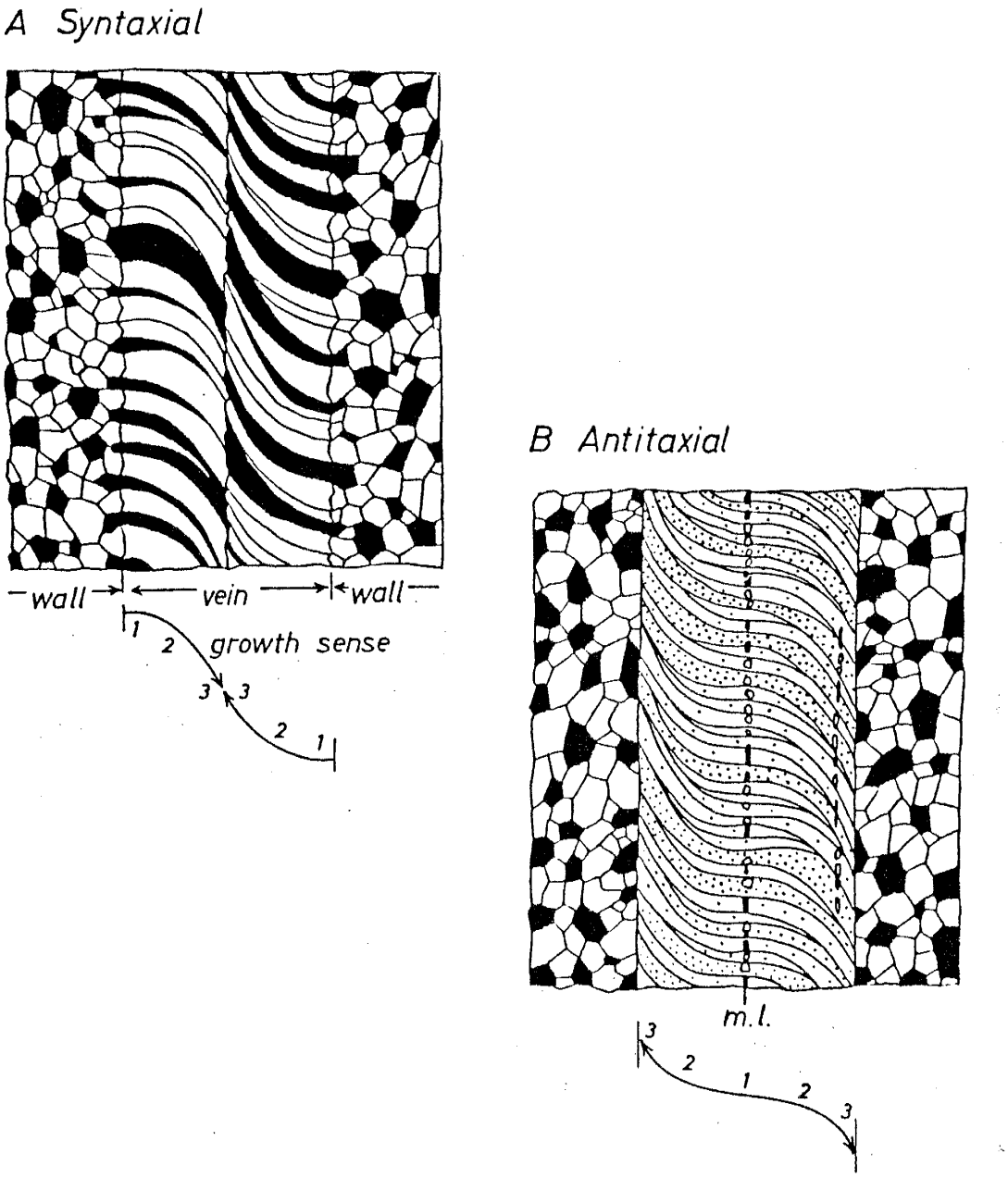

Figure 9. Principal features of fibrous vein systems showing the relationship of the composition and crystallographic orientations of vein and wall rock crystals. (A) Syntaxial veins. (B) Antitaxial veins. (modified after Ramsay and Huber, 1983).

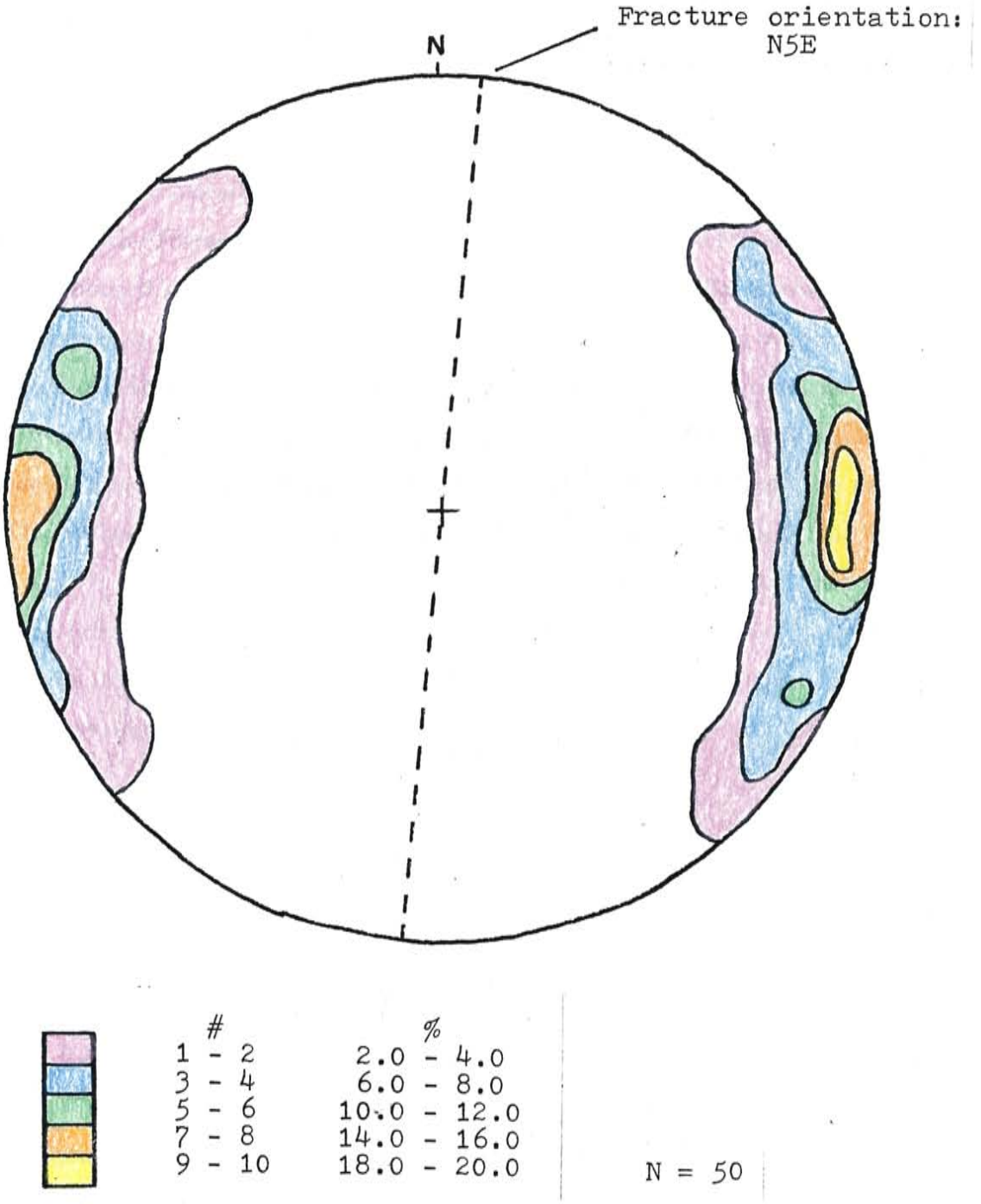

Figure 10. Contoured stereonet plot (Schmidt net; lower hemisphere projection) of c-axis orientations recorded from calcite crystals in extension veins formed in San Andres limestone.

fracture orientation indicates that shear movement did not influence the growth of the crystals. This offers support for other observations which suggest these features are dilatant tensile fractures formed by a gravitationally imposed greatest principal stress.

Figure 9B schematically illustrates the geometry of the antitaxial fiber veins which are common in the Torres sandstones. A distinctive characteristic of these veins is that they are composed of different material than that of the vein walls. Specifically, the fibers are made up of gypsum derived from nearby (0.1–20.0 meters) evaporite beds. Therefore, these fibers do not form wall-related groups, but do exhibit crystallographic continuity from wall to wall. Many of these veins have wall rock fragments which have been incorporated as solid inclusions with the crystals of the vein along the median line. The inclusions are composed of debris derived from the walls of the initial fissures and/or transported into the developing fractures accompanying fluid influx. Numerous such veins have been noted in the field area, and an analysis of their growth sequence and orientation is given in the section dealing with mechanical modeling (see Figures 29 through 33).

Breccia Zones

Locally persistent zones of brecciation occur where rocks have been mechanically crushed along fault contacts. This cataclastic metamorphism generally results in a reduction in grain size due to fracturing and granulation of the materials in contact. Little or no heat is usually present during this process. The breccias commonly consist of angular fragments suspended in a fine grained matrix of crushed material (Figure 11), the compositions of which are dependent upon the lithologies in contact. For example, breccias associated with the fault contact between the Glorieta Sandstone and the Torres Member display rounded to well-rounded Glorieta and Torres fragments suspended in a matrix of poorly sorted, smaller fragments. This fine-grained material is quite susceptible to chemical alteration (as evidenced by the presence of various oxides) which can result in rapid erosion and topographic emphasis of the fault. In some cases, local recrystallization of the minerals in the fault breccia has produced a

Figure 11. Photograph of low-angle fault illustrating zone of brecciation and Riedel shears.

resistant ridge at the fault.

Mechanical crushing is also noted in regions where the sediments of the Torres Member have undergone tight-to-isoclinal folding. At these locations, the limestone beds, which are normally quite resistant and well-preserved, are reduced to broken, irregular pieces approximately 1.0 cm to 10.0 cm in their longest dimension. Some show visible scratches and gouging, suggesting frictional/abrasive processes as the folding and movement progressed. Brecciation along many of the normal faults which cut the allochthons is also observed. Where preserved, the directions of slickensides indicate predominantly dip-slip motion.

Riedel Shears

Occasionally there are Riedel shears developed in conjunction with the low-angle fault contact(s) in the field area. Riedel, or additive shears, have the same sense of shear as the main fault, and thus add to the slip (Suppe, 1986). Such features prove quite useful in determing the sense of slip because the acute angles they make with the fault point in the direction of slip. Orientations recorded in the field from a series of north-trending exposures (sec. 5, T.2S, R.2E) indicate a direction of allochthon emplacement from approximately due east. Figure 11 shows an example of Riedel shears which have developed in the fault breccia.

Slickensides

The process of frictional sliding along an interface produces polished and striated surfaces called slickensides. It is the abrasion by the wall rock and fault zone fragments that produces these features, in much the same way as glacial striations and polish are formed. Surfaces showing slickensides represent a locus of shear and define a unique set of three orthogonal kinematic axes: (1) the line of slip marked by the slickensides striae (a-axis), (2) an axis of rotational slip (b-axis) positioned in the fracture plane and perpendicular to the slickenside striae, and (3) the normal to the fracture plane (c-axis), which combined with the direction of slip defines the plane of deformation (ac plane). Slickensides have been recorded in all lithologies except gypsum, and display a variety of attitudes and directions. Two general

groupings of slickenside data are apparent: a more-or-less omnidirectional clustering at about 50–70° around the center of the net associated with dip-slip movement on normal faults, and a concentration located close to the primitive circle probably due to movement accompanying allochthon translation. Both groups are clearly displayed in the contoured stereonet shown in Figure 12.

Fossil Deformation

Fossil cephalopods collected from various locations within the San Andres Limestone were analyzed by the method of Tan (1977). This technique of strain analysis can be applied to fossils whose initial shapes approximate that of logarithmic spirals, without having to assume the direction of the principal strains. It relies on a fundamental property of the logarithmic spiral that the tangent at any point of such a curve makes a constant angle with the polar radius vector. Positive identification of the cephalopods was not possible due to lack of preserved detail, but this restriction does not severly compromise Tan's procedure. Such analysis yields very small (less than 2%) amounts of deformation, suggesting an essentially neutral or passive involvement of the translating allochthons in the deformational process at the stratigraphic level of the San Andres. The cephalopods are occasionally cut by high-angle joints, although cases where joint directions are refracted around the cephalopods (presumably due to mechanical contrasts between the fossil and the enclosing rock) are also observed. Echinoid (subclass Regularia) (Moore and others, 1952) spines are present in the San Andres at a few localities; subcylindrical, up to 4.5 cm in length and 0.5 cm in width, these primary spines show no observable deformation.

Deformed feeding burrows (parallel to bedding) were noted in parts of the upper Torres and San Andres limestones; they show elliptical cross-sections perpendicular to the plane of bedding. When viewed in thin section, it is not possible to determine how much, if any, of the observed deformation is due to tectonic forces after the effects of initial sediment compaction (σ_1 vertical) (Cutter, 1985). Other fossils whose geometry lends them to quantitative deformation analysis (i.e. possess shapes for which there is a well-defined mathematical description) are scarce in the area, so no additional

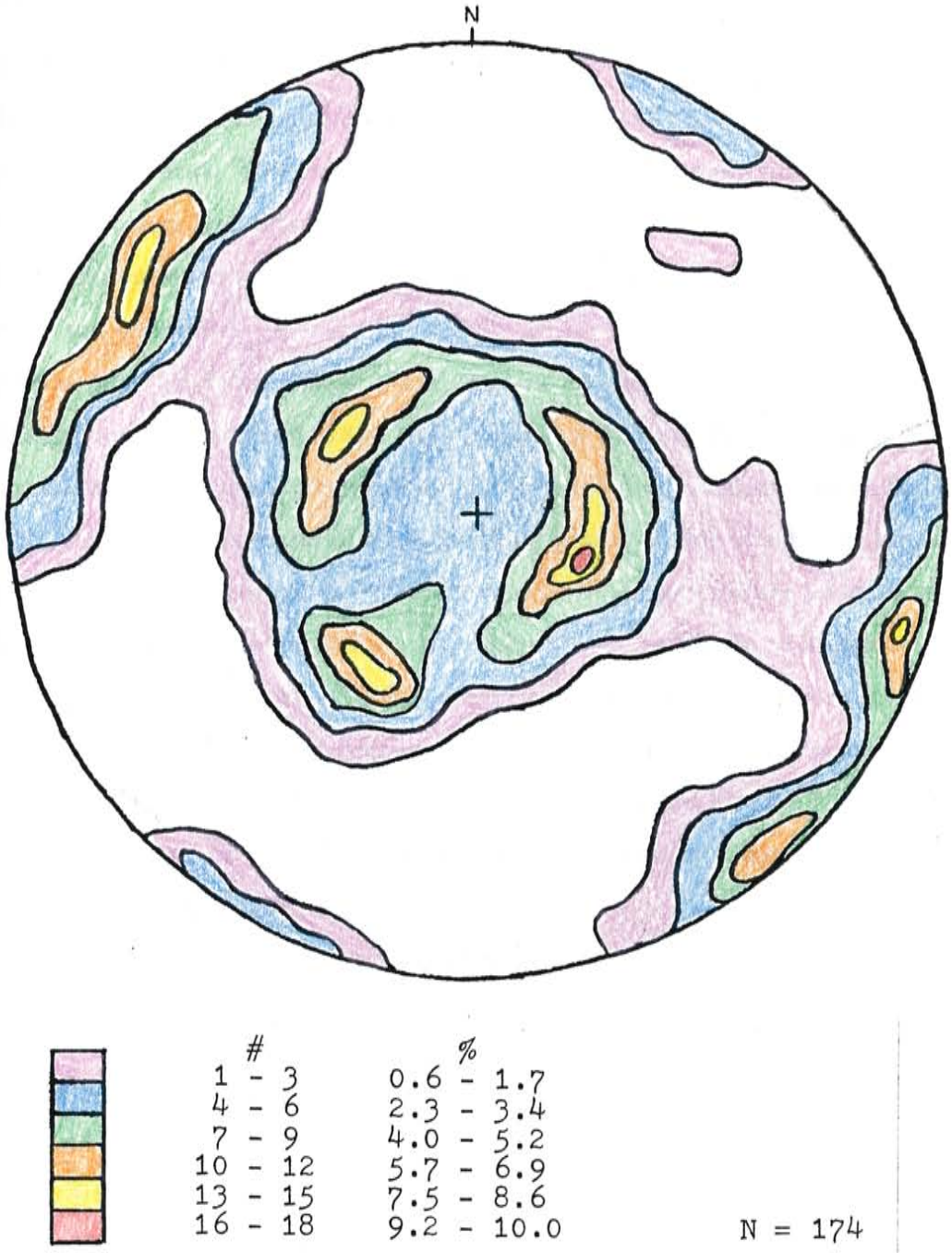

Figure 12. Contoured stereonet plot (Schmidt net; lower hemisphere projection) of slickenside orientations recorded from the lithologies in the field area.

strain determinations were made.

Clastic Dikes

Numerous clastic dikes and related examples of locally high fluid pressure can be found in the field area. These are exclusively located in close proximity to deposits of gypsum, allochthon contacts, and areas of pronounced folding. The matrix material consists of fine-grained sand and silt in which small, angular clasts of sandstone and limestone are imbedded.

Several sites on both Plates 1 and 2 show evidence of the relative timing of this fluidization with respect to the local episode of folding. Water released from the gypsum during dehydration produced locally elevated fluid pressures which facilitated the emplacement of this material along bedding planes within the Torres limestones. Later drag-folding associated with the movement of the overriding allochthons then deformed both the limestones and the injected material, as Figure 13 illustrates. Some locations show "chocolate tablet" structure on both vertical and horizontal exposures, a direct indication of high fluid pressure acting to decrease the stresses normal to the pre-existing extensional fracture surfaces. Clastic dikes can also be found along the axial planes of some of the folded sandstones and limestones, apparently emplaced during the period of folding.

Igneous Intrusions

Alkaline diabase dikes are found to pierce the allochthons at a number of locations in the mapped area. Similar intrusions have been dated as being $\approx$ 27–30 million years old (Aldrich and others, 1986); they are generally associated with the early stages of rifting and are useful in establishing the timing of allochthon emplacement. Heat from the intrusions has affected the surrounding rocks in several ways. When sandstones are intruded, there is a noticeable color change – usually a deep reddening is observed. This feature is a reliable indicator of the presence of a dike even when it is not apparent from surface outcrops. No such drastic color change is noted in the case of limestones. Contact metamorphism has altered the normally friable sandstones so that they are now much more densely cemented and locally resemble quartzites. The

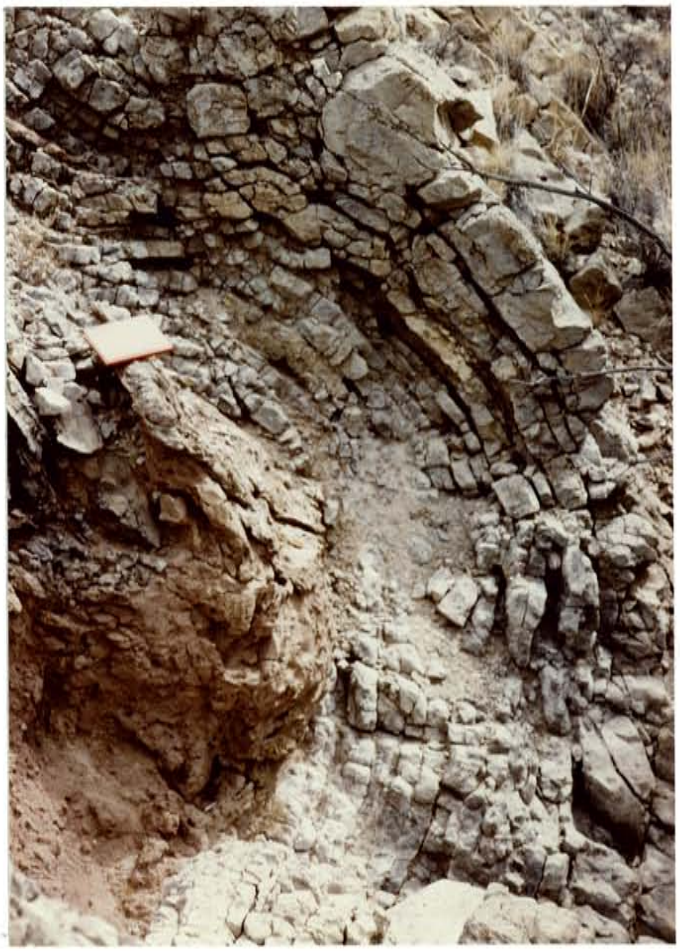

Figure 13. Clastic dikes injected between beds of competent limestone show evidence of folding due to forces associated with the movement of the overriding allochthons.

limestones are characterized by increased joint densities in the neighborhood of the intrusions. These effects are confined to areas in close proximity to the dikes, usually within 10 meters lateral distance.

One reason for the lack of more extensive "baking" and contact effects may lie in the chemical nature of the dikes themselves. Petrographic analysis (Rosen, 1983) has shown that the dikes in the area may be generally classified as being alkaline diabase. Broadly speaking, the degree to which country rock is thermally affected by intrusions is related to the volatile content of the injected material. Those of granitic composition normally have a higher volatile content than the more basic varieties, such as alkaline diabase. The higher proportion of volatiles will diffuse into the surrounding rock and transfer the heat from the intrusion more efficiently into the regions adjacent to the dike, thus causing contact effects over a larger area and to a greater degree. The fact that the sediments adjacent to the intrusive bodies have undergone only moderate changes is probably due to the relatively low volatile content associated with mafic intrusives (personal communication, A.J. Budding).

Distribution of Deformational Features and the Nature of the Strain Ellipse

Next we consider the nature and distribution of the various deformational features and kinematic indicators associated with allochthons and substratum. Figure 14, which serves as a schematic cross-section through a typical "A over B" allochthon, shows the relative locations where these features are observed. Two important aspects of the phenomena are summarized in the sketch: (1) that the nature of the deformation can be separated into two general categories, brittle and ductile, based on lithologic characteristics and position within the allochthon complex, and (2) that when all the deformational features and their relative locations with respect to the basal contact of these allochthons are considered, a definite pattern to the nature and orientation of the strain ellipse emerges (Webb and Cooper, 1988). The situation in the Torres (brittle/ductile) is a bit more complicated. Because of the strong competency contrast between limestones and gypsum, there are two orientations shown for the strain ellipse at this level; one for the competent beds (solid ellipse), and one for

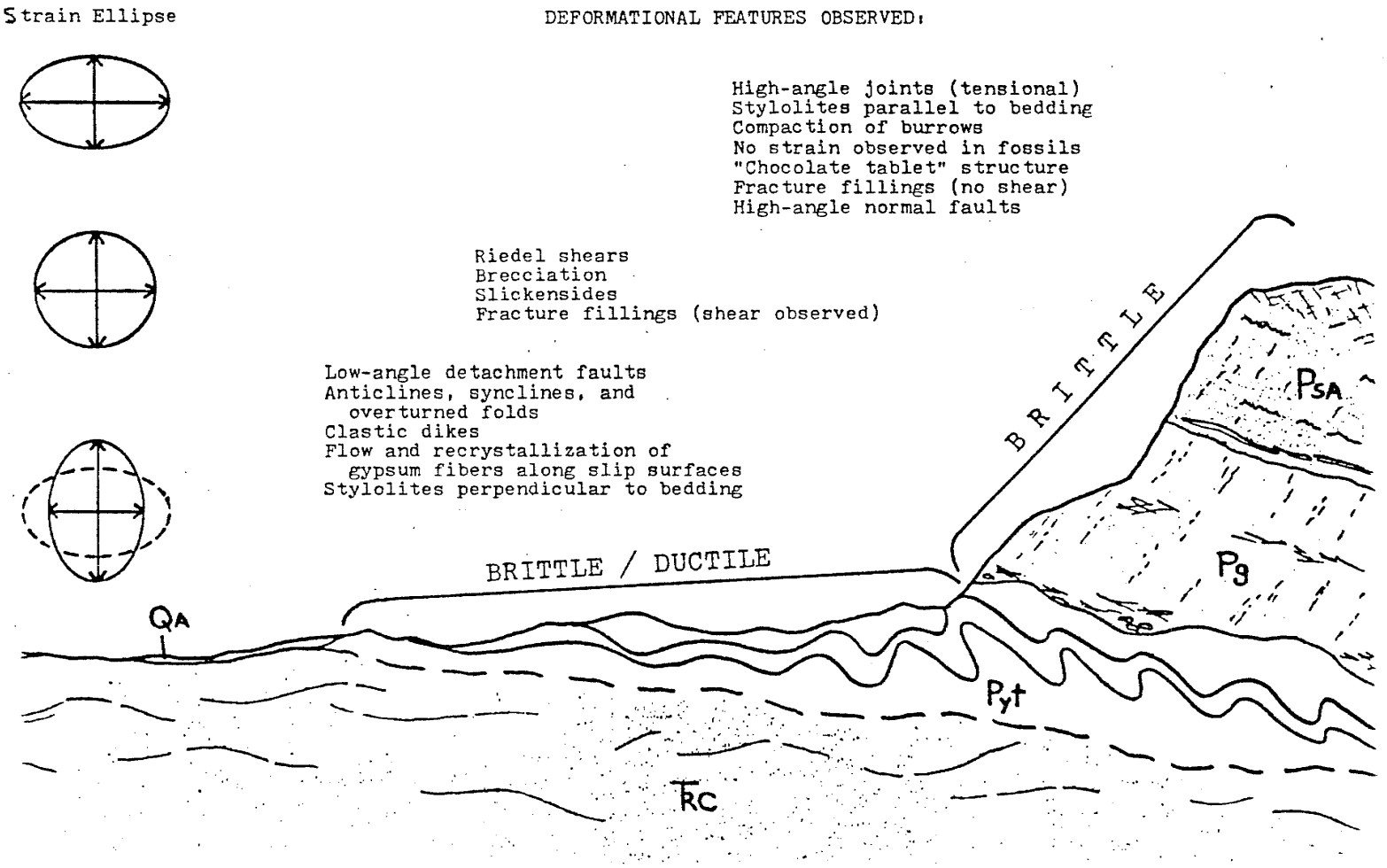

Figure 14. Schematic cross-section through a typical "A over B" allochthon illustrating the types of deformation observed and the overall orientation of the strain ellipse.

the incompetent material (dotted ellipse).

It is important to distinguish between brittle micro-processes and viscous micro-processes. The rate at which brittle micro-processes take place is essentially independent of the magnitude of the local stresses, whereas viscous or ductile deformation changes markedly with the magnitude of these stresses. Ductile processes include all microstructural changes that take place by means of mass-diffusion processes, such as pressure solution and dynamic recrystallization. In the present study, with the exception of the stylolite development, the bulk of the deformation suffered by competent lithologies is due to brittle processes. In contrast, virtually all the deformation observed in the incompetent gypsum is the product of ductile processes.

CHAPTER III – TIMING OF ALLOCHTHON EMPLACEMENT

The next step is to construct a simplified scenario, based on local geologic parameters, which is capable of explaining the major deformational features. To start with, what sort of field evidence is found within the study area that will constrain time limitations on when this deformation took place? This question is complicated by the fact that the age of the lithologies which form the allochthons is restricted to such a narrow interval of the Permian. There are, however, four pieces of information which can be used to estimate the timing of deformation; specifically,

1. part of the allochthonous sheet overlies the Tres Hermanos Formation (Upper Cretaceous), therefore, emplacement must have taken place after deposition of these strata,
2. in the eastern portion of the field area, the Montosa Fault system (late Laramide) cuts the allochthonous sheet,
3. nowhere within the mapped area does any of the deformation associated with the allochthons involve the Eocene Baca Formation ($\approx$ 40 MYBP), and
4. in several areas the allochthons are intruded by igneous dikes associated with the early stages of rifting (Oligocene, $\approx$ 30–27 MYBP) and would have to have been emplaced before this time.

Sequence of Deformational Events

The simplified sequence of events illustrated in Figure 15 is proposed to account for the structural development of the allochthonous Permian rocks. Figure 15A begins with an undisturbed sedimentary sequence in the late Cretaceous. At this time deposition and periodic erosion of all the Paleozoic and Mesozoic lithologies has taken place. The stratigraphy in the sketch is divided into four sections depending on the nature of its involvement, or lack of involvement, in the structural developments. Starting from the bottom of our sediment stack, the first section (1) is composed of the Meseta Blanca, Abo, and older Phanerozoic units, rocks which are largely unaffected by the emplacement of the allochthons. Section (2), between the long dashes, represents that portion of the column which comprise the allochthons, the Torres through San Andres lithologies. Next we have section (3) which is made up of those rocks which have been overridden by the translating allochthonous sheet, the Triassic Chinle through Tres Hermanos sediments (Upper Cretaceous). Finally, the last and uppermost portion, section (4), represents superincumbent Cretaceous sediments that either were not involved in the deformation or have subsequently been eroded.

Figure 15B is set in Paleocene time (65–45 MYBP), the period during which the available data suggest the deformation was initiated. We show the right side of our stratigraphic section as being uplifted, for our model requires a source of gravitational potential energy to bring about the emplacement of the allochthonous rocks. There are several possibilities for such structural uplifts; namely, vertical movement associated with transpression in the vicinity of the Montosa Fault, or the development of the northeast-trending anticline located just south of the field area. These alternatives will be discussed more fully in a later section.

Also shown in the diagram is a slip surface representing the probable geometry of the initial detachment (Webb and Cooper, 1988). Detailed explanations of the evolution of this and various other structures characteristic of the deformation will be developed in the section dealing with modeling. At present, the primary intent is to introduce a simple overall geometry capable of producing the gross structural

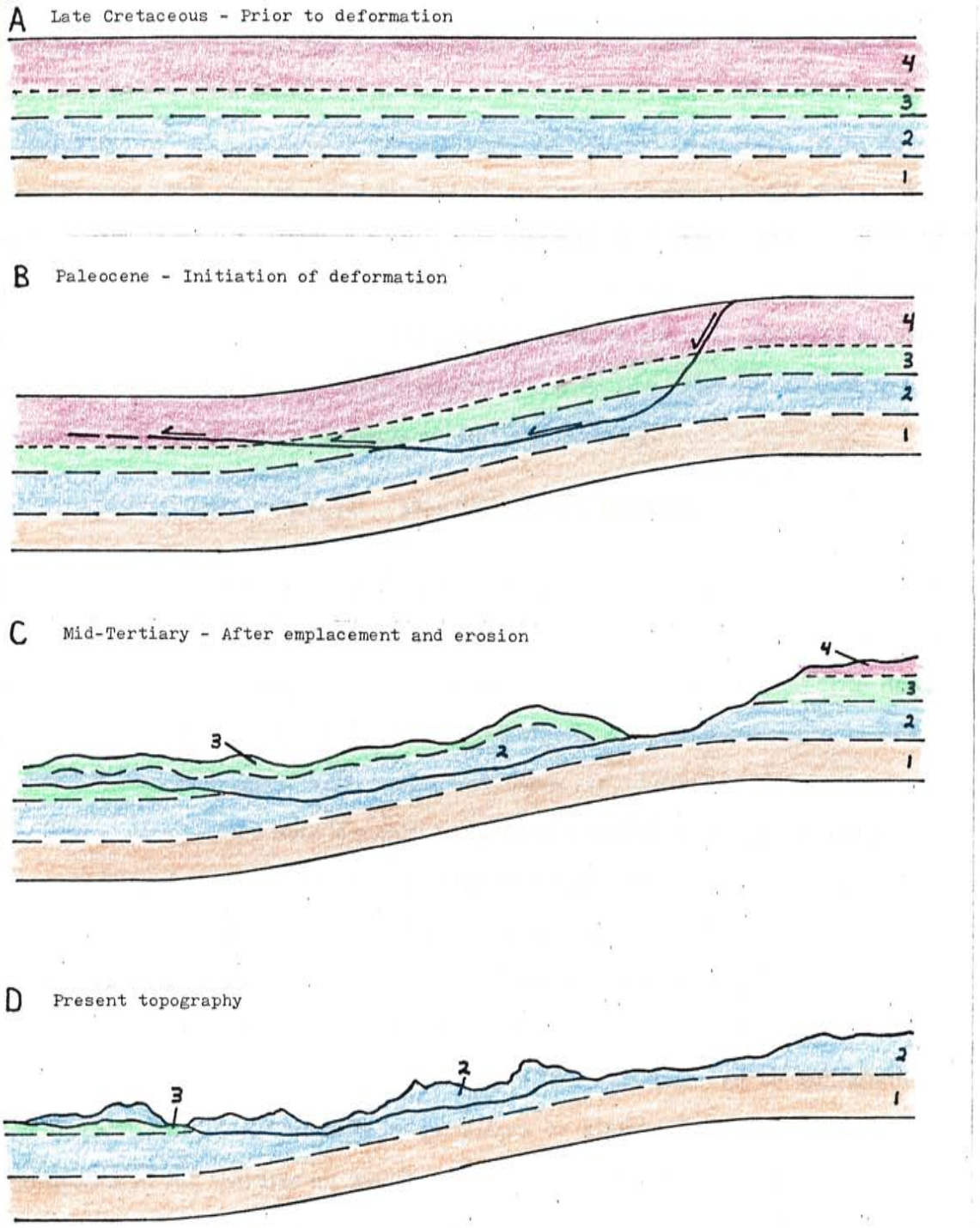

Figure 15. Schematic sequence of events proposed to account for the structural development of the allochthons in the Socorro area.

aspects of the observed deformation.

An interpretation of what the allochthonous sheet may have looked like after its emplacement and erosion sometime in the mid-Tertiary is given in Figure 15C. Most of the superincumbent Cretaceous sediments of section (4) have been removed by erosive processes, and gravitational gliding along the basal detachment surface has moved Permian rocks up over Mesozoic rocks, such as Figure 16 illustrates. With continued erosion, and probably some additional displacement on the décollement, we arrive at the situation depicted in Figure 15D. Here we see that now only isolated remnants, or klippe, of this once largely-continuous sheet are to be found (Figure 17). Not shown in this sketch are the effects of Tertiary faulting.

CHAPTER IV – MECHANICAL MODEL

The phenomenon under study is truly an interesting one, for although all observed deformation takes place well within what are normally strictly brittle conditions, (i.e. shallow depths of burial and low-to-moderate temperature) we find ductile deformation in intimate association with brittle phenomena. This is a consequence of the pronounced variation in mechanical properties which are inherent in the stratigraphic section. The analysis made here is meant to serve as a useful "first approximation" to the structural/mechanical development of the features recorded in the field area. It achieves a measure of success in providing explanations for most of the major structural characteristics noted in the deformation. However, due to the complexity of the structures, the masking effects of alluviation, and the erosion of major portions of the allochthonous sheet, some local interpretations of the field data can be ambiguous.

It is generally difficult to assess by geometric or kinematic considerations alone the significance of the features on which to base structural analogies. This is because tectonic processes are not merely of a geometric nature but, rather, of a mechanical one, being the product of the interplay of forces and deformations. Thus accordingly, the features that constitute the most reliable structural analogies will usually be of a purely mechanical nature, and it is this approach that will be central to this analy-

Figure 16. Outcrop near toe of sheet showing contact of allochthonous Permian strata (Torres Member of the Yeso Formation) where it overrides autochthonous Triassic Chinle.

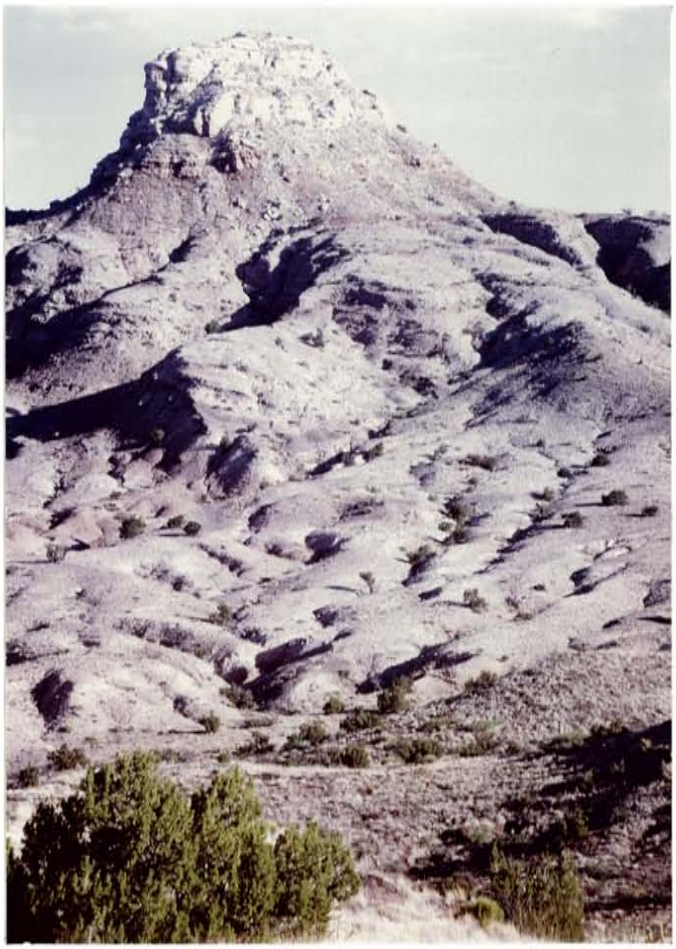

Figure 17. Isolated remnant of allochthonous sheet. Competent Glorieta and Joyita sandstones overlying massive gypsum deposits (plus minor sandstones and limestones) of the Torres Member.

sis. Mechanical and rock-mechanical principals and theories will be combined with the more traditional methods of structural geology to obtain an improved basis for the comparison of structural styles and enhance our understanding of tectonic processes. Knowledge of the mechanics of a structural process implies insight into the development of the associated stress field, a situation which can be of great practical importance.

Gravitational Gliding vs. Compressive Thrusting:

In order to more effectively assess what type of structural features one would expect to find in rock masses emplaced by such mechanisms, it is instructive to compare the basic mechanical differences between these alternatives. Sketches and force-balance equations for scenarios based on the emplacement of thrusts by pushing from the rear versus the detachment and gravitational gliding due to body forces are shown in Figure 18 (Mandl, 1988). For both situations we will be concerned with force components that act on an isolated rectangular segment of the allochthonous sheet, and parallel to the basal shear plane. The dimensions ΔL and T of this rectangular segment should be considered as having unit lengths and thicknesses in the third dimension, respectively, so that the equations correctly represent the balance of forces (stress x area = force). Also note that in each case the shear stresses τ induced along the lower surface will act to oppose the motion of the sheet.

If the sheet is pushed from the rear, as in case A, the magnitude of the thrust-parallel normal stress $\sigma'_{\parallel}$ will decrease in the direction of thrusting because less force is required to overcome basal friction further along the sheet. The situation is quite different if the sheet is moved downslope by $W_{\parallel}$, the slope-parallel component of its own weight W. Here gravitational gliding requires that $W_{\parallel}$ must at least equal the shear forces at the base of the sheet. Usually it will be somewhat in excess of this basal resistance, however, because it also has to overcome some additional buttressing effects at the front of the sheet. As illustrated in Figure 18B, the slope-parallel normal stress will increase in magnitude toward the "toe" of the detached sheet.

For each of these cases, the limit state will be first attained in the part of the

A. Push from the rear

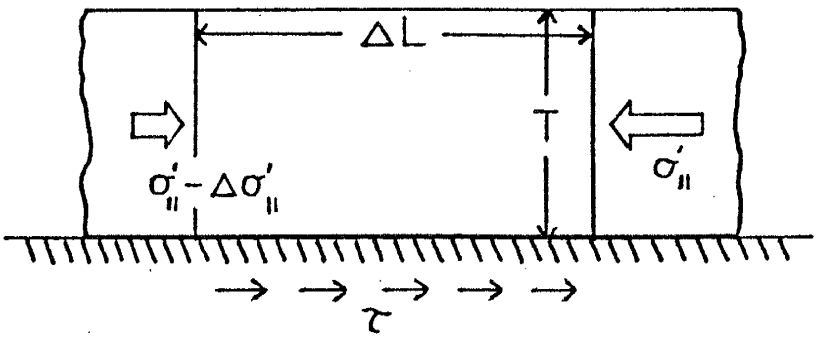

$$\Delta\sigma'_{II} \cdot T = \hat{\tau} \cdot \Delta L$$

B. Gravitational gliding

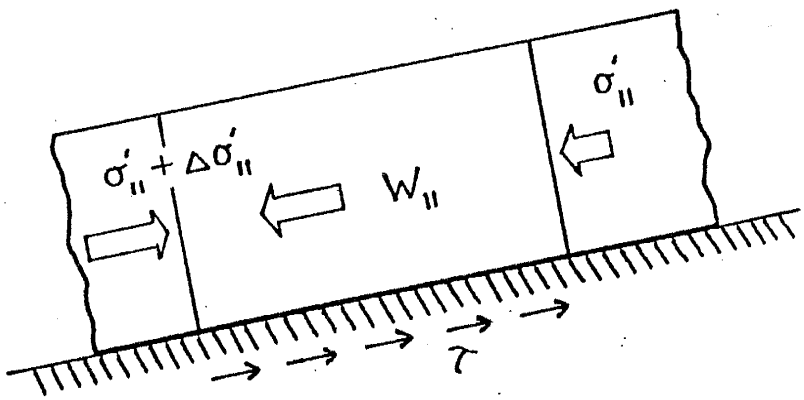

$$\Delta\sigma'_{II} \cdot T = W_{II} - \hat{\tau} \cdot \Delta L$$

Figure 18. Force diagrams illustrating the basic mechanical difference between the emplacement of thrusts by pushing from the rear, and the detachment and gravitational gliding of rock masses due to body forces.

sheet where the thrust-parallel normal stress is greatest. Therefore, when a sheet is pushed from the rear, we would expect compressive failure to occur near the back end, and in the gravitationally gliding sheet such faulting should begin near the front (see Figure 14). As we shall see in a subsequent section, this reasoning does not exclude the possibility of faults (either extensional or compressional) from forming at other locations within the sheet where factors such as frictional resistance, dip angle, or sheet geometry locally induce contact with the limit state.

Emplacement of the allochthons by compressive thrusting has several major problems with it that cannot be supported by the field and experimental evidence. Specifically, if the allochthons were emplaced by such a mechanism, why do we not see any widespread development of stylolites perpendicular to bedding? It has already been noted that stylolite formation commences at stresses of $\approx$ 2.25 MPa, values characteristic of overburden loads of about 90 meters of sediments. Using the analytical approaches of Raleigh and Griggs (1963) and Murrell (1981), we can calculate the compressive stresses required to move the allochthonous sheet up a thrust ramp structure. Under even the most optimistic of physical circumstances – i.e. high pore pressure ($\lambda = 1$), basal shear strength = 0, and shallow ramp angle (20°) – the requisite stress exceeds the minimum stress for stylolite formation by at least an order of magnitude. The absence of stylolites perpendicular to bedding in the limestones of the San Andres Formation and the lack of overall compressive strain profiles in the allochthons is evidence against a thrust hypothesis. Also, aside from the previous mechanical discussion, there is no field evidence of horizontal thrusting in the suurounding regions . Indeed, the predominant mode of deformation appears to be that of vertical tectonics. Thus it is shown that several significant arguments restrict compressive thrusting from being seriously considered as a viable tectonic alternative. The nature of the kinematic indicators present (as well as those absent) and the positions within the allochthons at which they are noted, suggest that of the two possible mechanisms, gravitational gliding versus thrusting, the former is preferred.

Determination of Rock-Mechanical Properties:

In order to more realistically evaluate these competing tectonic scenarios, it is necessary to know the value of certain elastic moduli so that representative mechanical models can be constructed. Various rock-mechanical methods were used to obtain this information, specifically, uniaxial and polyaxial compression, ultrasonic-pulse techniques, "constant force" tests, and bevelled shear dies. Detailed descriptions of these procedures and the equipment employed are given in Linden, (1987). Physical properties such as, Young's modulus, compressional strength, shear strength, the modulus of rigidity, viscosity, and characteristic relaxation time, of several critical rock types involved in the deformation were determined. The results of these investigations are listed in Figure 19 according to lithology, physical property measured, and method employed. The data on which these experimental results are based are given in Appendix B.

Tests using ultrasonic-pulse determinations of the compressional and shear wave velocities in several of the rock types were made in order to calculate dynamic values of E and G. This was done to serve as a check of the values of these moduli obtained by static methods. In addition to these tests, experimental information taken fron the rock-mechanical and geophysical literature is also included. These values appear in parentheses, with the source of the information indicated by the accompanying numerical superscript. Some of these will prove to be quite valuable as we develop our model of allochthon emplacement; in particular, τ_C, the critical shear stress reported by Williams (1988).

The actual numerical values of the mechanical properties measured for each lithology investigated are somewhat dependent on the type of experimental test used and the nature of the measuring/recording set-up. What is perhaps more important are the *ratios* obtained when these properties are compared for various rock types. This gives a first approximation as to what the gross properties of the sedimentary sequence are, which, in turn, is helpful in constructing mechanical models and physical analogs.

Physical Property /Test Used	Lithologies Tested		
	Pyc/Pyt Gypsum	Pyt Limestone	Pg Sandstone
Young's Modulus E* (GPa)	5.11	43.48	2.74
Compressional Strength C* (MPa)	26.37	97.66	48.00
Shear Strength S** (MPa)	1.42 τ_U (0.58-1.36)[2] τ_C (0.20-0.56)[2]	—	9.81
Compressional Velocity V_P† (km/sec)	1.51	4.07 (2.52-4.76)[1]	— (4.55)[1]
Shear Velocity V_S† (km/sec)	1.04	2.72	—
Young's Modulus E† (GPa)	5.20	42.22	—
Shear Modulus G† (GPa)	2.46 (2.02-2.85)[2]	19.24	—
Viscosity μ‡ (10^{17} Pa-sec)	4.36	—	—
Relaxation Time r ‡ (10^7 sec)	8.54	—	—
Density ρ (gr/cm^3)	2.29	2.60	2.25

*Uniaxial compression
**Bevelled shear dies
†Ultrasonic-pulse
‡Constant force test

(1) Brocher, 1981
(2) Williams, 1988

Figure 19. Summary of experimentally determined elastic properties characteristic of rocks involved in the deformation.

Deformational Characteristics and Rheological Nature of Gypsum

Gypsum possesses a variety of qualities that makes it the prime "deformational catalyst" in our sedimentary package:

1. being hydrated calcium sulfate, the water in the lattice structure will be liberated as temperature increases above $\approx 50°$ C at a depth of 1.0 kilometer (Heard and Rubey, 1966; Murrell and Ismail, 1976),
2. initially, it possesses very little (if any) porosity, a condition which will generate high fluid pressures when water is released (Guth and others, 1982),
3. the gypsums are very fine-grained, a condition which favors recrystallization-based deformation (Müller and others, 1981), and
4. they are interlayered with materials which have drastically different mechanical properties, viscosity in particular, and will react in a ductile manner under the conditions that exist in the subsurface (Gretener, 1972; Johnson, 1984).

We shall see that this combination of chemical composition, initial depositional features, rheology, and overall stratigraphic geometry is conducive to the generation of the deformational features observed in the field area. The following discussion assumes that the evaporites were originally deposited as gypsum, and not as anhydrite. If this latter condition were the case, the model proposed would not be severly compromised because the rheological properties of anhydrite closely resemble those of gypsum (Müller and others, 1981).

Figure 20 is a graph of the pressure-temperature-depth relationships between anhydrite and gypsum, and illustrates the significance of point (1). At a depth of one kilometer the vertical stress σ_1 is estimated to be 25.0 MPa (where $\sigma_V = \rho g z$, $\rho = 2,550 kg/m^3$, $g = 9.80 m/sec^2$, and $z = 10^3 m$). If we assume a geothermal gradient dT/dz of 30° per kilometer we see that at a depth of one kilometer the gypsum will have begun to undergo dehydration.

Some additional experiments to determine the rheological characteristics of the Pyc/Pyt gypsum deposits were performed using what is called the "constant force test" (Rutter, 1972). Using this procedure, a core of gypsum was subject to passive

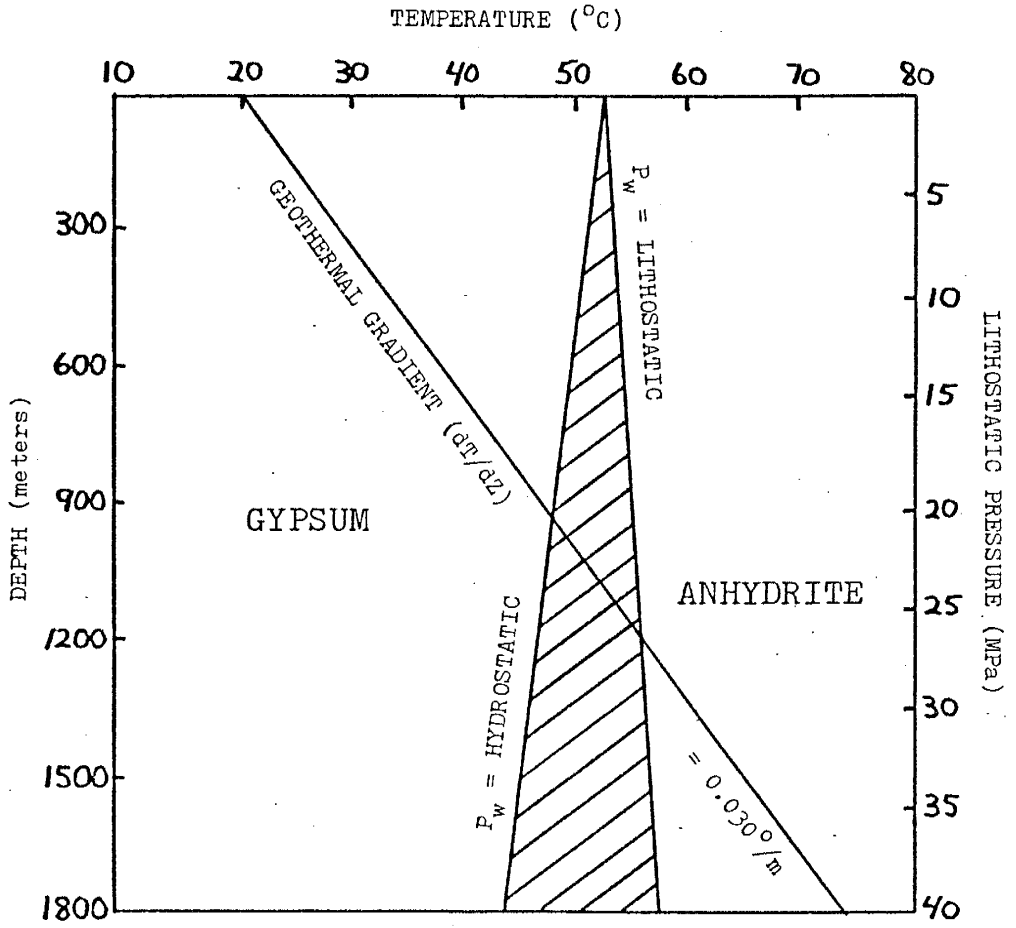

Figure 20. Graph of pressure-temperature-depth relationships between gypsum and anhydrite (modified from Hanshaw and Bredehoeft, 1968).

gravitational loading for an extended period of time (56 days) and its deformation monitored using an LVDT (linear voltage differential transformer) and a strip-chart recorder. The time-strain curve (see Figure 21) produced in this manner yields information regarding the materials mechanical behavior. Results of such a test (data tabulated in Appendix B) show that the material reacted as a Maxwell elasticoviscous substance (see Appendix A).

Two important physical quantities were determined from analysis of the experiment, the viscosity of the material and its characteristic stress relaxation time. Viscosity is the measure of the resistance of a material to flow, i.e. of the internal friction between contiguous layers in relative motion to one another. This calculation requires knowledge of the stress-strain relationship of a Maxwell elasticoviscous body as derived in equation [A–7], Appendix A

$$e_T = \frac{\sigma}{E} + \frac{\sigma t}{\mu}. \qquad [1]$$

Solving this expression for μ, the viscosity, we obtain

$$\mu = t\left(\frac{e_T}{\sigma} - \frac{1}{E}\right)^{-1}. \qquad [2]$$

Substitution of the experimentally determined values of t (test duration in seconds), e_T (total strain), σ, and E (see Figures 19, 21, and Appendix B, p. 95) yields a viscosity of 4.36 x 10^{17} Pa-sec ($ML^{-1}T^{-1}$) for the gypsum. This is in good agreement with gypsum viscosities reported in the literature (Kehle, 1970). An interesting property of Maxwell bodies is that, provided strain is kept constant, the stress contained within the body will relax exponentially (see Appendix A for derivation of the expression for stress relaxation). The period over which the stress will decay to a value equal to σ_0/e (initial stress divided by Euler's constant) $\approx 0.37\sigma_0$ is called the relaxation time, r. This quantity is calculated by taking the ratio of the viscosity modulus to the elastic modulus

$$r = \frac{\mu}{E}. \qquad [3]$$

When these values are substituted we find that the relaxation time for the Torres/Cañas gypsum is 8.54 x 10^7 sec which is $\approx$ 2.71 years. As far as rocks go, this

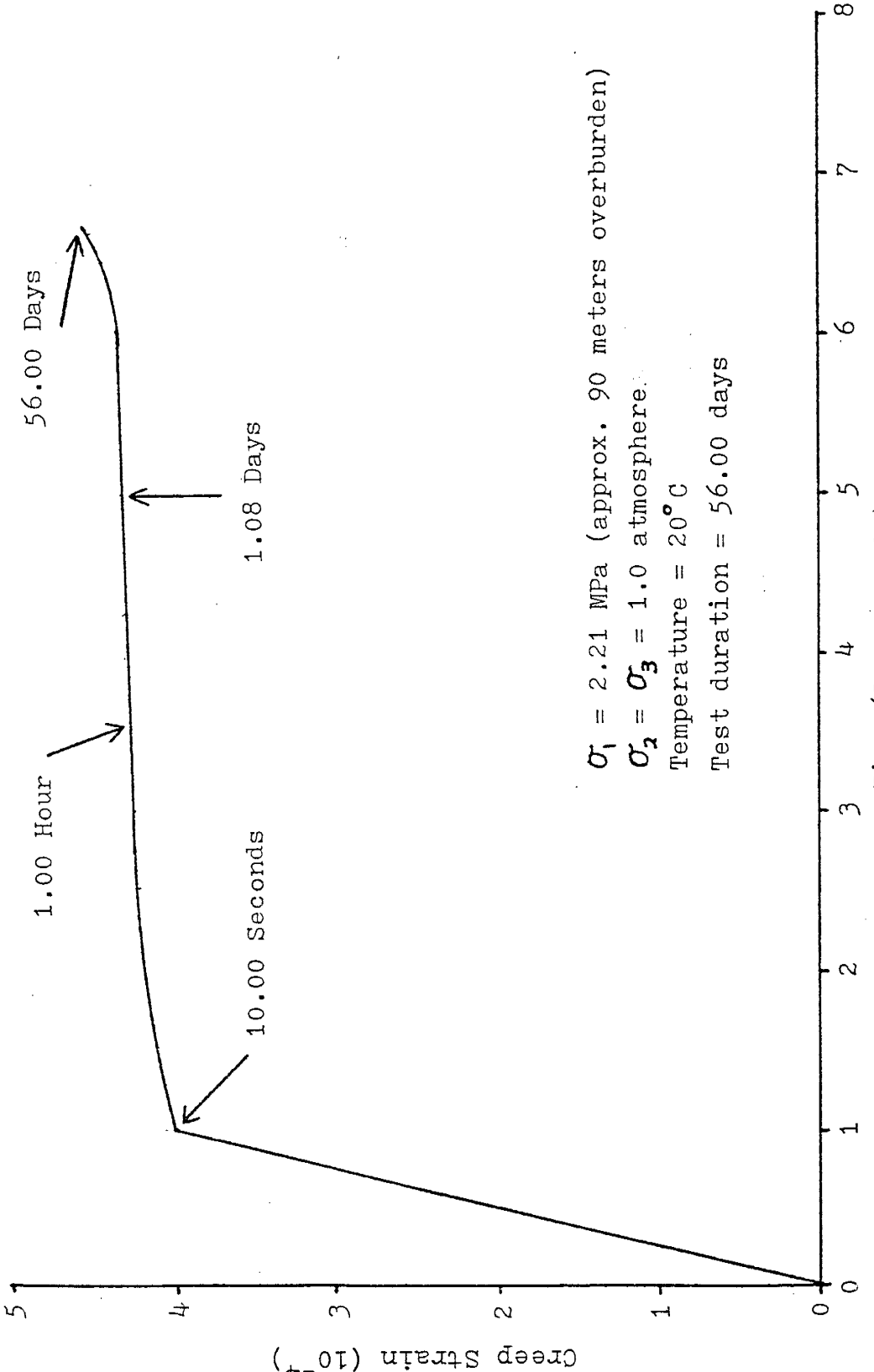

Figure 21. Time-strain curve produced by Pyc/Pyt gypsum in "constant force" test.

is an extremely rapid relaxation time, but such is the rheological nature of this material. Essentially, the gypsum is reacting as a viscous fluid – when it is subject to loads in excess of τ_C, the critical shearing stress, it will continue to strain at a rate equal to $\sigma t/\mu$. As soon as the load is removed it will begin to dissipate the stored stress as it seeks to attain a hydrostatic state. Figure 22 illustrates the stress relaxation curve derived from the creep experiment performed on the gypsum (calculations presented in Appendix B).

Flow due to inelastic shearing in a Newtonian viscous fluid will continue without altering the limit state of stress. This is a consequence of the fact that such a material does not undergo changes in mechanical properties and shows no "memory" of past inelastic shearing. Therefore, the stress cannot be related to the total inelastic shear strain, but only infinitesimal increments of strain, or to strain rates, when referred to some infinitesimal time interval (Ranalli, 1987).

Influence of Pore Pressure on Thrusting Phenomena

The thermodynamics of the gypsum dehydration reaction indicates that conversion will occur at shallow depths ($\approx$ 1.0 km) and produce fluid at a constant rate. Hanshaw and Bredehoeft (1968) have constructed a model which requires that the head in the source bed at a particular depth rises in a relatively short time period and then remains constant. Heard and Rubey (1966) indicate that the excess water produced in a bed of gypsum 16.1 meters thick is equivalent to a layer of water 738 cm thick; half of this, or approximately 370 cm, would flow into the overlying layer, and half into the underlying layer. Calculations of the excess-head distribution in the adjacent layers at 45,700 years after the onset of dehydration have been made and are plotted in Figure 23, where the parameters K and S_s respectively refer to the hydraulic conductivity and the specific storage (the volume of water taken into storage or discharged per unit volume per unit change in head). Several important results emerge from their computations. Gradients near the source bed are much greater in the early stages of flow than when the steady-state is reached. Also, the resulting head change has migrated only about 20 meters from the source layer – all

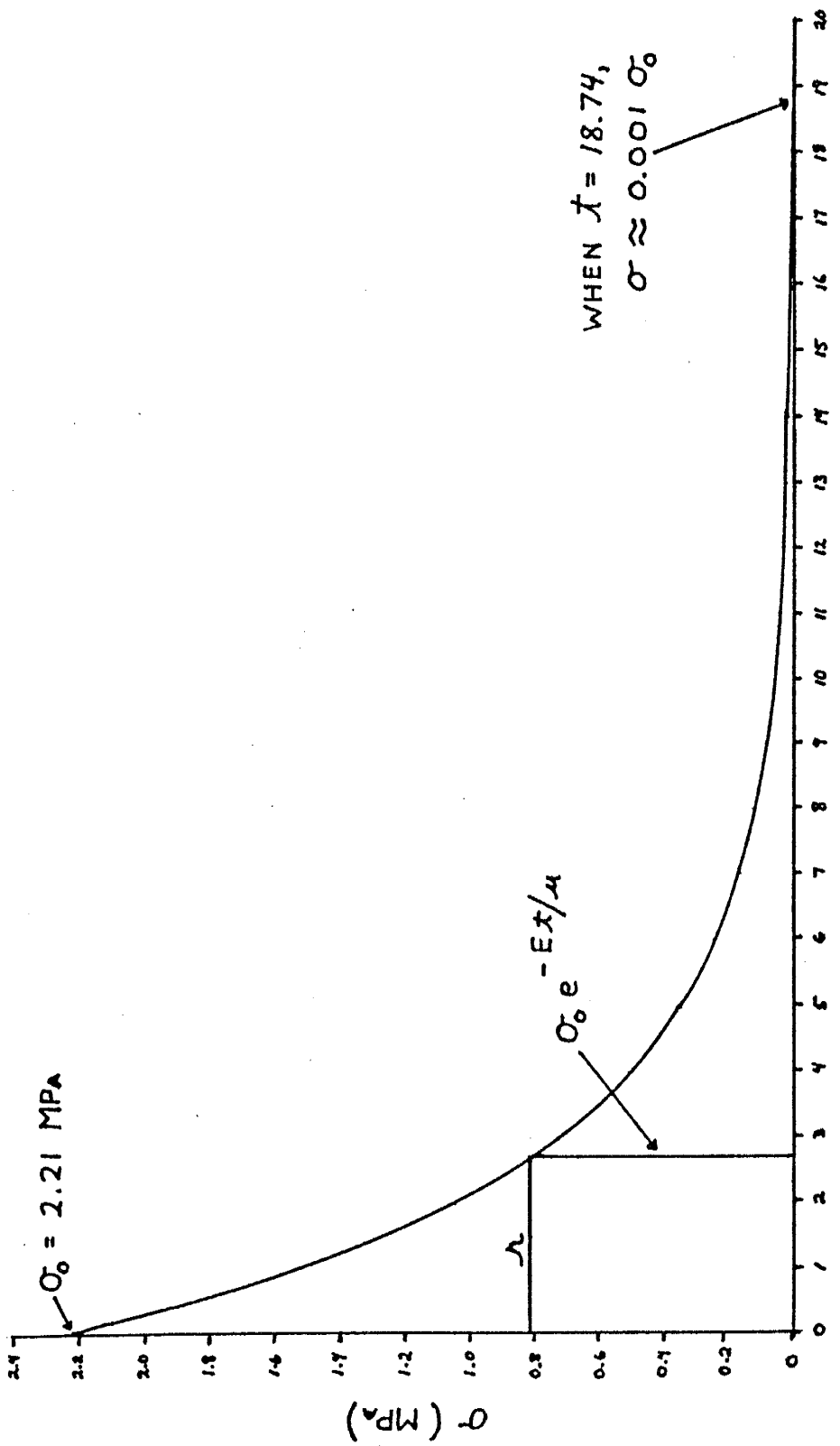

Figure 22. Stress-relaxation curve derived from the experimental response of core samples of Pyc/Pyt gypsum to gravitationally imposed stress during "constant force" test.

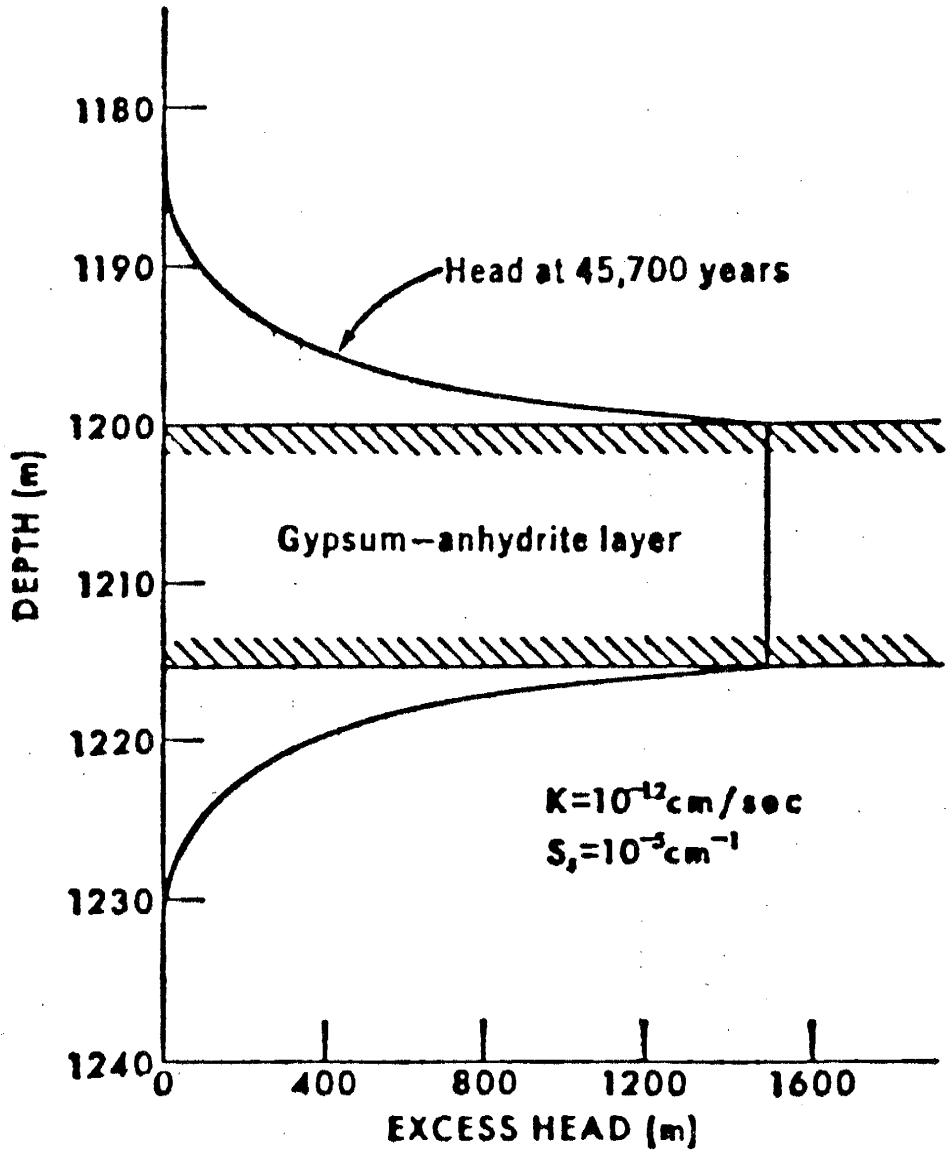

Figure 23. Excess-head distribution at 45,700 years (from Hanshaw and Bredehoeft, 1968).

the water derived from the dehydration reaction is stored within this interval.

The water driven from the lattice structure will produce elevated pore pressures in the evaporite layers. When such a condition is combined with sediments which rest on a slope, shear stresses are introduced which can initiate gravitational gliding. Under these conditions, the slope requirements to produce shear stresses large enough to exceed τ_C (0.20–0.56 MPa) (Williams, 1988) turn out to be modest, indeed. The calculation of this induced shear stress is performed in the following manner.

Given a block which rests on sloping, overpressured substratum, a portion of the vertical stress will be converted into a component of shear stress which parallels the basal surface. The ratio of conversion is dependent upon the sine of the slope angle; expressing this symbolically yields

$$\tau = \sigma_V sin\delta \qquad [4]$$

where δ is the angle of slope. The problem is to determine what is the smallest angle required to equal or exceed the critical shearing stress for the weak gypsum layers. This can be expressed in the form of an inequality, $\tau \geq \tau_C$, so we get

$$\sigma_V sin\delta \geq \tau_C \qquad [5]$$

or, in a more useful form

$$\sin\delta \geq \frac{\tau_C}{\sigma_V}. \qquad [6]$$

Entering values of 25.0 MPa (stress at a depth of one kilometer) for σ_V and 0.20 MPa for τ_C (Williams, 1988), respectively, we see that *a slope as little as 0.5 degrees is sufficient to induce translation gliding of the gypsum and facilitate movement of the allochthonous sheet.*

The Coulomb-Mohr Failure Criterion

Observations of small-scale faulting phenomena resulting from a wide variety of soil and rock tests lead to the general conclusion that the onset of faulting requires that critical values of σ_1 and σ_3 be attained. The stress states that lead to failure are best represented by means of the Mohr diagram for stress, a graphical method

which illustrates the relationship between the magnitude of normal and shear stresses and the orientation of the planar element on which they operate (Means, 1976). The collective set of all such limit stress circles defines the Coulomb-Mohr failure envelope, the linear portions of which are described by

$$|\tau| = S_o + \sigma'_N \tan\varphi \qquad [7]$$

where φ is the angle of internal friction and S_o is the shear strength of the material (Ramsay, 1967; Mandl, 1988). For the majority of rocks this function is approximately linear in the compressional stress range up to about $\sigma' = 100$ MPa, well within the stress range we will investigate in this study. Figure 24 illustrates a typical limit stress state and the elements in physical space upon which the components of stress operate.

Numerous successful applications in rock mechanics underscore the utility of this limit condition. Its striking simplicity is mainly a consequence of its independence from σ_2, the intermediate principal stress, an approximation which appears quite acceptable for most applications of rock mechanics and structural geology (Jaeger and Cooke, 1979). This method is particularly convenient for the two-dimensional analysis of planar features such as faults, joints, and fractures, and subsequently forms the basis for many of the mechanical arguments presented in this investigation.

The primary controlling factor in the brittle mode of deformation is the effective confining pressure σ', which is defined as the total confining pressure σ_T minus the fluid pressure p, or

$$\sigma' = \sigma_T - p = \frac{(\sigma_1 + \sigma_3)}{2} - p \qquad [8]$$

for the two-dimensional case. Hereafter, any stresses that appear primed will refer to effective stresses. In the analysis that follows, compressive stresses will be considered positive, tensile stresses will be negative, and σ_1, σ_2, and σ_3, the principal stresses, will be algebraically ordered so that $\sigma_1 \geq \sigma_2 \geq \sigma_3$.

Mohr's Stress Analysis and the Pole to the Stress Circle

Whenever possible, analytical derivations have been replaced with the extremely useful, and elegant graphical method of Mohr's stress/strain circles. But, although

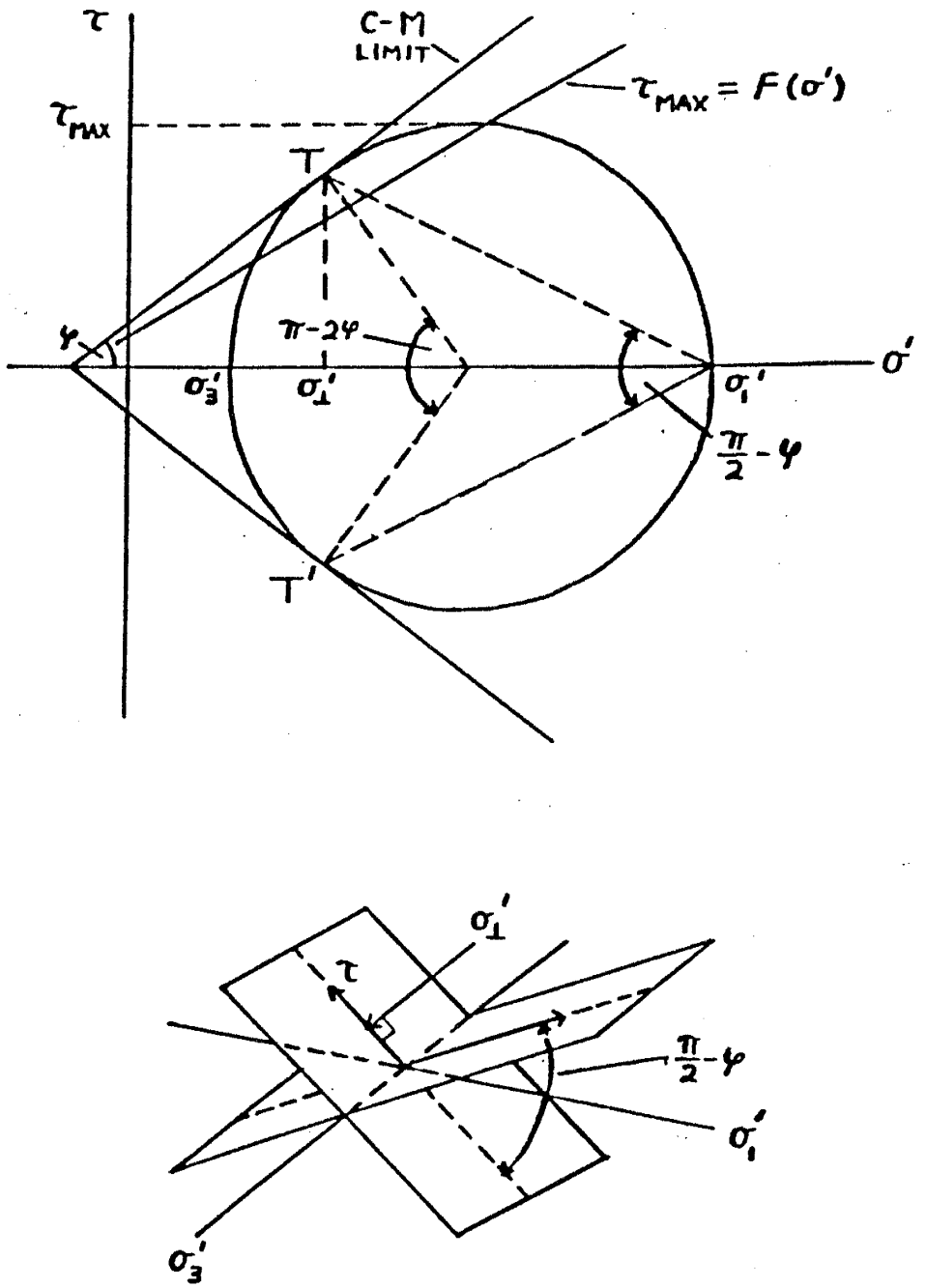

Figure 24. (A) Limit stress states in Mohr's stress plane. (B) Elements in physical space upon which the stress components of T and T' of figure A operate.

the Mohr construction has great utility in determining stresses on a particular plane given the values of the principal stresses, it does not provide any information with regard to the orientation of that plane in physical space. This problem can be solved by what is termed the "pole", another useful construct in representing second order tensors. The pole of the Mohr circle provides a link between abstract stress or strain space, and real, physical space. It allows us to attribute a geographical direction to any particular state of stress we are interested in. In the analysis of two-dimensional stress (σ_1 and σ_3), the pole is parallel to the σ_2 direction, i.e. perpendicular to the plane of the Mohr diagram. By definition, the line from a stress point on the Mohr circle to the pole is parallel to the trace of the physical plane on which the stress operates (Mandl and Shippam, 1981; Allison, 1984). For the purposes of this study, the most useful state of stress and its corresponding orientation in space is that concerning the direction of σ_1, the greatest principal stress. Since σ_1 acts perpendicularly on the element represented by the chord connecting the stress point to the pole, we can quickly determine the orientation of stresses in physical space. Figure 25 illustrates the use of the stress pole for the case in which it is coincident with σ_1. More detailed explanations and examples of the various properties of the pole are given in (Mandl, 1988).

Active vs. Passive Modes of Failure

So far, no statement regarding the mode of faulting itself has been made – the Coulomb-Mohr limit has been considered as a purely static statement on stress states that give rise to faulting. There are, however, different failure modes which result from particular states of stress. Consider a stack of horizontal strata subject to an effective vertical normal stress σ'_V determined by the weight of overburden minus fluid pressure (here being the most compressive stress), and initially free of horizontal shear stresses. In this situation the stresses on a horizontal plane can therefore be represented in Figure 26 by point σ'_V on the σ'_N axis, and the two effective horizontal normal stresses σ'_H will be equal and represented by σ'_3. This section of strata will not yet be in a limit state and requires tectonic activity to raise or lower the imposed

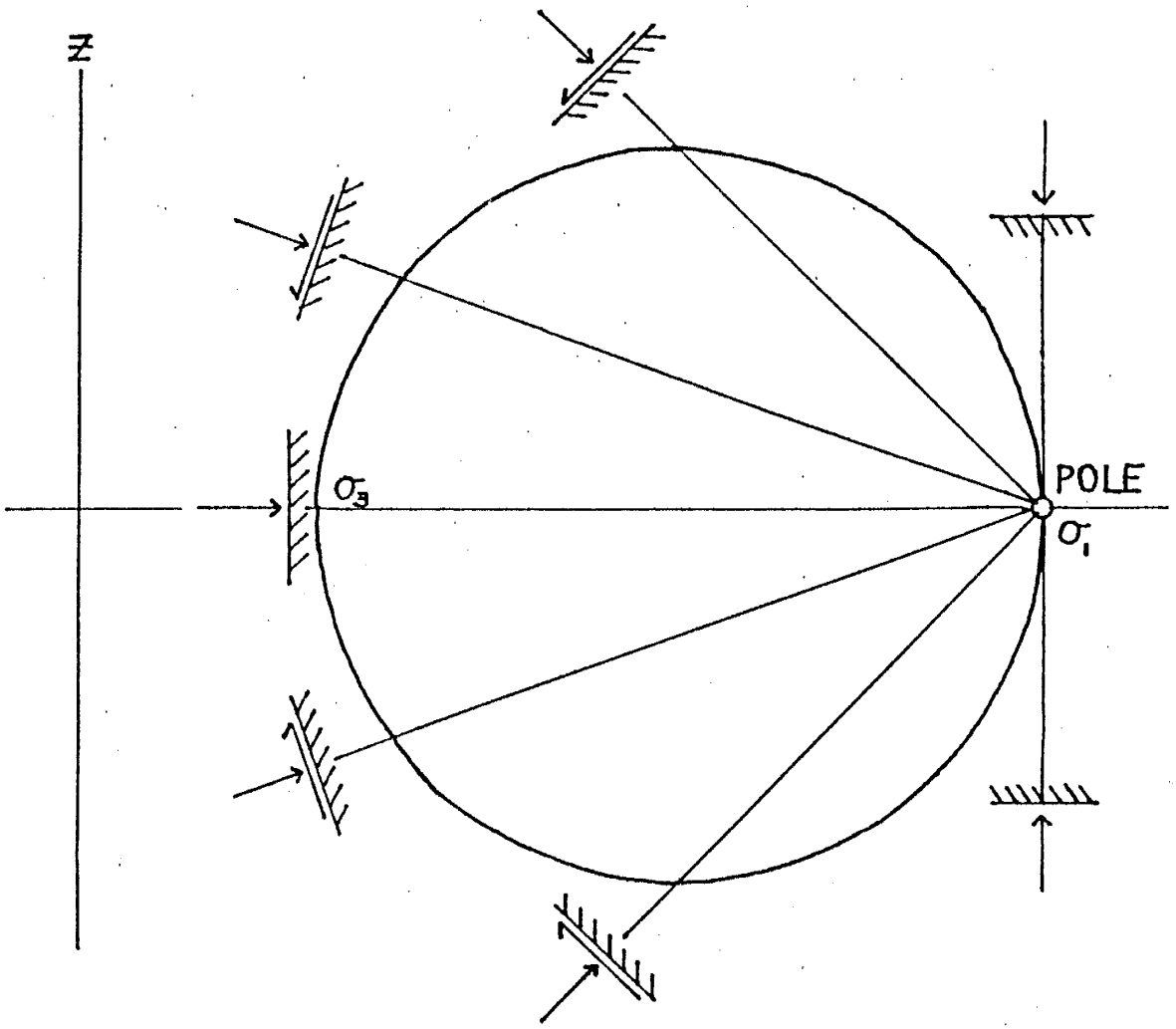

Figure 25. Mohr circle for stress demonstrating use of the pole. Case where stress axes are aligned with geographical axes as shown and σ_1 is vertical; pole is coincident with σ_1 point.

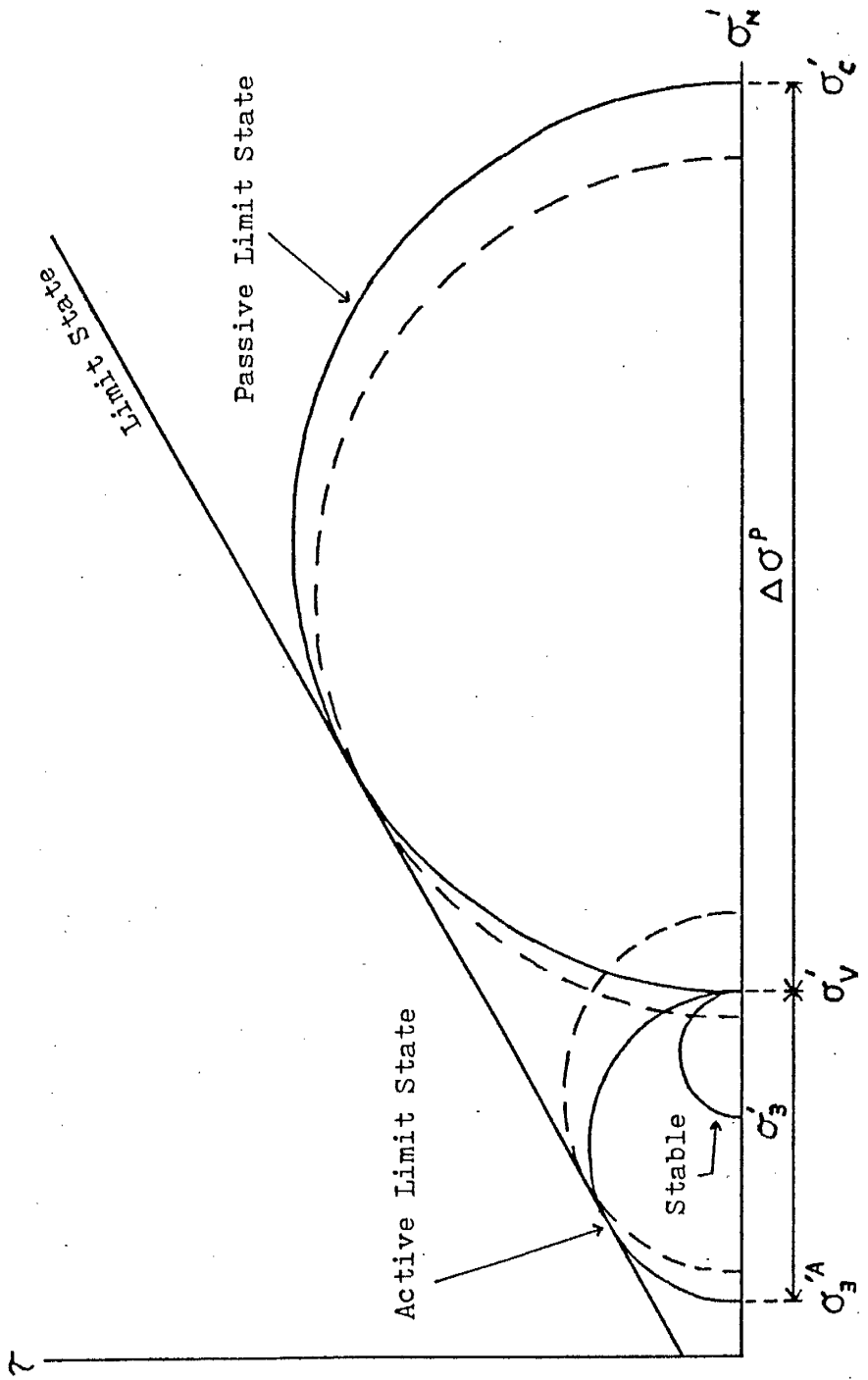

Figure 26. Duality of tectonic limit states in horizontal strata – Active versus Passive modes of failure.

horizontal stresses. The introduction of a horizontal extension leaves the role of σ'_V as the greatest principal stress unchanged. The effect of a modest reduction in horizontal normal stress (σ'^A_3) is to induce a limit state in which normal faulting is possible and the rock mass may undergo further extension in the horizontal dimension.

If however, horizontal compressive stresses are applied, a much greater change in stress ($\sigma'_H \rightarrow \sigma'_C$) is required to attain the second type of limit state. Due to the shear-strength-increasing-effect attending a rise in confining pressure, the differential stress (the diameter of the Mohr circle) associated with the compressive limit state will usually be from three to four times the stress difference required for extensional failure. Thrust faulting in this limit state will accomodate lateral shortening of the rock mass. In accordance with soil mechanics terminology, the compressional limit state will be referred to as the "passive" limit state, whereas the extensional limit state will be called the "active" limit state. As a consequence of the pronounced difference in differential stress between these two limit states, material will generally be much more deformed in tectonic shortening by thrust faulting than by the normal faulting which is characteristic of extension.

There is yet another implication of the difference between active and passive failure that needs to be addressed; in particular, the switching of fault style which may occur during a single tectonic episode. Given a situation in which a sedimentary sequence is free from tectonically imposed horizontal stress, σ'_V is the greatest principal stress. Generally it will remain a principal stress if either horizontal extension or compression is imposed on the rocks, but it may no longer retain its role as the greatest principal stress. Critical stress states such as the dotted examples in Figure 26 then become possible — these situations are characterized by wrench faulting. Hence, it is shown that the conditions of stress for extension/thrusting and wrench faulting may lie quite close together, and that relatively minor changes in applied horizontal stress may induce a switch from either normal faulting or thrust conditions to those which produce strike-slip faults.

Flattening of the Basal Fault

Non-tectonic forces, such as variation in shearing strength, may cause flattening of a fault. Given a uniform stress field, a fault which cuts across the interface between a sedimentary rock with a high friction angle (i.e. Glorieta sandstone) and one with low frictional resistance (Cañas/Torres gypsum), may change its orientation with respect to a uniform σ_1 direction. The effect of variation in shear strength is magnified when an additional shear stress acts on the interface between competent and incompetent layers. Such a situation is commonly observed in the case of dipping beds where gravity induces shearing stresses along bedding planes.

When superincumbent strata are displaced over underlying sediments towards regions of high curvature, such as anticlinal crests or uplifts associated with faulting, interstratal shear stresses are introduced by the flexure of this stack of alternating strong and weak strata. Such a situation is demonstrated by the stress diagram in Figure 27 for two mechanically different lithologies involved in the type of deformation we are investigating. This analysis (adapted from the work of Mandl, 1988) will consider how the physical properties affect a normal fault which cuts across the interface, and accordingly, the following stress diagrams were constructed using the rock mechanical data presented in Figure 19 and Appendix B, corresponding to the Glorieta Sandstone and the Torres and Cañas gypsum deposits.

Both lithologies have to be in their respective limit states, therefore, each stress circle must touch the corresponding limit line. An additional requirement will be that the fluid pressure be equal on both sides of the interface so that both the tangential and effective normal stresses must also have the same value across this interface. These criteria are fulfilled at only one point on the resulting diagram, here labeled A, where the two circles intersect. By means of the stress pole construction the direction of σ_1' can be found for each rock layer. This is done by simply drawing a straight line through the points where the interface (horizontal dotted line) cuts each limit circle to represent the planar element that is acted upon in real space by the stress components of A. It is important to note that upon entry into the weaker beds (inset

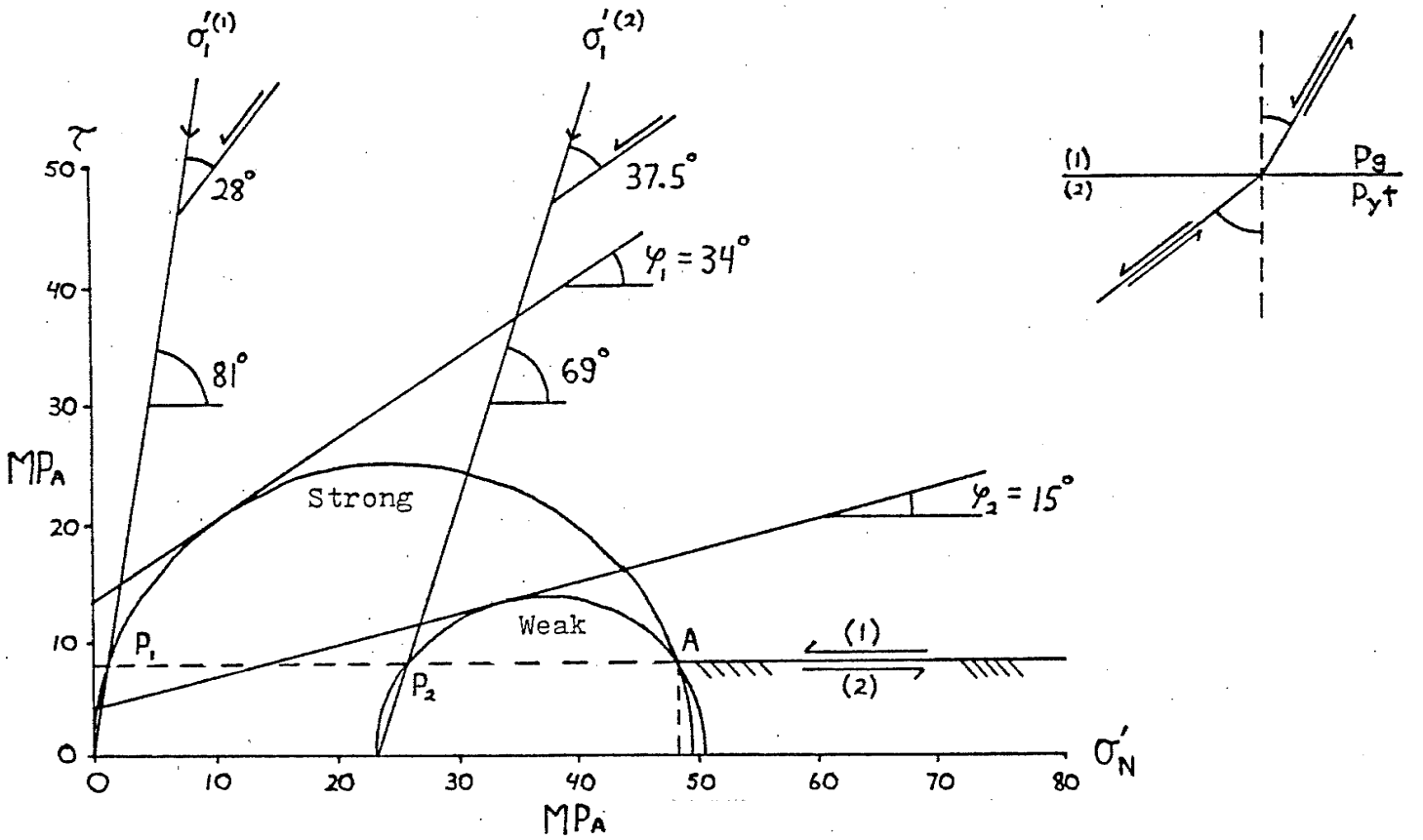

Figure 27. Flattening of a normal fault upon entering a weaker layer. Determination of the change in direction of the maximum compressive stress and associated slip elements by the pole-method in Mohr's stress space.

Figure 27), the σ_1' direction undergoes a refraction with respect to the interface – this implies a concommitant flattening of the associated slip elements. The amount of refraction is calculated by taking the difference in orientations of σ_1' in the respective lithologies (Pg = strong) and (Pyt/Pyc = weak), and adding this to the difference between the angles characteristic of the slip elements in these lithologies. Under the conditions given in the figure the σ_1'-directions associated with the respective lithologies would differ by 21.5°: ($81° - 69° = 12°$, $37.5° - 28° = 9.5°$, so $12° + 9.5° = 21.5°$ change in fault attitude). Of prime importance here is that when cutting through an interface of contrasting shear strength, the incipient fault not only changes the angle it makes with the σ_1 direction, but that *the σ_1 direction itself is changed.*

The competent/incompetent interface can be considered as a plane of superweakness, for not only does a strong mechanical contrast exist across this surface, but it is also the region which is most likely to be subject to elevated fluid pressures. An effect similar to the change in dip angle observed due to a frictional contrast between adjacent sedimentary layers is also noted in such circumstances involving high pore pressure. Consider a sequence of strata in which overpressured sediments are overlain by normally pressured beds. The layers are somewhat inclined, so the weight of the overburden induces some shear stress along bedding planes. Figure 28 shows the nature of the stresses across the interface and how they change as one goes from normal to overpressured situations. Increased pore pressure causes a decrease in the magnitude of stresses which operate normal to surfaces; only the shear stress does not change across this interface. By arguments similar to that presented for the case of rocks with a strong competency contrast separated by an interface, one can show that a normal fault will flatten abruptly when it passes from the normally pressured sediments to the overpressured region. This change in dip will only occur when a shear stress acts along the bedding, otherwise, the fault will intersect the top of the overpressured region undeflected.

Development of the Thrust Toe

The varied nature of the lithologies in our stratigraphic sequence insures that

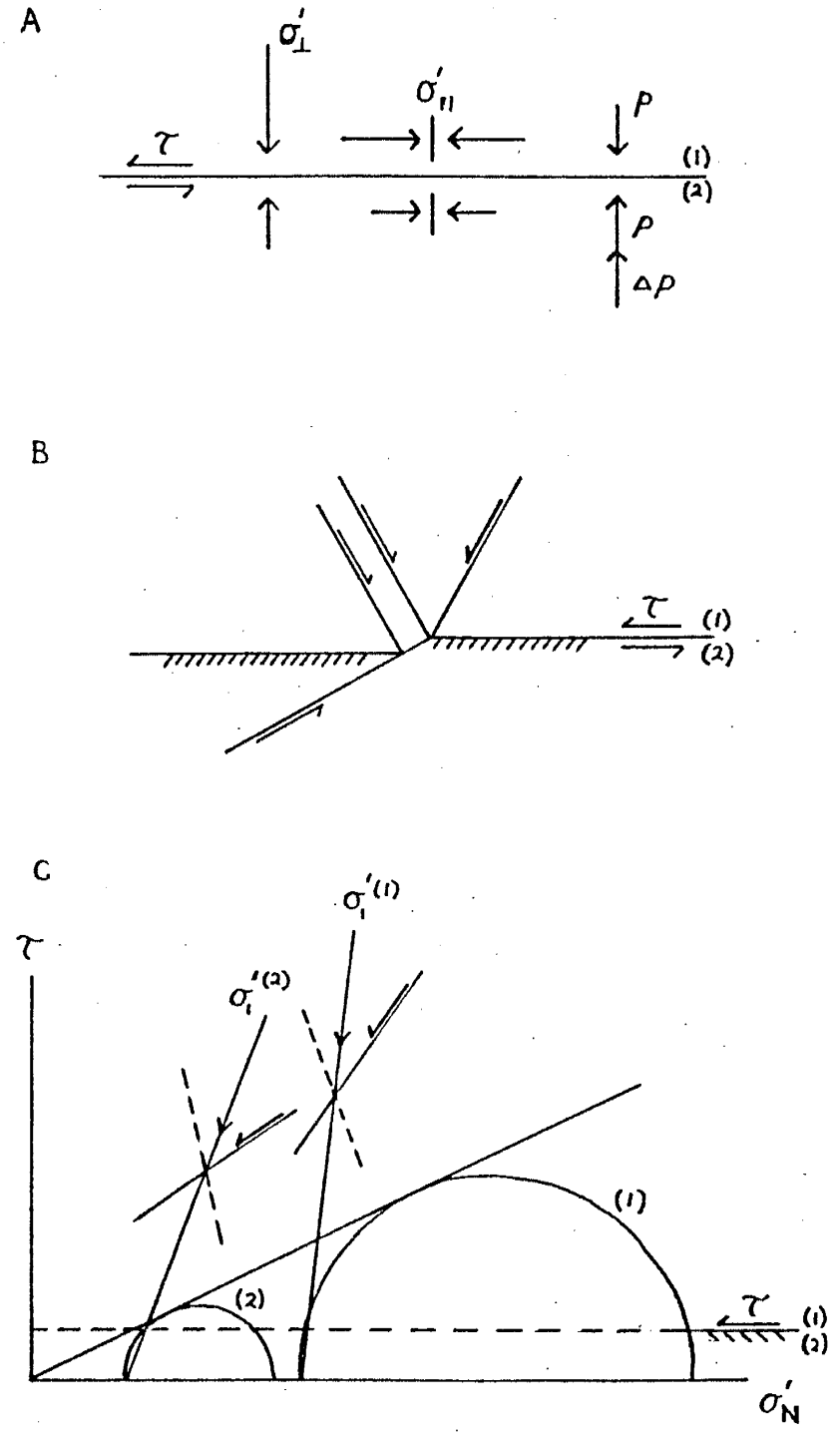

Figure 28. Refraction of a normal fault upon entering an overpressured layer subject to shear stress.

individual layers will undoubtedly differ markedly in their mechanical properties (see also Figures 19, 27, and Appendix B). Compression of such a layered medium will lead to a stress distribution dictated by the elastic properties of the layers. Competent layers such as the massive carbonates and sandstones will act as beams and become highly stressed. Until these layers undergo failure, either by folding or faulting, it is not possible to apply any significant load to the intervening incompetent members (weak sandstones and evaporites). Only upon failure of the competent beams can the load be suddenly transferred to the adjacent incompetent lithologies.

Figure 29, adapted from the work of Gretener (1972), illustrates this situation via Mohr analysis. Failure envelopes (limit states) for both the competent and incompetent lithologies are shown. The large solid Mohr circle refers to the state of stress which exists in the competent beam immediately prior to failure, whereas the smaller solid Mohr circle represents the stress state in the adjacent incompetent material at this time. Note that the effective overburden stress σ'_V is of the same magnitude in both layers. Also, the effects of high pore pressure will not be introduced in this analysis, although such effects would cause a shift of the Mohr circle to the left and further facilitate the process described below.

At the moment the large solid Mohr circle encounters the failure envelope for competent rock, a compressional structure (either fold or fault) forms (shown by the sequential collapse of the large Mohr circle) and the stress is transferred to the adjacent incompetent lithologies. This loading will be quite rapid, geologically speaking, and it is probable that the additional stress will be carried by the fluid portion of these weak, often poorly permeable beds, rather than by the matrix. The result is that there is a reduction in the pressure due to overburden, and the small solid circle corresponding to the stress state in the evaporites/weak sandstones will grow in the manner shown in the figure. Figure 30, which is a more detailed enlargement of the left portion of Figure 29, provides information concerning the production of slip surfaces within the weak sediments. As stress is transferred from the competent beams to the adjacent sandstones and evaporites, the size of the Mohr circle representing

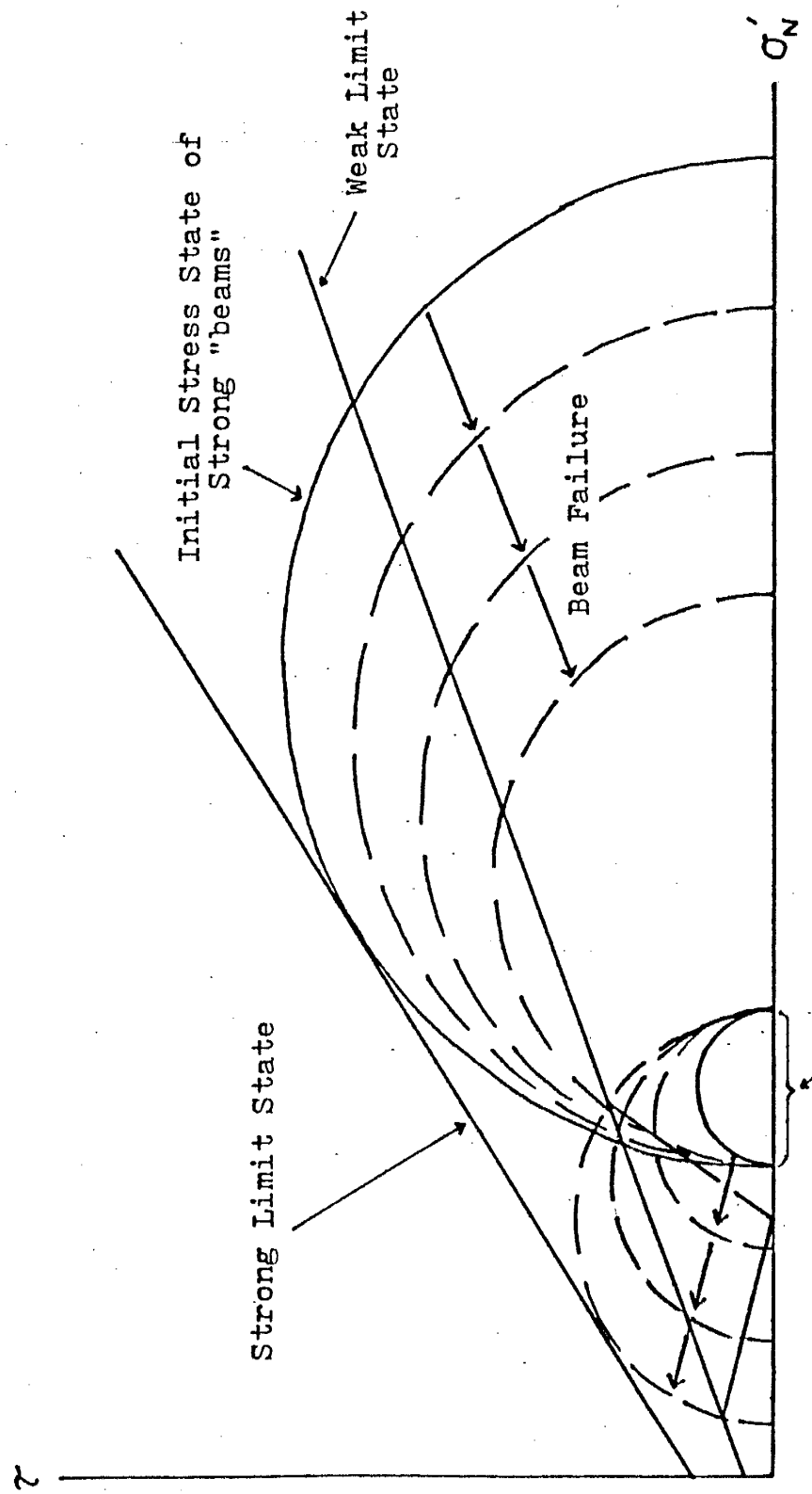

Figure 29. Transfer of stress from competent "beams" to adjacent incompetent lithologies due to the formation of a contractional fold/fault near the toe of the allochthonous sheet.

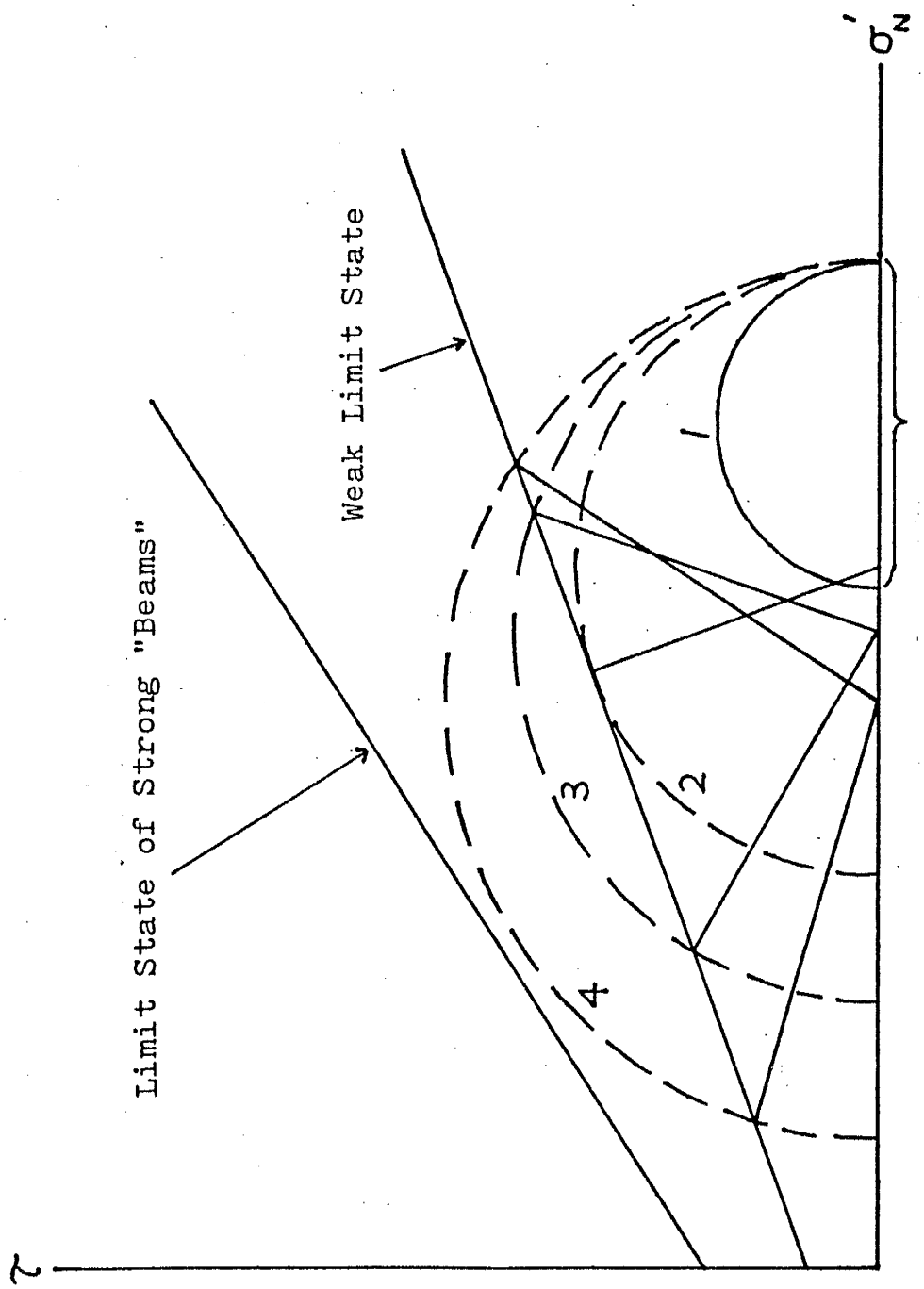

Figure 30. Sequential development of slip surfaces in the incompetent layer due to stress transfer accompanying failure of the adjacent competent member.

the state of stress in these lithologies continues to grow in response to the decrease in σ'_H. Eventually the circle will contact the limit state (circle 2) and fractures will begin to form in the material at some characteristic angle (in this case $\approx 35°$). With continued stress transfer, the diameter of the stress circle will grow larger still (circles 3 and 4), and fractures will be initiated over a wider range of angles. Evidence to support this deformational scenario is seen in the veins of recrystallized gypsum found in several regions of the field area. At these locations, a temporal evolution of fracture development is apparent; the initial fractures (35° dip) are cut by later-formed fractures of either higher ($40 - 60°$), or lower dip ($30 - 10°$).

Figure 31 shows an example of the vein networks that have developed in the weak Torres sands and gypsiferous sediments. Analyses of the fiber growth orientations recorded from numerous veins in the areas immediately surrounding the allochthons on Plates 1 and 2 are presented in Figures 32 and 33. This information was recorded from gypsum veins having a wide variety of attitudes and orientations. Upon inspection, several features of the deformation become apparent: (1) there is strong tendency for the data points to cluster close to the primitive circle, and (2) there is a notable absence of data in the centers of these figures. Remembering that these data points represent the down-plunge directions of gypsum fibers which have formed in compressional fractures, their orientations provide information concerning the movement of the translating allochthons and the mechanical response of the sediments being overridden.

The clustering of data points at shallow plunge angles (close to the primitive) indicates that crystal growth records lateral expansion of the underlying sediments to the load exerted on them by the superincumbent allochthons. This conclusion is supported by the essentially omnidirectional distribution seen in the Sierra de la Cruz-Rancho Grande Well data group (Figure 33). Data collected from the Mesa del Yeso-Gibbs Place trend (Figure 32) does not display this feature as well due to alluvial cover which compromised the collection of data in specific areas. Within each of these clusters, point concentration tends to be highest at plunge angles between

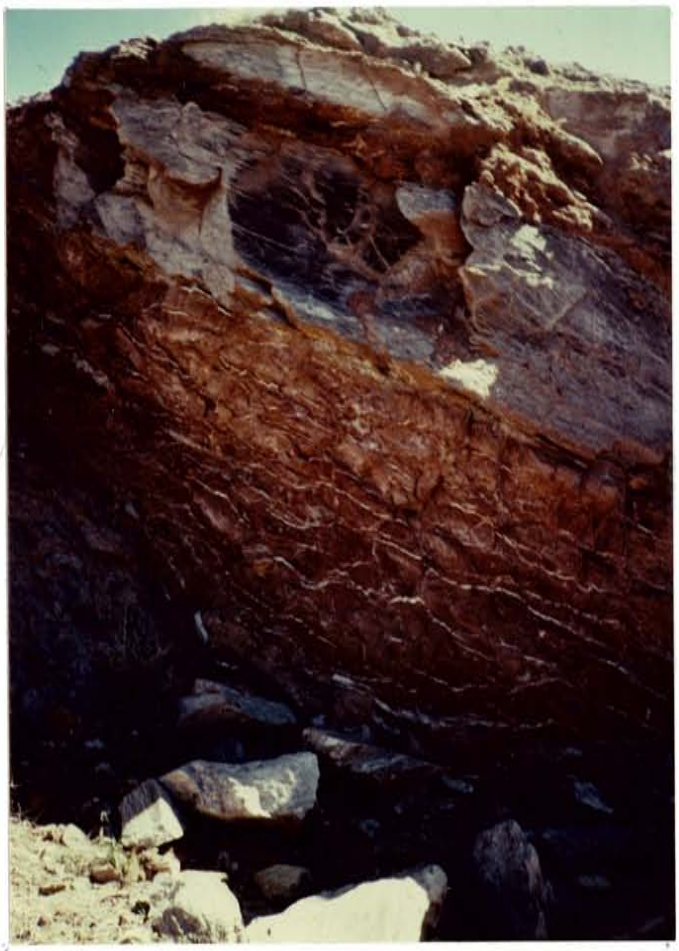

Figure 31. Example of the network of veins comprised of fibrous gypsum crystals which have formed in the weak Torres sandstones. Height of exposure is approximately 10 meters. Upper one-third of outcrop is composed of massive layer of recrystallized gypsum.

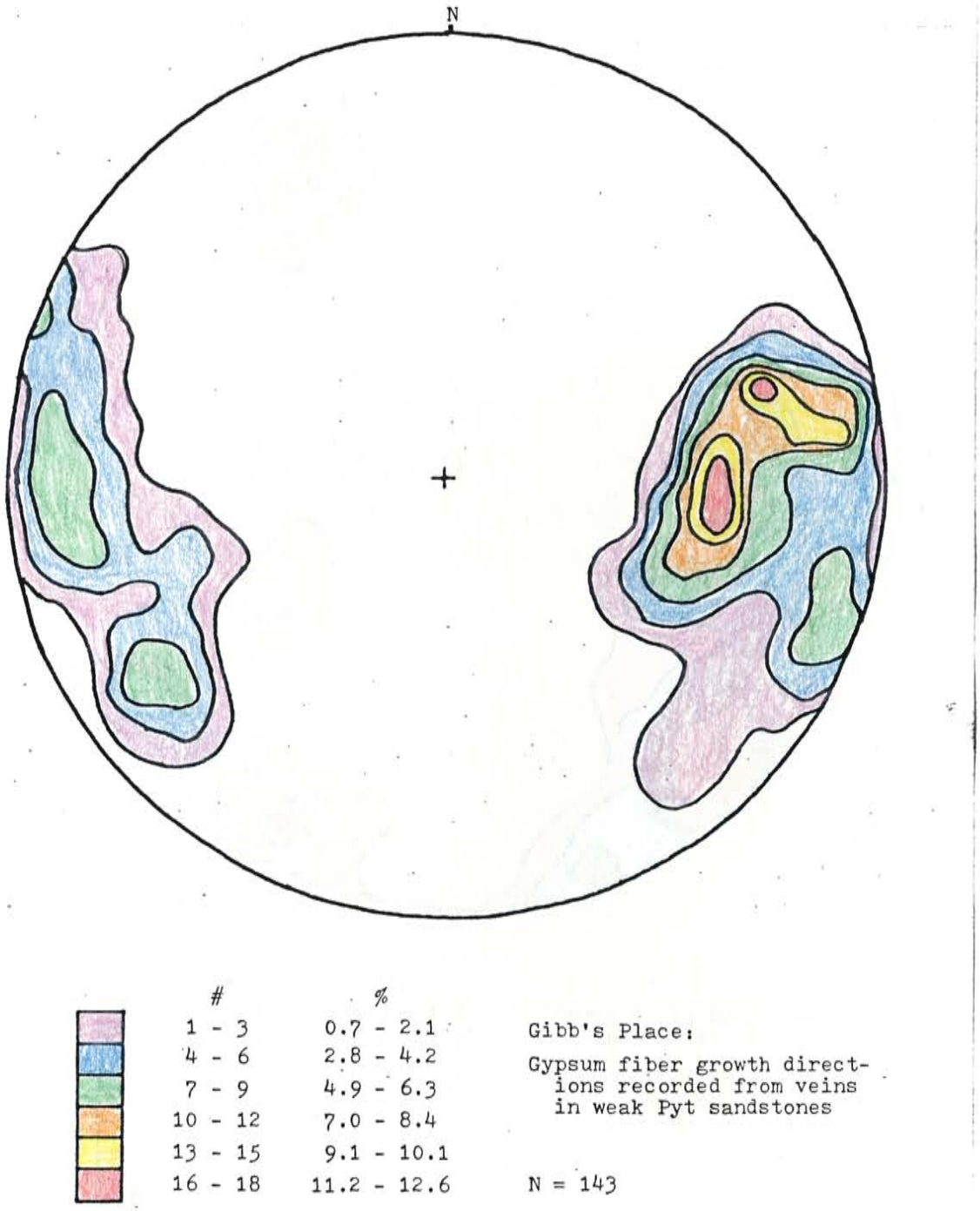

Figure 32. Contoured stereonet plot (Schnidt net; lower hemisphere projection) of gypsum fiber growth directions recorded from veins in weak Pyt sandstones (Mesa del Yeso–Gibbs Place).

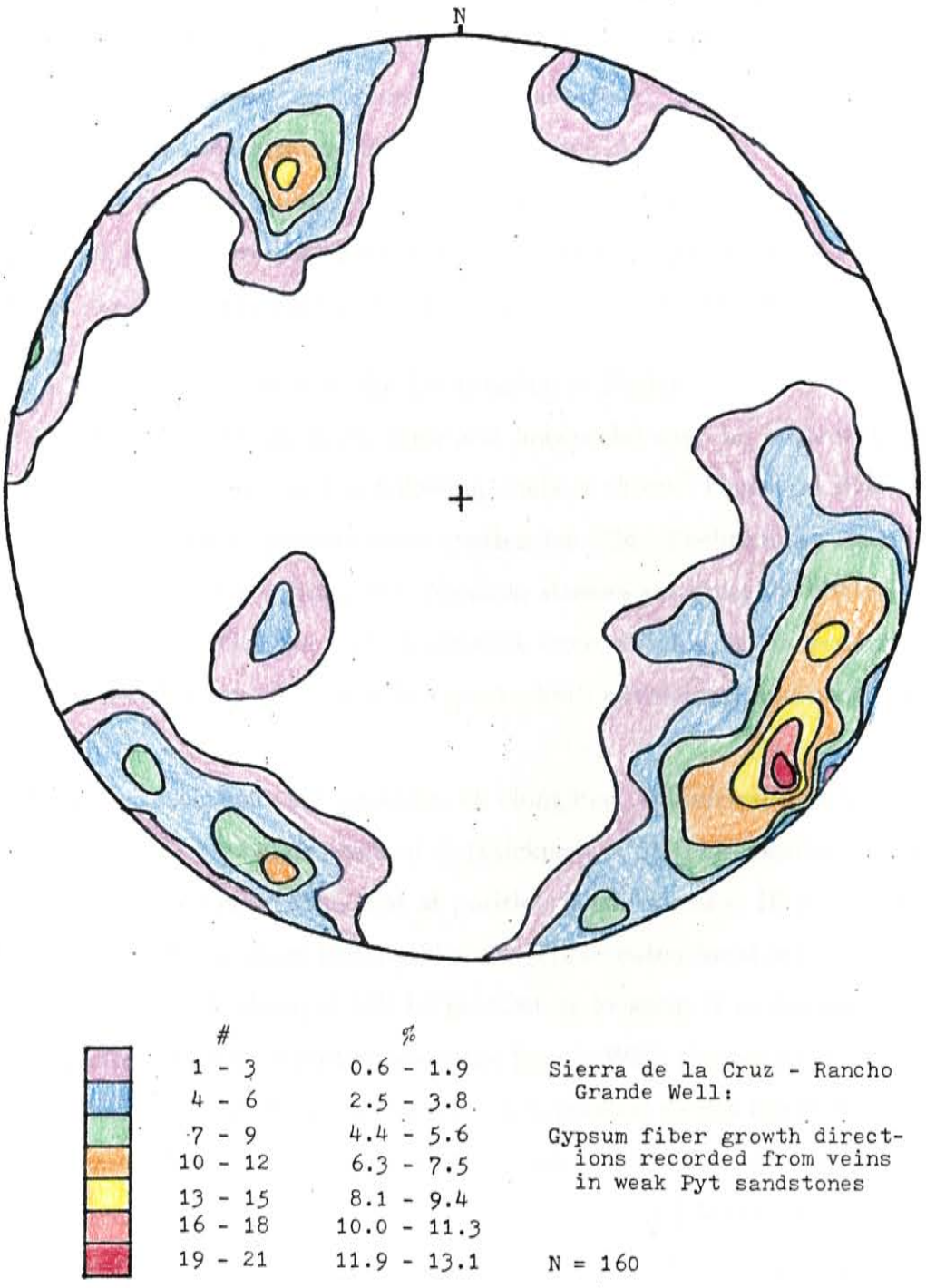

Figure 33. Contoured stereonet plot (Schmidt net; lower hemisphere projection) of gypsum fiber growth directions recorded from veins in weak Pyt sandstones (Sierra de la Cruz–Rancho Grande Well).

15 – 30° with a generally east-west or southeast-northwest directional preference. This fiber-growth orientation concentration, which was recorded from fractures displaying a wide range of dips, suggests that development was strongly influenced by the motion of allochtons along a subhorizontal detachment surface in a E-W or SE-NW direction. The lack of any fiber orientation data in the center of these stereoonet plots is an indication that high-angle fiber growth was prohibited, confirming that there was little, if any, vertical displacement of individual blocks in the fracturing process.

Effect of Allochthon Geometry on the Localization of Faults

The localization of faults (both high and low-angle) may be controlled by the geometry of the sheet itself, as the following analysis shows. Figure 34 illustrates a situation in which brittle, homogeneous overburden (the allochthonous sheet) rests horizontally upon a ductile substratum. No shear stresses act along the brittle/ductile interface, so consequently, the total horizontal force which acts on vertical cross-sections must be the same. This will be true for both extensional and compressional forces.

Consider an allochthon that possesses an elongated, cylindrical depression in its upper surface, as shown below position A (thickness = I). This location presents a smaller vertical cross-section than that at position B (thickness = II) outside the depressed region. So, if a uniform horizontal stress (either extensional or compressional) is applied to this brittle sheet, it will be greatest at location A as demonstrated by the force balance equation provided below the figure. With respect to the stress due to vertical loading, it is obvious that for a given horizontal datum the stress at B will always be greater than the stress at similar horizons within the depression.

This situation can therefore be represented by the solid Mohr circles which are shown in Figure 34B, where the H and V subscripts refer to the horizontal and vertical stresses at the positions indicated. If this original state of stress is altered by imposing horizontal extension on the brittle overburden, some surprising results are obtained with respect to fault formation and location. Assuming that extension occurs at a rate slow enough to allow the ductile substratum to adjust to this load change, any

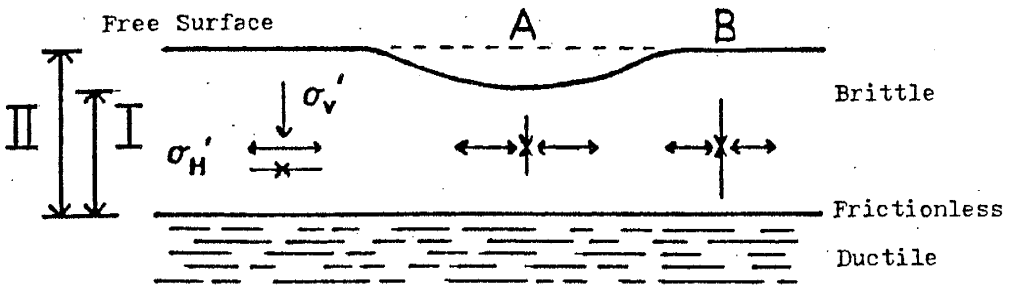

$$\sigma'_{HB} \cdot II = \sigma'_{HA} \cdot I$$

$$\sigma'_{HA} = \frac{II}{I}\,\sigma'_{HB}$$

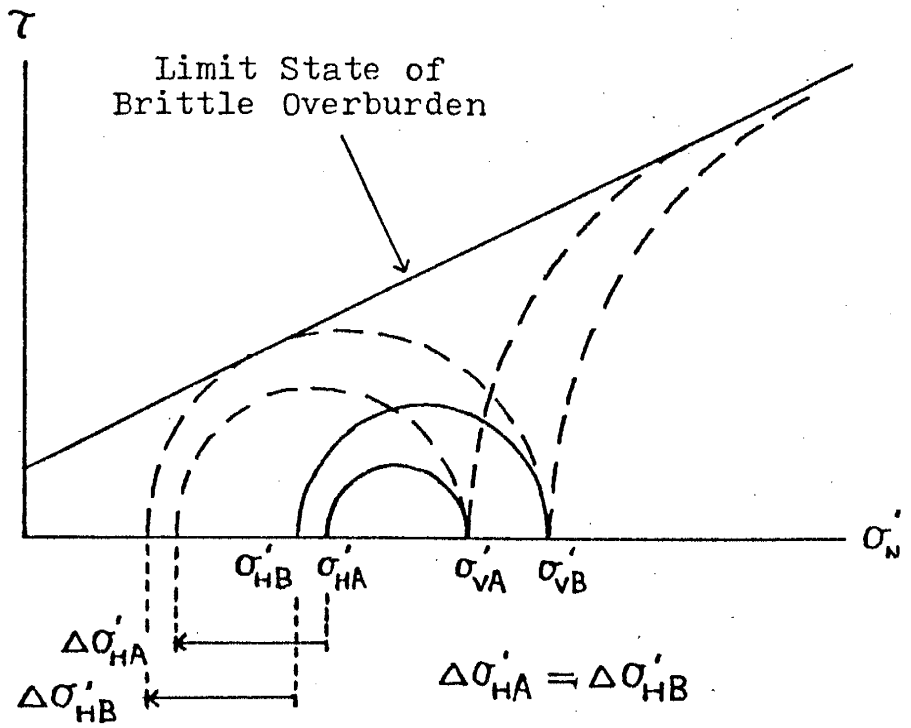

Figure 34. The effects of allochthon geometry on the localization of faults. Brittle overburden with cylindrical depression subject to either horizontal extension or compression.

shear stresses which might be induced along this interface can be neglected. Applying equal horizontal extension to both original stress states, ($\triangle\sigma'_{HA} = \triangle\sigma'_{HB}$), causes the B Mohr circle to encounter the limit state and induce active normal faulting, while the A stress state remains subcritical. This result is counterintuitive; the first faults will form outside the depressed region, in the thicker portions of the sheet! Conversely, imposed horizontal compression induces passive limit failure and associated thrusting within the depressed area, as is shown by the large, dashed Mohr circles. This result is not so surprising.

Formation of Secondary Normal Faults

In principal, the state of stress of the overriding allochthon may remain subcritical as the sheet glides along the detachment layer. Various experimental techniques have shown that differential stresses in sedimentary rocks that have become detached and travelled some distance over evaporites are consistently less than cases where travel has taken place over rocks offering more frictional resistance (McGarr, 1980; Engelder and Geiser, 1984). This possibility was examined during consideration of how sheet geometry affects fault localization and it was shown that only modest stress changes are required to bring the "detached" stress circle into contact with the limit state, thus producing secondary normal fault structures.

As noted in the field and on page 23, little deformation is present in large parts of the sheet; these regions indicate subcritical states of stress as shown in Figure 35. In this figure, Mohr circle 1 represents the subcritical stress state of the overridding allochthon, and Mohr circle 2 pertains to the substratum. In order to facilitate gliding, the stresses in the weak, overpressured substratum must be in the limit state, and accordingly stress circle 2 touches the limit line for this material. Any local steepening of the basal slip plane, or change in the effective basal friction, will produce a reduction in base-parallel normal stress in the gravitationally driven sheet. Such a reduction can induce local normal faulting as illustrated by stress circle 3. Also shown in Figure 35 are the orientations of possible conjugate fault systems as determined by the pole-method. Of particular note is the fact that these faults are

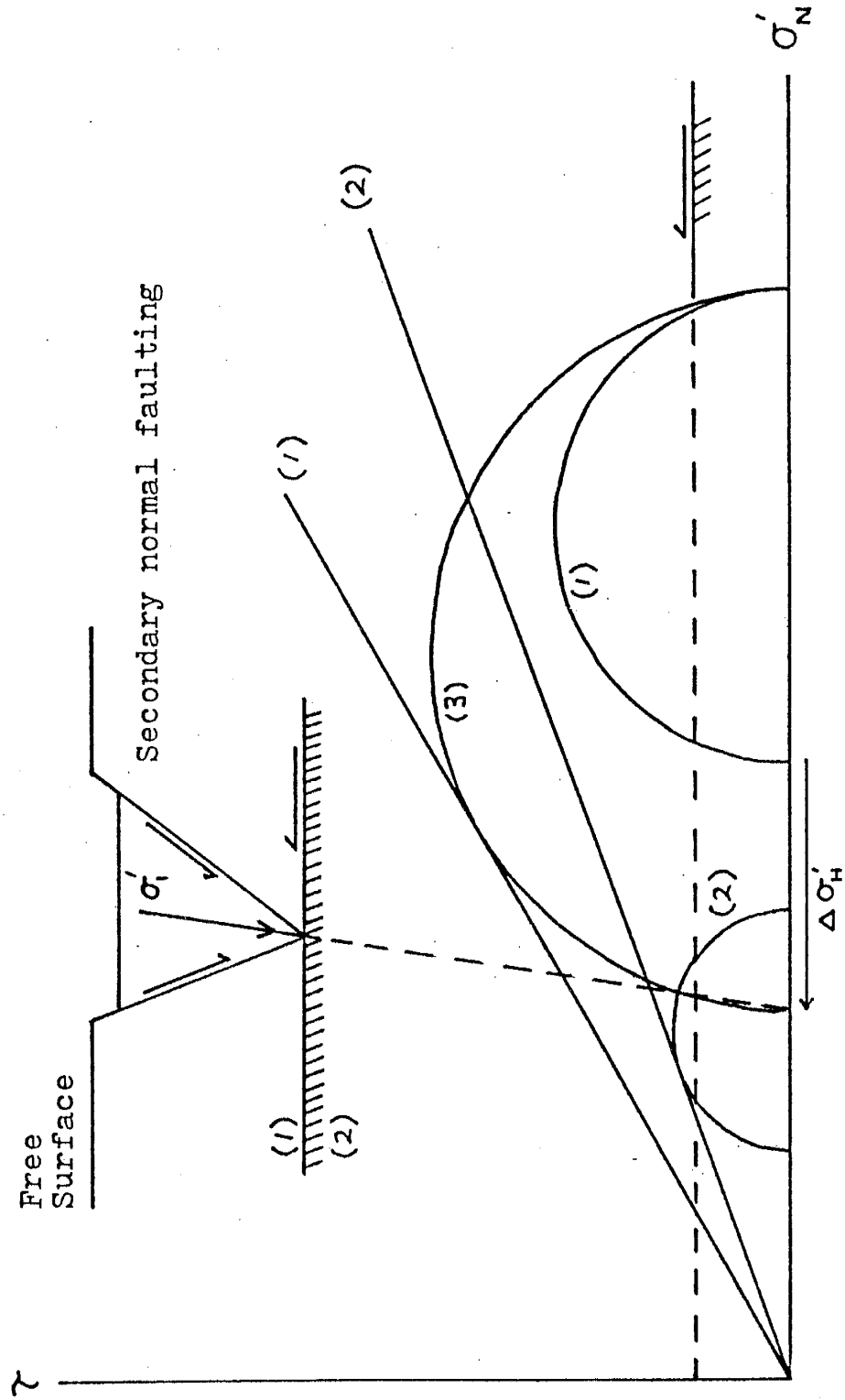

Figure 35. Stress differences across a stratigraphic interface subject to variation in fluid pressure and the formation of secondary normal faults in a gravitationally gliding rock sheet on a lubricating (overpressured) substratum.

asymmetrically disposed with respect to the vertical. Faulting of this type, with minor throws, takes place contemporaneously with the gravitational gliding of the allochthon sheet. A passive limit state may exist in the overridden incompetent strata simultaneously with a subcritical (elastic), or even with an active limit state in the competent allochthon. The substratum is subject to either brittle or ductile deformation depending upon the local lithology.

Strain Partitioning in Emplacement Process

Another feature that is observed in the vicinity of the allochthons is the strong tendency for limestones of the Torres Member to dip toward the overriding rocks (see allochthons on Plate 2 for good examples). Dip angles of these beds range from a few degrees to near vertical and virtually any strike direction is possible. Despite variations in the geometry and attitude of the rocks comprising the allochthons themselves, this relationship is consistently observed. To what can such phenomena be attributed? The answer may lie, once again, with the rheological properties associated with the Pyt/Pyc gypsums. It has already been shown that gypsum behaves rheologically as a Maxwell fluid. Stated simply, if subject to stress levels in excess of its minimum yield stress, such a material will flow via creep processes toward less restrictive, low-stress areas (Reiner, 1949). Consider a situation where interbedded evaporites and carbonates underlying a portion of the allochthonous sheet are unconfined in the lateral direction, perhaps due to tectonic faulting and/or erosional effects. Stresses introduced by the weight of overburden will then cause the gypsum to flow to regions of lower stress. In the process, the carbonates which crop out near the borders of the allochthon will be subject to folding as this viscous vertical thinning and lateral expansion occurs. This results in limestones beds which dip in the direction of the overriding rocks. Even a small allochthon is capable of exerting sufficient vertical stress to induce the lateral expansion of the underlying evaporites. The limestones become passively deformed due to pure shear of the gypsum in response to the gravitationally imposed load.

Because of the strong contrast in rheological properties exhibited by the rocks

involved in the deformation, no single mechanism can explain all the structural features we observe. In 1970, Kehle proposed a model of viscous gliding of the whole sheet (nappe) on a low viscosity basal substratum, essentially deforming due to simple shear only, and ignoring gravitational influences in the rocks themselves. In contrast, models of emplacement emphasizing gravitational collapse of nappes under their own weight advanced by Ramberg (1981) are based on the process of pure shear. More recently, investigations by Merle (1986) and Brun and Merle (1988) have shown that these approaches are either too simplistic or unrealistic to accurately describe conditions in sheet emplacement. Their models call for provisions to be made for the partitioning of strain throughout these sheets, which they refer to as spreading-gliding nappes.

An inspection of the kinematic indicators found in the allochthon sheet demonstrates that the mode of deformation is dependent on rock type and location. Starting at the upper surface of the overriding sheet of competent rocks, the deformational mode is that of brittle extension. Proceeding to the base of the translating sheet, deformation may be classified as brittle simple shear in those regions where competent rocks are involved. Where the upper sheet overlies gypsum, little shear is evident in the competent rocks. The gypsum itself exhibits the most complex behavior, a combination of vertical collapse and horizontal spreading – pure shear. In addition, ductile simple shear is observed within the gypsum where bordered by unsheared, competent rocks, an example of kinematic and mechanical discontinuity at a coherent interface (Cobbold, 1983). Thus, the observed strain is thought to be the result of a process where viscous gliding and viscous spreading have occurred together (Merle, 1986). When considered along the direction of flow, pure shear dominates motions up-hill and over obstructions, and the simple shear component dominates in down-hill motion.

CHAPTER V – STRUCTURAL INTERPRETATION AND GEOLOGIC HISTORY

In some areas unambiguous interpretations are difficult to make because several structural features share a common orientation. Many of the remnants of the dis-

sected allochthon sheet exhibit general outcrop trends (either singly or in groups) of approximately N30E. This orientation is also noted for the strike of many of the major Tertiary normal faults which cut the allochthons and the reverse faulting associated with the Montosa fault zone. In addition, a majority of the anticlines, synclines, and monoclines developed in the area, and virtually all the intrusive igneous dikes, share this directional preference (see Plates 1 and 2). Add the effects of erosion and alluvial cover, and decisions as to the structural significance or temporal evolution of a particular outcrop can become problematic. Some structural interpretations, therefore, rely more heavily on overall familiarity with the region developed through months of field work.

Evidence for Multiple Points of Origin and/or Multiple Periods of Emplacement

It is probable that there was either more than one location of origin for the allochthons, or that detachment and translation occurred at different times at various locations. Evidence of this can be found on Plate 1 near the northwestern part of Mesa del Yeso. Here an allochthon contact that separates Torres and San Andres lithologies has been folded by forces associated with the translation of a later-arriving allochthonous sheet.

Additional support for this conclusion comes from various types of deformational and lithologic observations. The portions of the lower allochthon complex which lie immediately in front of the upper sheet have numerous well-developed overturned folds which show a consistent northwesterly vergence. This implies a translation direction from the southeast for the upper sheet. Also, there are marked differences in the lithologies of which the two sheets are composed. In the area presently under consideration, the lower sheet is composed of Torres and San Andres sediments, while the overriding sheet contains Cañas, Joyita, Glorieta, and San Andres. Comparison of the San Andres sediments of these two allochthon sheets indicates a profound facies change between the sites of deposition. The lower sheet is characterized by massive gypsum deposits which are separated by occasional medium-to-thick bedded dolomites and limestones. In most areas, the evaporites comprise greater than 80%

of the formation. This composition contrasts strongly with that of the upper sheet where thick limestones and dolomites dominate, and no evaporites are present. Such drastic compositional differences offer strong support for different points of origin for these two detached sheets.

Tertiary Normal Faulting and Gravel Pediments

Along some of the N30E trending faults large amounts of uplift have occured which places the middle portion of the Abo in lateral contact with middle Chinle. This represents vertical movement on the order of two-thirds of a kilometer, comparable with that inferred for the Montosa fault (Colpitts, 1986).

Several locations provide evidence of repeated vertical movement on these faults. Successive stratigraphic horizons of well-cemented, imbricated gravels, primarily composed of Permian rocks (Pyt, Pym, Pg, and Psa) are found in the vicinity of some NW trending faults. The individual clasts show little evidence of rounding due to transport processes and imbrication indicates a east-to-west flow direction during deposition. Conspicuously absent are any clasts of granitic or metamorphic composition, and characteristic red coloration which would suggest these deposits may in fact be Baca, and so these rocks are considered to be late Tertiary. The overall attitude of these gravels also suggests that they are of fairly recent derivation. Deposits at several widely separated locations on Plate 1 are found at virtually the same elevation (± 20 feet) and show very little relief despite large vertical offset in the rocks they overlie. This gravel layer exhibits a shallow, westerly dip, and is locally well-indurated with calcite cement. If indeed these deposits are older (early or mid-Tertiary in age), one would not expect to see such undeformed remnants of this surface with all the normal faulting associated with the opening of the rift.

Hydrologic Nature of Basal Faults

The surface which separates the allochthons of the upper sheet from the underlying Triassic sediments also serves as the locus for a number of perennial springs on the Sevilleta Wildlife Refuge. Apparently, meteoric water which has percolated down through the upper layers is stopped as it encounters the mudstones of the Chinle.

Areas of large trees (tamarisk, oak, and juniper) and lush vegetation (various shrubs, grasses, and in certain areas, cattails) mark the location of these springs. Such springs are also noted in areas where Abo mudstones are close to the basal allochthon contact, usually where Tertiary normal faulting has disturbed this surface. It is probable that this "aquitard" made up of these mudrocks aided in the emplacement process by reducing the effective normal stress along the basal surface of the allochthons.

One may inquire as to why we do not see these detachment surfaces developed in the Triassic mudstones, for are they not inherently weak and equally prone to produce such features? Recent studies by Jordan and Nüesch (1989) present experimentally derived evidence to the contrary. In particular, at the depths of burial with which we are concerned (from $\approx$ 0.6–1.0 km for the Triassic sediments), their findings clearly indicate (Figure 36) that gypsum is far weaker, more ductile, and much more likely to develop surfaces of décollement than mudstones. As illustrated in the figure, at a depth of one kilometer, saturated clay requires about 75.0 MPa differential stress in order to undergo failure, compared to approximately 10.0 MPa for gypsum. Maximum stress values for a vertically oriented σ_1 due to one kilometer of overburden are about 25.0 MPa, and the differential stress would be only about two-thirds of this value. Clearly, such conditions are insufficient to produce décollement structures in the overlying Triassic mudstones, where stress conditions would be even more restictive than in the underlying Permian gypsums. Notice, however, that when burial depths exceed two kilometers, an inversion of the relative strengths of anhydrite and clay is observed.

Geophysical Support for Structural Interpretations

Structural interpretations concerned with whether there is an increase in the thickness of the stratigraphic section due to bedding plane faults cannot be unambiguously determined from field exposures at several crucial areas. This is primarily due to thick accumulations of alluvium at these locations. One area in particular is that of the western slope of the topographic high that runs from the northern boundary of the map area down through Mesa del Yeso (see Plate 1); here several

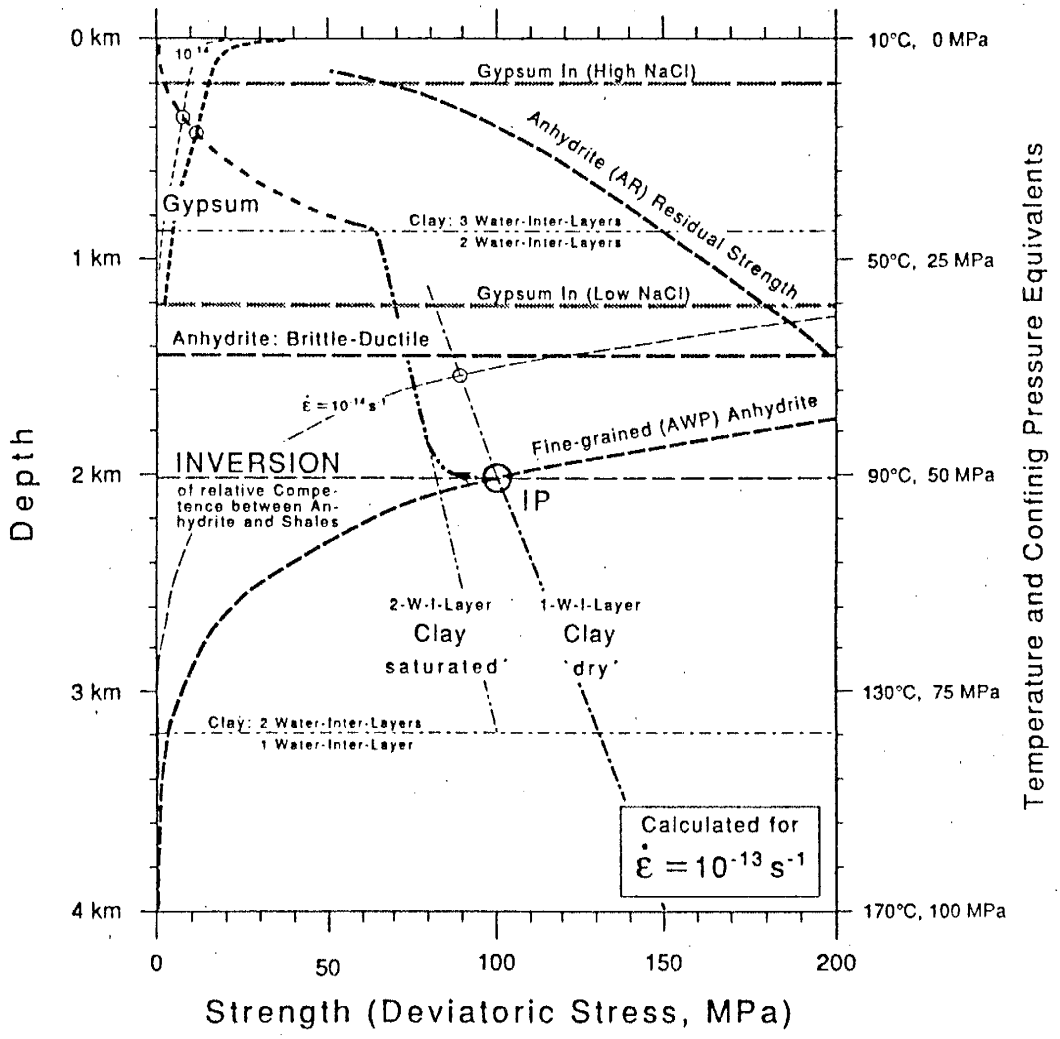

Figure 36. Compilation of mechanical data of shales, anhydrite, and gypsum, for the ambient conditions of Jura overthrusting (from Jordan and Nüesch, 1989).

interpretations are possible. The succession appears stratigraphically correct as one approaches the ridge from the west; going down-section, rocks of the Triassic Chinle are followed by Permian limestones and gypsum of the San Andres Formation. In contrast, if this area is approached from the east, going up-section, it it obvious that the Permian strata are allochthonous – the Joyita, Cañas, and upper part of the Torres Member of the Yeso Formation are missing between the fault contact separating Glorieta and middle Torres. Because of the aforementioned alluviation along its western side, no unequivocal structural interpretation is possible. This is unfortunate, for the implications of these competing interpretations call for deformational scenarios of very different scales. The problem basically boils down to the question, is the location to be interpreted as a Tertiary monoclinal flexure, or are the Triassic and Cretaceous rocks allochthonous?

Within the mapped area, there are a few sources of subsurface data which can illuminate the structural picture. Socorro Line 2A of the COCORP (Consortium for Continental Reflection Profiling) seismic reflection survey of the Rio Grande rift (Brown and others, 1979) does cross over into the northernmost portion of the study area for a short distance. Line 2A runs approximately parallel to the structural trend of the rift for 33 kilometers, but only the southernmost several kilometers cover the area studied, essentially from VP 200–250. The COCORP studies are intended to elucidate the deep structure of the continental crust, and consequently wavelength selection and data processing methods somewhat compromise the shallow (1.0–1.5 km) structural information we seek. Fortunately, studies by Brocher (1981) which were designed to investigate the velocity structure of the uppermost 1.2 kilometer along Line 2A do contain information useful in this analysis.

If indeed these Mesozoic sediments are not autochthonous, but the upper layers of an allochthonous sheet, we should see some evidence of this crustal thickening on the seismic record. In particular, pronounced offset should be seen at the level of the strong reflection identified with the midcrustal magma body. Repetition of the stratigraphic interval from mid-Torres through mid-Mancos (minus the Cañas–

Joyita interval) would increase the sedimentary cover overlying the Precambrian by approximately 600 meters. Thickness of the normal section is 1400 meters, so the normal section plus that repeated due to allochthonous cover would be 2.0 kilometers. Assuming an average compressional velocity of 4.20 km/sec for the mid-Torres through mid-Mancos sediments (Brocher, 1981), the total two-way travel time differential one would expect to observe in the normal and thickened sections is equal to 0.30 seconds. An inspection of the seismic section (Brown and others, 1979) does not show any such offset of the reflection correlated with the upper surface of the Socorro magma body. The conclusion is reached that sediments west of the region of the monoclinal flexure cannot be regarded as being allochthonous, but instead must be considered as autochthonous. The cross-section has therefore been constructed with this interpretation in mind.

Because our problem is concerned with the uppermost portion of the crust, gravity measurements made in the region (Sanford, 1968; Keller, 1983) offer even less assistance in answering our structural questions, and will not be considered further. Unambiguous structural interpretation of the deformational features in the region will only be possible after areas have been completely mapped and additional subsurface information (seismic, cores, well logs, etc.) is available to help complete the geologic picture.

Estimate of Transport Distances

An important question raised by the structural interpretation shown in cross-section $A - A'$ (Plate 3) needs to be addressed. In the easternmost portion of the section, Pyt and Pym overlie the Chinle Formation. The question is, how far to the east do the Triassic sediments extend beneath the Permian lithologies? A similar situation is noted on sections $E - E'$ and $F - F'$ from Colpitts (1986) for the adjacent region directly south of the area mapped in Plate 1. One approach to this problem is to consider the exposures of uplifted rocks in the vicinity of the Montosa fault. Here sediments as old as the Pennsylvanian are exposed, but nowhere is there any indication of the Triassic, which would be expected, if indeed, the Chinle continued to extend

eastward beneath the Permian sediments. Also, there are no surface exposures of Triassic rocks to be found anywhere between the fensters shown on cross-section $A-A'$ and the Montosa fault, with distances ranging from about four to eight kilometers. This suggests that somewhere in the subsurface within this interval, the "toe" of the gravitationally detached sheet must ride up over the autochthonous Mesozoic sediments. Such a geometry was proposed in Figure 15 (page 31) as part of a schematic sequence illustrating aspects of timing and deformation.

The present topography of the study area varies from a high of approximately 7100 feet at La Cebolla along the eastern margin to about 5100 feet near the southwest portion of Mesa del Yeso. This general geometry is conducive to the emplacement of the thrust sheets from east to west; an eastern high having served as a source of gravitational potential energy which caused a westward translation of the sheet (see Figure 15). Allochthon displacement can be estimated by measuring the distance from the easternmost exposure of the underlying Triassic sediments to the westernmost edge of the overriding allochthons. Results of such procedures yield transport estimates of from 4.0 to 6.0 kilometers.

The total displacement of the thrust sheet will not have taken place in one continuous process. With the initiation of the first movement of the toe, folds and fractures will form, the fluid pressure will decrease, and the Mohr circle will shrink, temporarilly inhibiting motion until additional increments of stress are applied. Also, there are topographic effects to consider, for most probably the geometry of the detachment surface will not have been entirely planar, but would have possessed obstructions or protrusions which would impede progress. The advance of the sheet might resemble motion similar to the crawl of a caterpillar, with only segments of the sheet moving at a given time. Thus, the process of rapid load transfer from beams to incompetent layers may be repeatedly required throughout the lifespan of movement on this surface. The overall movement could be imperceptibly slow, consisting of a series of discontinuous, rapid spurts. Emplacement of such a sheet is a process that conceivably takes place on the order of tens of thousands to perhaps millions of years.

Local and Regional Geologic History

The following explanation is proposed to account for the various types of structural and stratigraphic features displayed in the study area. Whenever possible, dates are supplied to better correlate these events.

The sedimentary deposits of the Pennsylvanian through Cretaceous periods were deposited under alternating marine and continental conditions. They are composed of various types of lithologies (limestones, dolomites, shales, sandstones, siltstones, mudstones, and evaporites) which record the repeated advance and retreat of shallow inland seas in central New Mexico (see Figure 2 and Plates 1 and 2). These sediments were deposited on an erosional surface made up of metamorphosed supracrustal and igneous rocks of Precambrian age. Conditions in the Permian are of particular concern because at that time the lithologies of the Yeso Formation (Leonardian) were formed. Due to climatic conditions and recurrent tectonics, the depositional environment vacillated between situations which favored carbonate, sands, and evaporite formation. The resultant sequence of interbedded limestone, sandstone, and gypsum beds was to have a profound effect on the structural stability of the rocks in the region. Sedimentation continued throughout the Mesozoic, with the exception of a period of uplift during the Jurassic.

Deformation attributed to the Laramide Orogeny (late Cretaceous to middle Eocene) constitutes the next major structural event to affect the region. Compressional forces related to high rates of convergence between the Farallon and North American Plates (late Cretaceous) and the opening of the Norwegian Sea (late Paleocene to early Eocene) are believed to have caused the widespread structural deformation attributed to the Laramide (Chapin and Cather, 1981). One such local result was the development of the Montosa Fault system in response to transpressional forces between the Colorado Plateau and the North American Craton. This structure is observed to cut upper Cretaceous rocks (Stark and Dapples, 1946), and so its formation is dated as being late Cretaceous to early Paleocene. As the Montosa Fault developed, the superincumbent strata was subject to extensional and shear

stresses developed in the adjacent sediments.

The stability of a geological structure is intimately dependent on the nature and arrangement of its constituent rocks. Given the situation present in the case of the Yeso lithologies (weak, ductile evaporites alternating with competent units), deformation of the sediment stack was inevitable. As more and more load was imposed on the critical members (primarily Torres limestones), their strengths were eventually exceeded, and folding and faulting of these rocks occurred. Concentration of stress near the front of the sheet caused the formation of a shallow ramp up which the Permian rocks moved. Powered by gravitationally induced shear stresses, emplacement of the allochthon sheet proceeded from southeast to northwest, overriding Mesozoic rocks in the process. Many deformational structures (folding, faulting, fracturing, etc.) were produced during the various stages of translation. Dissection of this once continuous sheet has now left only scattered remnants between which the underlying Triassic and Cretaceous sediments are now exposed.

Deposition of the Eocene Baca Formation occurred in response to uplifts developed along the axis of the modern Rio Grande rift (Chapin and Cather, 1981). The deformation attributed to allochthon translation appears to predate these deposits, for no evidence of their involvement in the deformation can be found anywhere within the study area. Volcanism commenced in the Socorro region at the start of the Oligocene and continued periodically into Miocene time. Extensional stresses associated with the opening of the Rio Grande rift in mid-Oligocene time ($\approx$ 29 MYBP) contributed to the development of the northeast trending faults and the emplacement of alkaline diabase dikes, some of which are observed to penetrate into the allochthons. Sediments composed mainly of sands and gravels (late Tertiary Santa Fe Formation) were produced due to erosion of uplifted regions and were spread out in broad aprons running from the rift shoulders to its main axis. Numerous tributaries of the Rio Grande, such as Arroyo de la Parida, have now dissected these alluvial surfaces somewhat.

SUMMARY and CONCLUSIONS

Allochthonous Permian rocks which overlie autochthonous Triassic and Cretaceous sediments are found at a number of locations along the east side of the Socorro constriction in the Rio Grande rift. The purpose of this investigation is three-fold: (1) to determine the direction(s) from which the allochthonous Permian rocks were emplaced, (2) establish the timing of this deformation, and (3) construct a mechanical model capable of explaining the observed deformational features. These questions have been addressed using an integrated approach combining detailed structural mapping, strain analysis of kinematic indicators, experimental rock-mechanics, and theoretical methods.

The portion of the sedimentary sequence in which the allochthons have developed consists of alternating layers of competent rocks (limestones and sandstones) separated by beds of incompetent material (gypsum and weak sandstones). Because of pronounced differences in the mechanical properties associated with these lithologies, such an arrangement and combination has proven to be crucial in the structural development of the allochthonous terranes. In particular, the gypsum possesses a variety of qualities, such as little or no porosity, water weakly held in its crystal lattice, fine grain size, and Maxwellian rheological behavior, that made it susceptible to strong deformation. Movement became concentrated in these weaker, more ductile layers and caused the superincumbent rocks to become mechanically isolated and allowed them to undergo a different strain history.

Numerous overturned or recumbent, horizontal to gently plunging folds are found in the middle to upper Torres Member of the Yeso Formation. They are most commonly developed where the Cañas and Joyita sections are absent between the basal fault and the underlying Torres. The orientation and west-to-northwesterly vergence of these folds records deformation produced by the generally ESE to WNW translation of the overriding allochthons. In addition to these folds, a wide variety of strain indicators were used to piece together various aspects of the structural picture. When considered collectively, these data provide a direct and succinct record of the

kinematic history of the rocks, and serve as a sound basis for the analysis of deformation. Important results derived from such procedures are: (1) that the nature of the deformation can be separated into two general catagories, brittle and ductile, based on lithologic characteristics and position within the allochthon complex, and (2) that when the various deformational features and their relative locations with respect to the basal contact of these allochthons are considered, a definite pattern to the nature and distribution of the strain ellipse emerges.

Based on field data, rock-mechanical testing, and Mohr circle analysis, several deformational scenarios were evaluated by modeling the development of the main structural features observed in the allochthons and the underlying lithologies. It was determined that gravitational gliding of a competent allochthonous sheet on a ductily deforming layer of evaporites best describes the field evidence and test results. Evidence collected from the field and the literature suggest that the source of these translating rocks were Laramide uplifts which lay to the east-southeast of the study area. Displacement of the allochthons is estimated at between 4.0 and 6.0 km. Structural, stratigraphic, and intrusional relationships observed in the field indicate that emplacement and deformation probably occured during the Paleocene Epoch.

APPENDIX A

The Maxwell Elasticoviscous Model:

This rheological model consists of viscous and elastic components, a dashpot and spring (often referred to as the Newtonian and Hookean elements), which are arranged in series (Figure A.1A). If we let σ_v and σ_e be the stresses acting on the two representative elements, and e_v and e_e be the strains produced in these elements we can express the stress-strain relations as follows:

$$\sigma_v = \mu \frac{de_v}{dt} \qquad \text{[A–1]}$$

and

$$\sigma_e = E e_e \qquad \text{[A–2]}$$

where μ and E are the viscous and elastic moduli, and the subscripts v and e refer to the viscous and elastic components, respectively.

Because the elements are in series, it follows that the total stress σ_T is equal to each of the individual stresses, and that the total strain e_T is given by the sum of the strain components,

$$\sigma_T = \sigma_v = \sigma_e \qquad \text{[A–3]}$$

$$e_T = e_v + e_e. \qquad \text{[A–4]}$$

Combining equations [A–1] and [A–3] we get

$$e_v = \frac{1}{\mu} \int_0^1 \sigma_T dt \qquad \text{[A–5]}$$

and substituting equations [A–2] and [A–5] into [A–4] yields the basic stress-strain relationships for the Maxwell elasticoviscous model

$$e_T = \frac{\sigma_T}{E} + \frac{1}{\mu} \int_0^1 \sigma_T (t)\, dt. \qquad \text{[A–6]}$$

In the case of constant applied stress, this expression becomes

$$e_T = \frac{\sigma_T}{E} + \frac{\sigma_T t}{\mu}. \qquad \text{[A–7]}$$

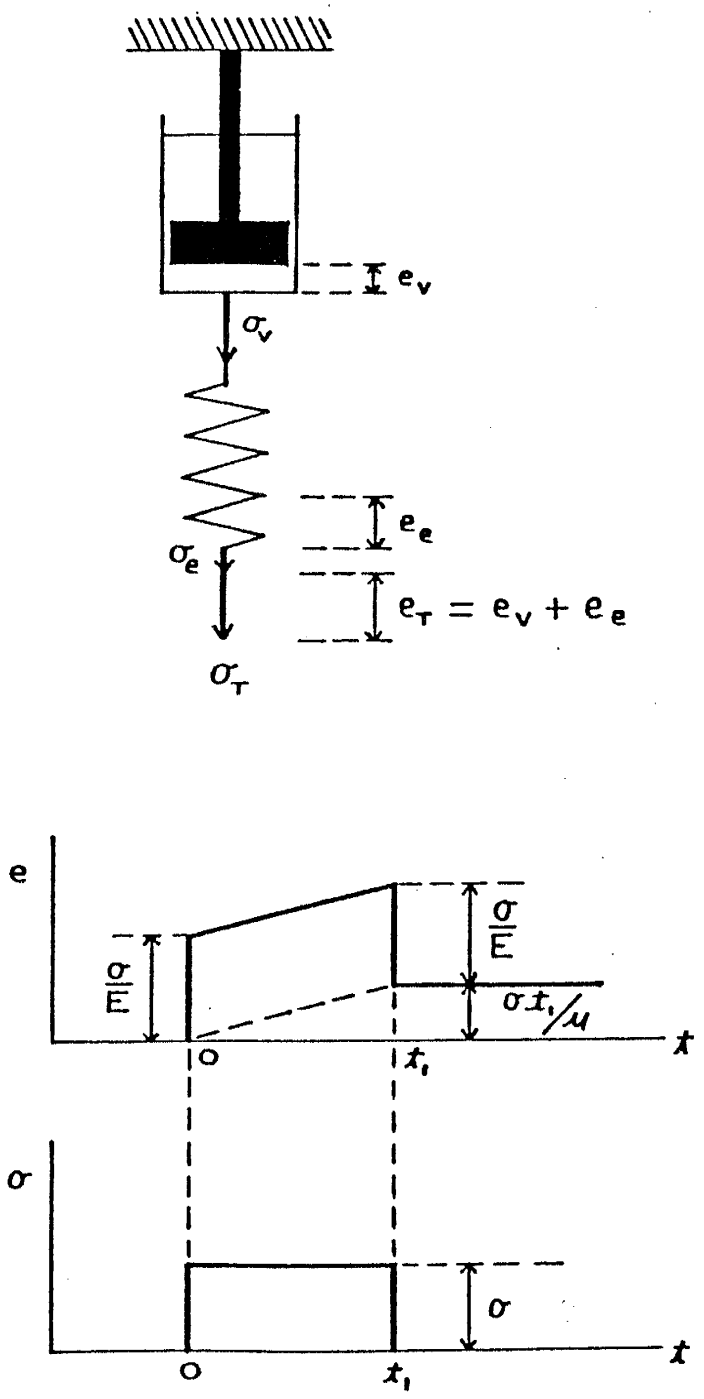

Figure A.1. (A) Rheological model of Maxwell elasticoviscous fluid. (B) Characteristic stress and strain graphs plotted as functions of time for a Maxwell substance.

This tells us that when the initial stress is applied, the material will show an instantaneous elastic strain equal to σ_T/E, followed by a viscous strain which is proportional to the duration of the applied stress. Upon removal of this stress at any time t, there will be complete recovery of the elastic strain, but a permanent strain of $\sigma_T t/\mu$ will be unrecoverable. Figure A.1B shows characteristic graphs of stress and strain for such a material plotted as functions of time.

The stress relaxation properties and the behavior of the stresses when strain of the material is held constant may also be determined from equation [A–7]. Setting $\sigma_T = \sigma$, and differentiating σ with respect to time we obtain

$$0 = \frac{1}{E}\frac{d\sigma}{dt} + \frac{\sigma}{\mu} \qquad \text{[A–8]}$$

or, rearranging this into a more revealing form,

$$\frac{d\sigma}{\sigma} = -\frac{E}{\mu}dt. \qquad \text{[A–9]}$$

Integrating both sides yields

$$\int_{\sigma_0}^{\sigma} \frac{d\sigma}{\sigma} = -\frac{E}{\mu}\int_0^t dt \qquad \text{[A–10]}$$

where σ_0 is the initial stress level at time t_0. This can be expressed in terms of logarithms as

$$\log_e \sigma - \log_e \sigma_0 = -\frac{E}{\mu}t \qquad \text{[A–11]}$$

and, finally, exponentiating gives us the expression we seek

$$\sigma = \sigma_0 e^{-(Et/\mu)}. \qquad \text{[A–12]}$$

This tells us that the stresses which were imposed on the body and produced deformation will relax exponentially with time. The rate at which this relaxation takes place is dependent on the viscous and elastic moduli. An elasticoviscous material is said to possess a characteristic relaxation time equal to μ/E, the period it takes for the original stresses to decay by $1/e \approx 1/2.7183 \approx 0.3679$ of their original value.

APPENDIX B

Experimental Data and Test Results of Rock-Mechanical Investigations:

Test Performed: Determination of Young's Modulus and Compressive Strength
Lithology Tested: Torres Limestone (Pyt)
Method Employed: Uniaxial Compression

Sample #	Length	Diameter	Length/Diameter*
1	2.61 in	0.98 in	2.66
2	2.66 in	0.98 in	2.71
3	2.52 in	0.98 in	2.57
4	2.71 in	0.98 in	2.77
5	2.60 in	0.98 in	2.65

*All values fall within stable range (2.25-3.00) as reported by Mogi (1966).

Summary of Test Results:

Young's Modulus, E	Compressional Strength, C_0
$E_1 = 38.04$ GPa†	$C_{01} = 104.00$ MPa†
$E_2 = 47.22$ GPa	$C_{02} = 98.50$ MPa
$E_3 = 41.21$ GPa	$C_{03} = 87.80$ MPa
$E_4 = 40.00$ GPa	$C_{04} = 106.00$ MPa
$E_5 = 50.94$ GPa	$C_{05} = 92.00$ MPa
$\overline{E} = 43.48$ GPa	$\overline{C}_0 = 97.66$ MPa
S = ± 5.40	S = ± 7.74

†GPa = 10^9 Pascals; MPa = 10^6 Pascals.

Samples generally unfractured, dense limestones; some contained fossils and small voids; all samples failed by sudden, explosive, brittle fracture.

Deformation monitored by an LVDT (linear voltage differential transformer) and a pressure-sensitive load cell displayed on a strip-chart recorder.

One inch chart displacement (load cell) = 1250 lbs applied load.

Conversion factor: 1 PSI = 6.895 x 10^3 Pa.

Tests conducted at termperature of $\approx 20°$ C; $\sigma_2 = \sigma_3 = 1$ atmosphere.

Test Performed: Uniaxial Compression
Lithology Tested: Torres Limestone (Pyt)

Data from Sample #1

Point #	Applied Stress, σ	Strain, e
1	5.00 MPa	0.018
2	11.50 MPa	0.024
3	16.50 MPa	0.030
4	24.10 MPa	0.033
5	41.50 MPa	0.036
6	62.00 MPa	0.043
7	74.00 MPa	0.045
8	92.80 MPa	0.050
9	104.00 MPa*	0.053*

*Conditions of failure; Applied stress = C_0

Young's Modulus, E, calculated by taking the slope of the straight-line portion of the stress-strain graph (from data points 3 to 9, inclusive); E = stress/strain = σ/e.

Data from Sample #2

Point #	Applied Stress, σ	Strain, e
1	4.00 MPa	0.021
2	10.00 MPa	0.025
3	13.00 MPa	0.031
4	33.30 MPa	0.035
5	47.00 MPa	0.038
6	55.00 MPa	0.040
7	71.50 MPa	0.042
8	98.50 MPa*	0.049*

*Conditions of failure: Applied stress = C_0

Young's Modulus, E, calculated by taking the slope of the straight-line portion of the stress-strain graph (from data points 3 to 8, inclusive); E = stress/strain = σ/e.

Data from Sample #3

Point #	Applied Stress, σ	Strain, e
1	4.50 MPa	0.017
2	9.50 MPa	0.022
3	18.00 MPa	0.025
4	25.50 MPa	0.026
5	36.00 MPa	0.029
6	46.00 MPa	0.031
7	63.50 MPa	0.035
8	75.80 MPa	0.038
9	87.80 MPa*	0.041*

*Conditions of failure; Applied stress = C_0

Young's Modulus, E, calculated by taking the slope of the straight-line portion of the stress-strain graph (from data points 3 to 9, inclusive); E = stress/strain = σ/e.

Data from Sample #4

Point #	Applied Stress, σ	Strain, e
1	5.00 MPa	0.032
2	10.00 MPa	0.036
3	14.00 MPa	0.042
4	31.00 MPa	0.045
5	44.50 MPa	0.050
6	50.50 MPa	0.052
7	59.00 MPa	0.053
8	76.50 MPa	0.058
9	90.50 MPa	0.061
10	106.00 MPa*	0.065*

*Conditions of failure; Applied stress = C_0

Young's Modulus, E, calculated by taking the slope of the straight-line portion of the stress-strain graph (from data points 3 to 9, inclusive); E = stress/strain = σ/e.

Data from Sample #5

Point #	Applied Stress, σ	Strain, e
1	3.00 MPa	0.026
2	7.80 MPa	0.039
3	10.50 MPa	0.041
4	23.70 MPa	0.044
5	38.00 MPa	0,047
6	66.00 MPa	0.051
7	72.50 MPa	0.053
8	84.00 MPa	0.055
9	92.00 MPa*	0.057*

*Conditions of failure; Applied stress = C_0

Young's Modulus, E, calculated by taking the slope of the straight-line portion of the stress-strain graph (from data points 3 to 9, inclusive); E = stress/strain = σ/e.

Test Performed: Determination of Young's Modulus and Compressive Strength
Lithology Tested: Cañas Gypsum (Pyc)
Method Employed: Uniaxial Compression

Sample #	Length	Diameter	Length/Diameter*
1	60.20 mm	25.80 mm	2.32
2	58.00 mm	25.80 mm	2.25
3	68.40 mm	25.70 mm	2.66
4	67.30 mm	25.80 mm	2.61

*All values fall within stable range (2.25-3.00) as reported by Mogi (1966).

Summary of Test Results:

Young's Modulus, E	Compressional Strength, C_0
$E_1 = 8.50$ GPa†	$C_01 = 30.30$ MPa†
$E_2 = 2.18$ GPa	$C_02 = 18.30$ MPa
$E_3 = 3.42$ GPa	$C_03 = 16.38$ MPa
$E_4 = 6.35$ GPa	$C_04 = 40.50$ MPa
$\overline{E} = 5.11$ GPa	$\overline{C}_0 = 26.37$ MPa
S = ± 2.86	S = ± 11.26

†GPa = 10^9 Pascals; MPa = 10^6 Pascals.

Samples generally dense, unfractured, gray-white, fine-grained gypsum; most samples show evidence of flow processes; all samples displayed strain-softening (onset of ductile behavior) in the later stages of loading – no sudden, brittle failure observed; several samples did not survive loading cycle long enough to yield sufficient data to determine E and C_0 (this information not included in data tables).

Deformation monitored by an LVDT (linear voltage differential transformer) and a pressure-sensitive load cell displayed on a strip-chart recorder.

One inch chart displacement (load cell) = 1250 lbs applied load.

Conversion factor: 1 PSI = 6.895 x 10^3 Pa.

Tests conducted at temperature of $\approx 20°$ C; $\sigma_2 = \sigma_3 = 1$ atmosphere.

Average strain suffered by samples before finally undergoing failure was 1.84% of their original length.

Test Performed: Uniaxial Compression
Lithology Tested: Cañas Gypsum (Pyc)

Data from Sample #1

Point #	Applied Stress, σ	Strain, e
1	2.14 MPa	0.0271
2	4.14 MPa	0.0379
3	4.90 MPa	0.0421
4	5.41 MPa	0.0445
5	6.96 MPa*	0.0552*
6	9.93 MPa**	0.0913**

*Onset of strain-softening and ductile behavior; stress-strain graph becomes curvilinear.

**Conditions of failure; Applied stress = C_0.

Young's Modulus, E, calculated by taking the slope of the straight-line portion of the stress-strain graph (from data points 1 to 5, inclusive); E = stress/strain = σ/e.

Data from Sample #2

Point #	Applied Stress, σ	Strain, e
1	1.36 MPa	0.0233
2	2.64 MPa	0.0247
3	3.70 MPa	0.0262
4	4.34 MPa	0.0271
5	5.11 MPa	0.0279
6	6.94 MPa*	0.0314*
7	7.32 MPa**	0.0351**

*Onset of strain-softening and ductile behavior; stress-atrain graph becomes curvilinear.

**Conditions of failure; Applied stress = C_0.

Young's Modulus, E, calculated by taking the slope of the straight-line portion of the stress-strain graph (from data points 1 to 5, inclusive); E = stress/strain = σ/e.

Data from Sample #3

Point #	Applied Stress, σ	Strain, e
1	0.43 MPa	0.00281
2	2.59 MPa	0.0159
3	3.23 MPa	0.0164
4	4.78 MPa*	0.0175*
5	6.55 MPa**	0.0194**

*Onset of strain-softening and ductile behsvior; stress-strain graph becomes curvilinear.

**Conditions of failure; Applied stress = C_0.

Young's Modulus, E, calculated by taking the slope of the straight-line portion of the stress-strain graph (from data points 1 to 5, inclusive); E = stress/strain = σ/e.

Data from Sample #4

Point #	Applied Stress, σ	Strain, e
1	2.68 MPa	0.0332
2	5.83 MPa	0.0459
3	8.51 MPa	0.0562
4	10.30 MPa	0.0622
5	12.20 MPa	0.0707
6	14.70 MPa*	0.0842*
7	16.20 MPa**	0.1010**

*Onset of strain-softening and ductile behavior; stress-strain graph becomes curvilinear.

**Conditions of failure; Applied stress = C_0.

Young's Modulus, E, calculated by taking the slope of the straight-line portion of the stress-strain graph (from data points 1 to 5, inclusive); E = stress/strain = σ/e.

Test Performed: Determination of Young's Modulus and Compressive Strength
Lithology Tested: Glorieta Sandstone (Pg)
Method Employed: Uniaxial Compression

Sample #	Length	Diameter	Length/Diameter*
1	62.70 mm	25.80 mm	2.43
5	66.10 mm	25.90 mm	2.55
9	68.10 mm	25.80 mm	2.64
12	67.30 mm	25.80 mm	2.61

*All values fall within stable range (2.25-3.00) as reported by Mogi (1966).

Summary of Test Results:

Young's Modulus, E	Compressional Strength, C_0
$E_1 = 1.49$ GPa†	$C_{01} = 30.10$ MPa†
$E_5 = 1.77$ GPa	$C_{05} = 36.00$ MPa
$E_9 = 3.78$ GPa	$C_{09} = 63.10$ MPa
$E_{12} = 3.90$ GPa	$C_{12} = 62.80$ MPa
$\overline{E} = 2.72$ GPa	$\overline{C}_0 = 48.00$ MPa
S = ± 1.30	S = ± 17.43

†GPa = 10^9 Pascals; MPa = 10^6 Pascals.

Samples generally unfractured, porous, well-sorted, fine-to-medium grained, quartz-arenites; samples show moderate induration with calcite cement; amount of cementation somewhat variable within a particular sample; some samples displayed strain-softening in the final stages of loading, but mode of failure was usually sudden, brittle fracture.

Deformation monitored by an LVDT (linear voltage differential transformer) and a pressure-sensitive load cell displayed on a strip-chart recorder.

One inch chart displacement (load cell) = 1250 lbs applied load.

Conversion factor: 1 PSI = 6.895 x 10^3 Pa.

Tests conducted at temperature of $\approx 20°$ C; $\sigma_2 = \sigma_3 = 1$ atmosphere.

Average strain suffered by samples before finally undergoing failure was 5.27% of their original length – this value is rather large and suggests significant porosity and patchy cementation are probably responsible.

Test Performed: Uniaxial Compression
Lithology Tested: Glorieta Sandstone (Pg)

Data from Sample #1

Point #	Applied Stress, σ	Strain, e
1	5.00 MPa	0.0123
2	5.96 MPa	0.0152
3	11.00 MPa	0.0188
4	15.00 MPa	0.0217
5	20.90 MPa	0.0253
6	27.20 MPa	0.0295
7	30.10 MPa*	0.0309*

*Conditions of failure; Applied stress = C_0.

Young's Modulus, E, calculated by taking the slope of the straight-line portion of the stress-strain graph (from data points 2 to 6, inclusive); E = stress/strain = σ/e.

Data from Sample #5

Point #	Applied Stress, σ	Strain, e
1	8.41 MPa	0.0472
2	19.20 MPa	0.0542
3	27.80 MPa	0.0584
4	34.60 MPa	0.0620
5	36.00 MPa*	0.0628*

*Conditions of failure; Applied stress = C_0.

Young's Modulus, E, calculated by taking the slope of the straight-line portion of the stress-strain graph (from data points 1 to 4, inclusive); E = stress/strain = σ/e.

Data from Sample #9

Point #	Applied Stress, σ	Strain, e
1	2.98 MPa	0.0232
2	7.66 MPa	0.0282
3	12.50 MPa	0.0321
4	15.40 MPa	0.0337
5	21.90 MPa	0.0368
6	27.50 MPa	0.0388
7	41.90 MPa	0.0428
8	59.60 MPa	0.0473
9	63.10 MPa*	0.0498*

*Conditions of failure; Applied stress = C_0.

Young's Modulus, E, calculated by taking the slope of the straight-line portion of the stress-strain graph (from data points 6 to 8, inclusive); E = stress/strain = σ/e.

Data from Sample #12

Point #	Applied Stress, σ	Strain, e
1	5.32 MPa	0.0473
2	12.60 MPa	0.0515
3	22.30 MPa	0.0549
4	28.60 MPa	0.0566
5	38.30 MPa	0.0591
6	55.80 MPa	0.0635
7	62.80 MPa*	0.0674*

*Conditions of failure; Applied stress = C_0.

Young's Modulus, E, calculated by taking the slope of the straight-line portion of the stress-strain graph (from data points 3 to 6, inclusive): E = stress/strain = σ/e.

Test Performed: Determination of Viscous Modulus and Stress-Relaxation Time
Lithology Tested: Cañas/Torres Gypsum (Pyc/Pyt)
Method Employed: Passive Gravitational "Constant-Force" Test (Rutter, 1972)

Summary of Test Results

Modulus of Viscosity, μ	Stress-Relaxation Time, r
$\mu = 4.36 \times 10^{17}$ Pa-sec*	$r = 8.54 \times 10^{7}$ sec $\approx$ 2.71 years

---

Test Performed: "Constant-Force" Test
Lithology Tested: Cañas/Torres Gypsum (Pyc/Pyt)

Point #	Time Elapsed	Strain Observed
1	10.00 sec	4.03×10^{-4}
2	30.00 sec	4.13×10^{-4}
3	5.00 min	4.22×10^{-4}
4	15.00 min	4.26×10^{-4}
5	1.00 hr	4.29×10^{-4}
6	2.20 hrs	4.31×10^{-4}
7	4.50 hrs	4.32×10^{-4}
8	1.08 days	4.32×10^{-4}
9	3.25 days	4.33×10^{-4}
10	7.55 days	4.35×10^{-4}
11	10.40 days	4.37×10^{-4}
12	20.25 days	4.41×10^{-4}
13	24.60 days	4.43×10^{-4}
14	31.15 days	4.46×10^{-4}
15	37.07 days	4.49×10^{-4}
16	39.80 days	4.50×10^{-4}
17	45.65 days	4.52×10^{-4}
18	50.50 days	4.55×10^{-4}
19	56.00 days	4.57×10^{-4}

---

*Dimensional units of Pa-sec are $(ML^{-1}T^{-1})$.

Initial load = constant = 2.21 MPa $\approx$ 90.0 meters of overburden – load applied by passive gravitational means due to the time requirements of this experimental technique.

Almost all of the strain suffered by the sample was incurred within the first 10 seconds of applying load. Total elastic strain achieved by 4.5 hrs (data point #7) – hereafter strain is due to viscous processes: $e_e = 4.32 \times 10^{-4}$, $e_v = 2.50 \times 10^{-5}$, $e_{total} = e_e + e_v = 4.57 \times 10^{-4}$.

Material reacted as a Maxwell elasticoviscous body (see Appendix A).

Deformation monitored by LVDT and strip-chart recorder.

Test conducted at temperature of 20°C; $\sigma_2 = \sigma_3 = 1$ atmosphere.

Test Performed: Determination of Compressional and Shear Wave Velocities
Lithology Tested: Torres Limestone (Pyt)
Method Employed: Ultrasonic-Pulse

Summary of Test Results

Wave Velocities	Calculated Elastic Moduli
Compressional Wave $V_P = 4.07$ km/sec S = ± 0.062	Young's Modulus* $E = 42.22$ GPa
Shear Wave $V_S = 2.72$ km/sec S = ± 0.066	Modulus of Rigidity* $G = 19.24$ GPa
	Poisson's Ratio* $\nu = 0.19$

Specimen length accurate to 0.05 mm; $\rho = 2.60 g/cm^3$

Travel times accurate to 0.25 microsecond (V_P) and 0.50 microsecond (V_S).

Velocities measured perpendicular to bedding.

Tests conducted at atmospheric pressure.

*Elastic constants calculated from the following relationships derived from the theory of elasticity (Lama, 1978).

$$E = \frac{\rho V_S^2 \left(3V_P^2 - 4V_S^2\right)}{V_P^2 - V_S^2}$$

$$G = \rho V_S^2$$

$$\nu = \frac{V_P^2 - 2V_S^2}{2(V_P^2 - V_S^2)}$$

Test Performed: Ultrasonic-Pulse
Lithology Tested: Torres Limestone (Pyt)

Sample #	Length	Travel Time	V_P	V_S
1	21.60 mm	5.39 ms	4.01 km/sec	
		8.00 ms		2.70 km/sec
2	28.15 mm	6.80 ms	4.14 km/sec	
		10.16 ms		2.77 km/sec
3	27.70 mm	6.84 ms	4.05 km/sec	
		10.30 ms		2.69 km/sec
4	24.50 mm	6.14 ms	3.99 km/sec	
		9.14 ms		2.68 km/sec
5	23.55 mm	5.37 ms	4.13 km/sec	
		8.32 ms		2.83 km/sec
6	25.20 mm	6.30 ms	4.00 km/sec	
		9.13 ms		2.76 km/sec
7	25.35 mm	6.09 ms	4.16 km/sec	
		9.32 ms		2.72 km/sec
8	26.00 mm	6.47 ms	4.02 km/sec	
		9.77 ms		2.66 km/sec
9	26.45 mm	6.47 ms	4.09 km/sec	
		10.06 ms		2.63 km/sec

All samples were right circular cylinders (sections of drill core); measurements were made across the two, parallel flat surfaces; dimensions of the samples were such that V_S results will not be compromised by shear waves being converted into compressional waves.

Waveforms were generally strong and easily readable.

Test Performed: Determination of Compressional and Shear Wave Velocities
Lithology Tested: Cañas/Torres Gypsum (Pyc/Pyt)
Method Employed: Ultrasonic-Pulse

Summary of Test Results

Wave Velocities	Calculated Elastic Moduli
Compressional Wave $V_P = 1.51$ km/sec S = ± 0.042	Young's Modulus* $E = 5.20$ GPa
Shear Wave $V_S = 1.04$ km/sec S = ± 0.045	Modulus of Rigidity* $G = 2.46$ GPa
	Poisson's Ratio* $\nu = 0.10$

Specimen length accurate to 0.05 mm; $\rho = 2.29 g/cm^3$.

Travel times accurate to 0.50 microsecond (V_P) and 1.00 microsecond (V_S).

Velocities measured perpendicular to laminations.

Tests conducted at atmospheric pressure.

*Elastic constants calculated from the following relationships derived from the theory of elasticity (Lama, 1978).

$$E = \frac{\rho V_S^2 \left(3V_P^2 - 4V_S^2\right)}{V_P^2 - V_S^2}$$

$$G = \rho V_S^2$$

$$\nu = \frac{V_P^2 - 2V_S^2}{2(V_P^2 - V_S^2)}$$

Test Performed: Ultrasonic-Pulse
Lithology Tested: Cañas/Torres Gypsum (Pyc/Pyt)

Sample #	Length	Travel Time	V_P	V_S
1	23.25 mm	15.20 ms	1.53 km/sec	
		21.53 ms		1.08 km/sec
2	26.40 mm	17.96 ms	1.47 km/sec	
		26.67 ms		0.99 km/sec
3	24.45 mm	15.47 ms	1.58 km/sec	
		23.07 ms		1.06 km/sec
4	25.75 mm	17.28 ms	1.49 km/sec	
		25.00 ms		1.03 km/sec
5	26.60 mm	17.73 ms	1.50 km/sec	
		26.60 ms		1.00 km/sec
6	25.15 mm	16.33 ms	1.54 km/sec	
		22.86 ms		1.10 km/sec
7	24.90 mm	17.05 ms	1.46 km/sec	
		25.15 ms		0.99 km/sec

All samples were right circular cylinders (sections of drill core); measurements were made across the two, parallel flat surfaces; dimensions of the samples were such that V_S results will not be compromised by shear waves being converted into compressional waves.

Waveforms were generally strong and easily readable.

Test Performed: Determination of Shear Strength
Lithology Tested: Cañas/Torres Gypsum (Pyc/Pyt)
Method Employed: Beveled Shear Dies

Summary of Test Results

Shear Strength (S_0) of Pyc/Pyt Gypsum = 1.42 MPa ± 0.25

Sample #	Length	Applied Load	Shear Strength
10	1.24 in	400 lbs	2.28 MPa
11	1.03 in	200 lbs	1.37 MPa
12	1.12 in	250 lbs	1.58 MPa
13	1.30 in	140 lbs	0.76 MPa

Samples generally started to shear/powder as soon as load was applied; all samples right circular cylinders (core specimens); sample diameter = 1.0 in.

Tests conducted at temperature of 20° C and atmospheric pressure.

Conversion factor: 1 PSI = 6.895 x 10^3 MPa.

REFERENCES CITED

Aldrich, M.J., Jr., Chapin, C.E., and Laughlin, A.W., 1986, Stress history and tectonic development of the Rio Grande rift, New Mexico: *Journal of Geophysical Research*, vol. 91, no. B6, p. 6199–6211.

Allison, I., 1984, The pole of the Mohr diagram: *Journal of Structural Geology*, vol. 6, no. 3, p. 331–333.

Bell, A.M., 1981, Vergence: an evaluation: *Journal of Structural Geology*, vol. 3, no. 1, p. 197–202.

Biot, M.A., 1961, Theory of folding of stratified viscoelastic media and its implications in tectonics and orogenesis: *Geological Society of America Bulletin*, vol. 72, p. 1595–1632.

Biot, M.A., 1965, Further development of the theory of internal buckling of multilayers: *Geological Society of America Bulletin*, vol. 76, p. 833–840.

Brocher, T.M., 1981, Shallow velocity structure of the Rio Grande rift north of Socorro, New Mexico: a reinterpretation: *Journal of Geophysical Research*, vol. 86, no. B6, p. 4960–4970.

Brown, L.D., Krumhansl, P.A., Chapin, C.E., and others, 1979, COCORP seismic reflection studies in the Rio Grande rift, in Riecker, R.E., ed., Rio Grande rift: Tectonics and magmatism: Washington, D.C., American Geophysical Union, p. 169-184.

Brun, J.-P., and Merle, O., 1988, Experiments on folding in spreading-gliding nappes: *Tectonophysics*, vol. 145, p. 129–139.

Chapin, C.E., and Cather, S.M., 1981, Eocene tectonics and sedimentation in the Colorado Plateau-Rocky Mountain area, in Dickinson, W.R., and Payne, M.D., eds., Relations of tectonics to ore deposits in the southern Cordillera: *Arizona Geological Society Digest*, vol. 14, p. 173–198.

Cobbold, P.R., 1983, Kinematic and mechanical discontinuity at a coherent interface: *Journal of Structural Geology*, vol. 5, no. 3/4, p. 341–349.

Colpitts, R.M. Jr., 1986, Geology of the Sierra de la Cruz area, Socorro County, New Mexico [M.S. thesis]: Socorro, New Mexico Institute of Mining and Technology, 167 p.

Condie, K.C., and Budding, A.J., 1979, Geology and geochemistry of Precambrian rocks, central and south-central New Mexico: New Mexico Bureau of Mines and Mineral Resources, Memoir 35, 58 p.

Cutter, J.M., 1985, Error due to strain measurement in non-principal sections: *Tectonophysics*, vol. 113, p. 185–190.

Dunnington, H.V., 1967, Aspects of diagenesis and shape change in stylolitic limestone reservoirs: World Petroleum Congres, 7th, Proceedings, vol. 2, p. 339–352.

Engelder, T., and Geiser, P., 1984, Near-surface *in situ* stress, 4. Residual stress in the Tully Limestone – Appalachian Plateau, New York: *Journal of Geophysical Research*, vol. 89, p. 9365–9370.

Gretener, P.E., 1972, Thoughts on overthrust faulting in a layered sequence: *Bulletin of Canadian Petroleum Geology*, vol. 20, no. 3, p. 583–607.

Guth, P.L., Hodges, K.V., and Williams, J.H., 1982, Limitations on the role of pore pressure in gravity gliding: *Geological Society of America Bulletin*, vol. 93, p. 608–612.

Haimson, B.C., 1977, Crustal stress in the continental United States from hydrofracturing tests, in Heacock, J.G., ed., The earth's crust: American Geophysical Union Monograph, no. 20, p. 576–592.

Hanshaw, B.B., and Bredehoeft, J.D., 1968, On the maintenance of anomalous fluid pressures: II. Source layer buried at depth: *Geological Society of America Bulletin*, vol. 79, p. 1107–1122.

Harding, T.P., 1985, Seismic characteristics and the identification of negative flower structures, positive flower structures, and positive structural inversions: *American Association of Petroleum Geologists Bulletin*, vol. 69, no. 4, p. 562–600.

Heard, H.C., and Rubey, W.W., 1966, Tectonic implications of gypsum dehydration: *Geological Society of America Bulletin*, vol. 77, p. 741–760.

Hobbs, D.W., 1967, The formation of tension joints in sedimentary rocks: an explanation: *Geological Magazine*, vol. 104, no. 6, p. 550–556.

Hook, S.C., 1983, Stratigraphy, paleontology, depositional framework, and nomenclature of marine upper Cretaceous rocks, Socorro County, New Mexico: New Mexico Geological Society Guidebook 34, p. 165–172.

Hunter, J.C., and Ingersoll, R.V., 1981, Cañas Gypsum Member of Yeso Formation (Permian) in New Mexico: *New Mexico Geology*, vol. 3, no. 4, p. 49–52.

Jaeger, J.C., and Cooke, N.G.W., 1979, Fundamentals of rock mechanics: Chapman and Hall, London, 593 p.

Johnson, A., 1984, Physical processes in geology: Freeman and Company, San Francisco, 590 p.

Jordan, P., and Nüesch, R., 1989, Deformational behavior of shale interlayers in evaporite detachment horizons, Jura overthrust, Switzerland: *Journal of Structural Geology*, vol. 11, no. 7, p. 859–871.

Kehle, R.O., 1970, Analysis of gravity sliding and orogenic translation: *Geological Society of America Bulletin*, vol. 81, no. 6, p. 1641–1663.

Keller, G.R., 1983, Bouguer gravity anomaly map of the Socorro region: New Mexico Geological Society Guidebook 34, p. 96.

Lama, R.D., and Vutukuri, V.S., 1978, Handbook on mechanical properties of rocks – volume II: Trans Tech Publications, Clausthal, 481 p.

Linden, R.M., 1987, Strain energy and jointing in coal and adjacent sediments [M.S. thesis]: Socorro, New Mexico Institute of Mining and Technology, 123 p.

Mandl, G., 1988, Mechanics of tectonic faulting: Elsevier, Amsterdam, 407 p.

Mandl, G., and Shippam, G.K., 1981, Mechanical model of thrust sheet gliding and imbrication, in McClay, K.R., and Price, N.J., eds., Thrust and nappe tectonics: Geological Society of London Special Publication no. 9, p. 79–98.

Mase, G.E., 1970, Continuum mechanics: McGraw-Hill, New York, 221 p.

McGarr, A., 1980, Some constraints on the level of shear stress in the crust from observation and theory: *Journal of Geophysical Research*, vol. 85, p. 6231–6238.

Means, W.D., 1976, Stress and strain – basic concepts of continuum mechanics for geologists: Springer-Verlag, New York, 339 p.

Merle, O., 1986, Patterns of stretch trajectories and strain rates within spreading-gliding nappes: *Techtonophysics*, vol. 124, p. 211–222.

Mogi, K., 1966, Some precise measurements of fracture strength of rocks under uniform compressive stress: *Felsmechanik und Ingenieurgeologie*, vol. 4, p. 41–55.

Moore, R.C., Lalicker, C.G., and Fischer, A.G., 1952, Inverterbrate fossils: McGraw-Hill, New York, 766 p.

Müller, W.H., Schmid, S.M., and Briegel, U., 1981, Deformation experiments on anhydrite rocks of different grain sizes: rheology and microfabrics: *Tectonophysics*, vol. 78, p. 527–543.

Murrell, S.A.F., 1981, The rock mechanics of thrust and nappe formation, in McClay, K.R., and Price, N.J., eds., Thrust and nappe tectonics: Geological Society of London Special Publication no. 9, p. 99–109.

Murrell, S.A.F., and Ismail, I.A.H., 1976, The effect of decomposition of hydrous minerals on the mechanical properties of rocks at high temperatures and pressures: *Tectonophysics*, vol. 31, p. 207–258.

Needham, C.E., and Bates, R.L., 1943, Permian type sections in central New Mexico: *Geological Society of America Bulletin*, vol. 54, p. 1653–1668.

Paterson, M.S., 1978, Experimental rock deformation – the brittle field: Springer–Verlag, Berlin, 254 p.

Raleigh, C.B., and Griggs, D.T., 1963, Effect of the toe in the mechanics of overthrust faulting: *Geological Society of America Bulletin*, vol. 74, p. 819–830.

Ramberg, H., 1963, Evolution of drag folds: *Geological Magazine*, vol. 100, p. 97–100.

Ramberg, H., 1981, The role of gravity in orogenic belts, in McClay, K.R., and Price, N.J., eds., Thrust and nappe tectonics: Geological Society of London Special Publication no. 9, p. 125–140.

Ramsay, J.G., 1967, Folding and fracturing of rocks: McGraw-Hill, New York, 586 p.

Ramsay, J.G., and Huber, M.H., 1983, Techniques of modern structural geology: Volume 1, strain analysis: Academic Press, London, p. 1–307.

Ramsay, J.G., and Huber, M.H., 1987. Techniques of modern structural geology: Volume 2, Folds and fractures: Academic Press, London, p. 308–700.

Ranalli, G., 1987, Rheology of the earth: Allen & Unwin, London, 366 p.

Reiner, M., 1949, Twelve lectures on theoretical rheology: North Holland Publishing Company, 162 p.

Rosen, S., 1983, Geology of the Mesa del Yeso area, Socorro County, New Mexico: unpublished report to A.J. Budding, Geoscience Department, New Mexico Institute of Mining and Technology.

Rutter, E.H., 1972, On the creep testing of rocks at constant stress and constant force: *International Journal of Rock Mechanics and Mining Science*, vol. 9, p. 191–195.

Sanford, A.R., 1968, Gravity survey in central Socorro County, New Mexico: New Mexico Bureau of Mines and Mineral Resources, Circular 91, 14 p.

Siemers, W.T., 1983, The Pennsylvanian System, Socorro region, New Mexico: New Mexico Geological Society Guidebook 34, p. 147–155.

Smith, C.T., 1983, Structural problems along the east side of the Socorro constriction, Rio Grande rift: New Mexico Geological Society Guidebook 34, p. 103–109.

Stark, J.T., and Dapples, E.C., 1946, Geology of the Los Pinos mountains, New Mexico: *Geological Society of America Bulletin*, vol. 57, p. 1121–1172.

Suppe, J., 1985, Principles of structural geology: Prentiss–Hall, Englewood Cliffs, 537 p.

Tan, B.K., 1977, Determination of strain elipses from deformed ammonoids: *Tectonophysics*, vol. 16, p. 89–101.

Turcotte, D.L., and Schubert, G., 1982, Geodynamics: applications of continuum physics to geological problems: John Wiley & Sons, New York, 450 p.

Webb, B.C., and Cooper, A.H., 1988, Slump folds and gravity slide structures in a Lower Paleozoic marginal basin sequence (the Skiddaw Group), NW England: *Journal of Structural Geology*, vol. 10, no. 5, p. 463–472.

Williams, S. C., 1988, The shear strength of single gypsum crystals on three cleavage planes: *Tectonophysics*, vol. 148, p. 163–173.

— *F I N I S* —

This dissertation is accepted on behalf of the faculty of the Institute by the following committee:

A. T. Budding
Adviser

Manfred O. Peter

Allan R. Sanford

Lloyd B. Thum

R W Ohlin

Feb. 11 1991
Date